Neutrino Point Source Analysis at the TXS 0506+056 Position with 9.5 Years of IceCube Data

Master Thesis
by
Benedikt Krammer

23.07.2018

Technical University Munich
Physics Department, Group ECP
Prof. Elisa Resconi

Contents

Abstract

Despite the observation of an isotropic astrophysical neutrino flux in 2013 by IceCube, the origin of those neutrinos at highest energies is not yet known. Cosmic particles have been found at energies of EeV scale, therefore exceeding earthborne particle accelerator limits like the LHC by six orders of magnitude. Blazars, a class of Active Galactic Nuclei with jets oriented along the line of sight of the observer, pose likely source candidates for both neutrinos and Cosmic Rays. The acceleration mechanisms in blazar jets can be uniquely probed for hadronic processes by highest-energetic neutrinos. On the 22nd of September 2017, an IceCube Extremely High Energy neutrino event (IceCube-170922A) was simultaneously observed with a gamma-ray flare from a *Fermi*-LAT catalogued blazar in the same position. The coincidence sparked a large-scale multimessenger campaign resulting in detections in all wavelength bands.
In order to understand this association, a search for an excess in neutrinos in 9.5 years of IceCube muon track data is performed. The analysis in this work includes the time of the enhanced gamma-ray activity of the source TXS 0506+056. A combined data sample of 7 years of point source muon tracks and 2.5 years of the gamma-ray follow-up muon stream is utilized. Totalling to 9.5 years, this is the largest IceCube point source sample at the time of the analysis execution. To identify a prospective neutrino point source, an unbinned maximum likelihood approach with spacial and energy weighting is employed. This has previously been used for the point source search in 7 years of IceCube data. On the whole 9.5-years dataset, the analysis yields strong evidence (4.1σ) for neutrino emission from the source direction. Yet since the event that triggered the search contributes to the significance, this result is considered biased. For an independent analysis, the single event IC170922A is removed from the track sample. An excess of 2.3σ over no-source hypothesis is found. This is a growth in comparison to the significance in the 7 years result at this position, supporting indication for the first point-like source of IceCube neutrinos and Cosmic Rays.

Acknowledgements

First, I want to thank Prof. Elisa Resconi for allowing me to work on this very rewarding topic without as much as a moment of hesitation. I'm grateful for her supervision, encouragement and support.
I would also like to thank Chad Finley for his calm and structured way to organize the publication of the TXS results, for his help, the useful discussions, and lots of input. Thanks also to my colleagues Josh, Thomas, and Imen. I enjoyed working together with you all, and I think we can be proud of what we managed to do.

I want to thank my office mates Christian, Stephan, Maxi, Imma, Andrea, Theo, Matthias, Felix, Andi, other Christian, Nikhita, Natasha and all the people working in the ECP group for the great time I had with you. Thanks also for the hours of inspiring talks, not only on the subjects of this thesis but on physics and politics and various other topics as well.

Special thanks go to Matthias for explaining various aspects of *skylab*, to Paolo and Paolo for taking the time to share their vast knowledge with me, to Bruno and Yu-Ling for our discussions and the expertise they shared, Andrea for the lessons in color arrangements and to Christian for the enlightening discussions right at the edge of known physics.

Finally, I would like to thank my family and my friends for supporting me in any imaginable way. I owe you everything.

Chapter 1

Neutrino Astronomy: Basic Concepts

Ionized nuclei, photons and neutrinos from outside our galaxy are being detected at energies well beyond those achievable by the LHC[1]. Their origin is not known to date. Primary cosmic rays can not precisely be tracked down to their cosmic accelerators, since charged particles are deflected in magnetic fields. In the magnetic field of our galaxy, they are subject to Lorentz forces and reach the Earth only after changing their initial trajectory. Thus one has to rely on the neutral secondary particles that are created in the same processes as the cosmic rays, or that are being produced near the source: photons and neutrinos. Those can travel through space relatively unimpeded on straight lines, pointing back to their sources.

1.1 Cosmic Particle Acceleration

The origin of cosmic rays is a still-unsolved and fundamental problem of astroparticle physics. There exists no definite knowledge about their sources, or the process(es) that accelerate them to GeV-EeV energies.

Acceleration processes of cosmic rays can in principle occur in two environments. Cosmic rays can either be created in our galaxy or they are produced in (extragalactic) point-like sources with extreme energy densities. The exact mechanism of cosmic ray (CR) acceleration is an open question of astroparticle physics, but there exist theoretical prototypes: Fermi proposed two mechanisms boosting the energy of charged particles in ambient non-linear magnetic fields of turbulent intragalactic plasma or shockwave fronts [Fermi, 1949], see the appendix for details. The Fermi mechanisms provide an estimate of the achievable energies for particles that are trapped in the magnetic field of our galaxy. Those particles undergo acceleration until they are detected on Earth. Purely galactic acceleration is not efficient enough to produce CR in the high-energy tail of the spectrum [Gaisser et al., 2016, chps. 9, 12]. The higher the cosmic particle energy, the smaller is the amount of time they traverse our galaxy, derived from measurements of the CR composition at different energies. A Fermi-like stochastic acceleration process in our galaxy would effect the opposite: one would expect that acceleration to higher energies takes longer in the same environment. Instead, cosmic particles at the highest energies apparently spend little time in our galaxy and originate from beyond. Cosmic neutrinos at PeV energies can be found at high galactic latitudes, far off the galactic plane [Aartsen, 2013]. Therefore, point-like extragalactic objects are good potential candidates for the still-hidden mechanisms behind CR acceleration.

[1]Cosmic rays can be detected up to EeV energies, neutrinos up to a few PeV and photons until 100 TeV. The Large Hadron Collider was built to accelerate protons to up to 14 TeV in the center-of-mass system.

1.2 Cosmic Accelerators: Active Galactic Nuclei

Active Galactic Nuclei (AGN) are extreme extragalactic objects and potential candidates for cosmic ray acceleration to the highest energies. They are observable over a wide range of wavebands that spans up to 10^{27} Hz (TeV energy equivalent for photons). Their luminosity allows for probing large spacial and temporal scales of the universe: the most distant detected AGN lies at a redshift of $z = 7.1$ [Mortlock et al., 2011].
AGN consist of a super-massive black hole (SMBH, 10^6-10^{10} $M_\odot$ for AGN) with an accretion disk in its gravitational potential. AGN are permanent, non-explosive sources, although displaying aperiodic variability. This makes them good targets for long-term monitoring.

In the unified view of AGN [Urry and Padovani, 1995], the black hole and accretion disk are surrounded by a dusty torus and a corona obscuring the AGN center. Their observed properties vary with the angle at which the disk-orthogonal axis is oriented towards the observer. Depending on this tilt, different regions of an AGN are dominating the total emission. Thus one type of rotationally symmetric object could explain a variety of different properties. In the unified view, the orientation, the accretion rate, host galaxy contamination and the existence of a jet are the only parameters that vary between different AGN types.
A fraction of AGN has jets orthogonal to the rotating disk and aligned with the line of sight of the observer. Those form the subclass of blazars. The existence of a jet pointing in the Earth's direction breaks the $1/r^2$ dependence of apparent luminosity in spherically symmetric objects, thus blazars are visible over large distances. The synonym 'jetted AGN' refers to the observed object properties only, meaning that an object possesses a jet **and** the jet is oriented towards the observer along the line of sight. AGN without a jet, or with a jet at a large off-axis angle are called non-jetted. Blazars emit dominantly non-thermal radiation from the jet in all observed wavelengths, and have only broad or no absorption features. In contrast, non-jetted AGN emit mainly thermally and show strong emission lines. Only jetted AGN are visible in gamma-rays.

The distinction between different AGN classes is generally non-trivial, including a separation between jetted/non-jetted. Some distinctions can be inferred from basic observations, often in one single band: if gamma-ray observations are present, the object must be jetted. Objects with sharp emission lines in the IR/optical/UV are non-jetted. Especially the observation of the 'big blue bump', optical thermal emission in AGN, rules out a jet. If the radio flux of an AGN exceeds 1 mJy, the object is most likely jetted. Star formation can contribute to non-jetted AGN radio emission, resulting in a non-jetted AGN exceeding this threshold in rare cases, making it appear jetted. Both jetted and non-jetted AGN emit in X-rays. In the latter, there is a correlation between the optical/UV emission and the X-ray band flux - both originate from the disk. If the observed X-ray flux exceeds the one expected from this relation for a known optical spectrum, a jet is likely present in the object. The radio spectrum of blazars/jetted AGN is on average flatter than in non-jetted AGN. In a multiwavelength observation, non- or thermal emission will be evident: a galactic blackbody spectrum contribution is a sign of no jet or a jet at a large angle to the observer's line of sight.

In AGN without a strong jet, radio band photons are created in a small central volume near the black hole. Current radio observatories are the most sensitive instruments to detect AGN. Infrared (IR) light is associated to hot dust in the torus. Optical/UV emission can show characteristic lines from the material of the accretion disk. Emission lines are broadened if dust (partially) obscures the AGN center. AGN can indirectly be identified in their host galaxies by observation of narrow absorption lines that are untypical for the galaxy spectrum. X-rays are produced in processes in the accretion disk. The emission is putatively non-thermal via Inverse Compton upscattering of accretion disk photons on relativistic electrons, though a small thermal component can make a contribution in low X-ray energies. X-rays can traverse the dust regions around an AGN center without interacting and serve as good AGN tracers with minimal selection biases. Galaxies display only weak emission in this band, and hot dust X-ray emission from non-AGN processes is intrinsically thermal, so (high-energy) X-rays allow to distinguish AGN reliably. Contrasting non-jetted AGN, blazars show a large (and often dominant) jet contribution of non-thermal radiation in every waveband. Additionally, they appear to have their center obscured less towards the observer, indicating the absence of dust in the line of sight towards the observer.

AGN display high variability in all wavebands and on a broad variety of timescales. The duration of a high state or flare in a certain band corresponds to the size of the region in which the radiation is produced. In the X-ray band, AGN show changes in flux on hour-to-day scales, scaling linearly with the mass of the central black hole. Optical and UV emission changes on day-to-month scales. In this band, a characteristic feature is the so-called "red lag": longer wavelengths show the same time-dependent behavior than shorter ones, but with a small $O(1 \text{ day})$ delay. This supports the hypothesis of a central X-ray heating mechanism driving the emission. 'Redder' light is in that case emitted at a large disk radius, and the central X-ray driving radiation takes longer to reach the more faraway area. Shorter-wavelength light is emitted closer to the center, which is reached faster. This hints at one central mechanism influencing all emission from an AGN.

AGN variability is not an effect of obscuration or absorption on large scales. More distant sources show the same variable behavior as close ones, so variable absorption does not play a major role. The fact that AGN variability is similarly observed on the whole population is an indication against periodic obscuration of AGN emission. The timescales of AGN variability depend on the mass of the central black hole M_{BH} in all bands up to UV. The AGN variability amplitude seems anticorrelated with M_{BH}, leading to an anticorrelation with luminosity in X-ray, IR and optical. Gamma-ray variability is closely associated to an AGN jet (if present) and is observed on timescales of months, weeks and down to single days. Whether or how much the jet is influenced by the variability of accretion is an open issue in the field. In consequence, time-dependent behaviour is an inherent property of the central emission mechanism. Flares in different photon wavebands as well as neutrinos should share the same driving engine: the accretion process or the jet.

The observed properties of an AGN seem therefore to be intrinsically connected with each other. The apparent correlation between accretion/jet with the emission in all wavebands hints towards a central driving mechanism. Expanding this scenario to neutrinos, one can use this connection to guide neutrino astronomy: flux scales and variability in photons could eventually be translated into accurate predictions for neutrino emission, ultimately leading to a full multimessenger picture.

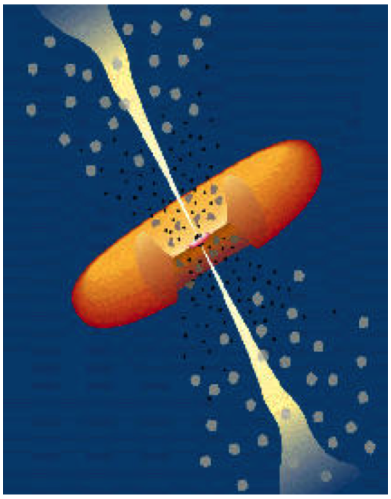

Figure 1.1: *Depiction of a jetted AGN - not to scale. The exact type of emission an observer measures is determined by the viewing angle (angle between observer line of sight and the jet axis). For small angles, one finds the typical blazar view without sharp absorption/emission features, for large angles approaching 90°, the galaxy with strong features dominates. In between, one can observe toral or dust-generated (small dots in the image) emission. [Urry and Padovani, 1995], copied with permission.*

Apart from AGN, there are further candidate populations for cosmic accelerators: GRBs are the most luminous events in the gamma-ray sky. They are transients with an enormous point-like eruption of photons in a very short time interval and a decreased successive emission ('afterglow') for a longer period. Their progenitor objects are hard to identify, making them nearly impossible to monitor. Due to their power, they are being examined as neutrino sources, but suffer from decreasing support from physical models [Waxman and Bahcall, 1997] [Aartsen et al., 2016a]. Supernovae are believed to produce supersonic shocks that could in principle accelerate particles to high energies. Extragalactic objects with a high rate of SN explosions are called Star-Forming (SFG) or Star-Burst (SBG) Galaxies and are also investigated as sources in other works [Gaisser et al., 2016, chp. 18]. In [Bechtol et al., 2017], different source classes of both transient and steady type are investigated, showing that blazars and blazar flares are currently the most interesting observational targets in terms of detectability and expected signal-clustering.

1.3 Blazar Properties

The blazar spectrum is always Doppler-boosted and blueshifted, due to beaming of light sent out from a highly relativistic jet at a small angle [Urry and Padovani, 1995]. It forms a characteristic shape with two broad humps: one in the radio to soft X-ray, and one in X-ray to HE and sometimes VHE gamma-rays (HE: 100 MeV - 100 GeV; VHE: 50 GeV - >10 TeV). The hump at lower energies is assumed to originate from synchrotron radiation. The high energy hump is not completely understood: it can come from Inverse Compton scattering in a purely leptonic acceleration scenario, from photon-meson interaction or proton synchrotron losses in a hadronic scenario, or from a combination of both.

Blazars themselves consist of two types of objects, BL Lacs and flat-spectrum radio quasars (FSRQs). FSRQs show broad emission/absorption lines. BL Lac type objects display these lines only very weakly or not at all. BL Lacs spectra usually extend to higher energies in the VHE band.

Blazars can be subdivided in classes based on the peak position of their first hump: if the synchrotron hump peaks above 10^{15} Hz (below 10^{14} Hz), the object is called high(low)-synchrotron-peak HSP (LSP) or high(low)-synchrotron-peaked BL Lac HBL (LBL) for BL Lac blazars [Padovani and Giommi, 1995] [Abdo et al., 2010]. In between, they are called intermediate (ISP/IBL). These classes are affected differently by selection biases in single-band studies. Especially in high-energy gamma-rays, HSPs dominate samples, see [Ajello et al., 2017] for an example. Still, the classification is purely observational and not motivated by underlying physics.

Detection of blazars in gamma-rays of the HE band (100 MeV - 100 GeV) can be realized in two different ways with the current-generation instruments: 1) All-sky surveys can find photon excesses in an unbiased way, identifying sources purely from data. 2) Source searches targetting known emitters in other bands (radio, X-ray) on the other hand can find AGN that could not be detected by the first method.

Detection in the VHE (>50 GeV) band is, due to the small field of view of the ground-based IACTs, limited to sources known in other bands. The strong absorption effect of VHE radiation undergoing pair production with extragalactic background light photons restricts the achievable depth in redshift. Detection of a source on the other hand allows to extract information of an object that is otherwise inaccessible. Sources that are sub-threshold for VHE experiments in quiescent state can often still be detected in a flaring state, if the observation is triggered by a flare reported in a lower band (HE gamma, X-ray).

The combined flux in gamma-rays from blazars and radiogalaxies equals approximately the total extragalactic gamma-ray background (EGB). HSP blazars are the dominant contributors to the EGB above 100 GeV [Ajello et al., 2015].

Blazar populations and classifications can be found in respective catalogs. Catalogues are complete lists of objects selected by luminosity/spectral criteria. For blazars, selection options are physically and observationally motivated: 1) Radio-selected catalogs provide the largest samples with moderate selection bias. 2) Gamma-ray selected blazars show high-energy emission hinting at neutrino production. 3) HBL/HSP blazars are potentially connected to neutrinos in other searches (see below). Other selections are possible, but often suffer from incompleteness or selection biases - blazar classes with high emission in a single band are preferentially selected by this band. FSRQ have strong radio emission, so radio-selected blazar catalogs feature large fractions of those. HSP BL Lac objects emit X-rays at high fluxes, so X-ray selections are biased towards them. The *Fermi*-LAT instrument is more sensitive for hard-spectrum objects, therefore BL Lac objects are preferred in the HE band.

Examples for catalogs are:
1) The 2WHSP: radio-selected blazars of the WISE survey can be sorted by their synchrotron peak. This requires a fit to the entire SED (if available). The high-synchrotron-peaked objects (HSP) are listed in this compilation [Chang et al., 2017].
2) *Fermi*-LAT detected blazars are listed in different catalogs. Those sources are gamma-ray detected and often identified with observed sources in other bands. The 2LAC is an early gamma-ray catalog with 2 years of data [Ackermann, 2011], with an update in the 3LAC [Ackermann et al., 2015]. FHL catalogs (2FHL, 3FHL) only contain *Fermi*-LAT hard sources which is relevant to neutrino physics [Ackermann et al., 2016] [Ajello et al., 2017].
3) Subsamples of the FHL catalogs with high synchrotron peaks can be used as HBL lists. The 2WHSP

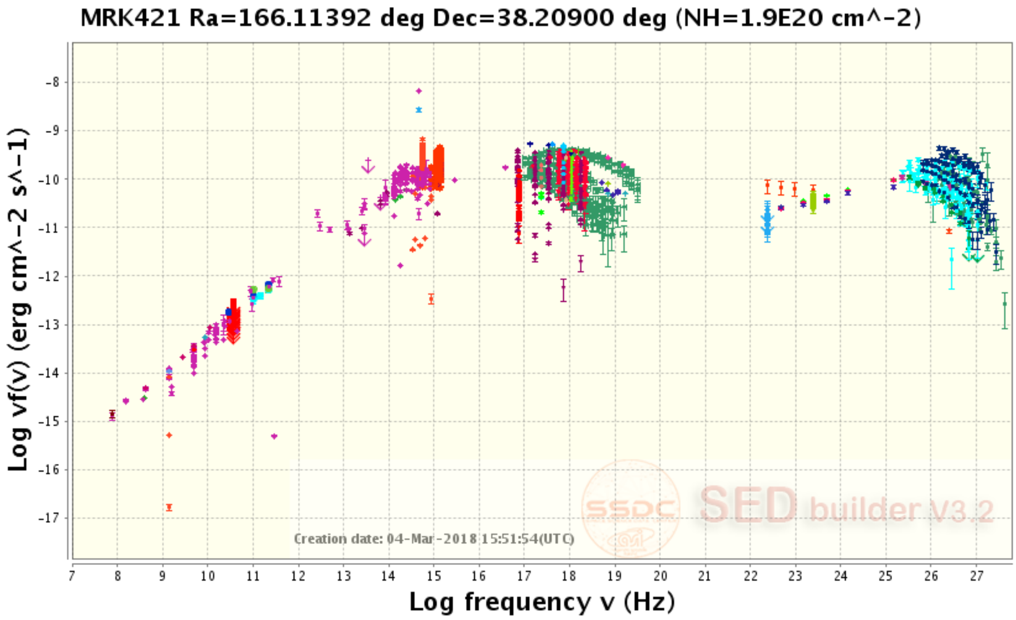

Figure 1.2: *Spectral Energy Distribution (SED) of Markarian 421, frequency over flux times frequency. MRK 421 is one of the closest and the most prominent blazars. An SED shows the source photon energy flux for photon wavelengths from radio via infrared, optical/UV and X-ray up to gamma rays. It is generated by synopting data from all experiments and observatories, earthborne telescopes and spaceborne satellites that have at some point observed the source. Different colors in the data points mark different experiments, time-variability of the emission causes multiple values per frequency to show. One can clearly distinguish the two humps characteristic for a blazar SED. The first is a tracer of synchrotron emission, the second can be attributed to Inverse Compton scattering or (semi-) hadronic processes. The distribution spans the whole observable spectrum. Compare [Mastichiadis and Kirk, 1997] for a treatment of acceleration physics in this source.*

inherently provides a large list of high-peaked blazars.
A special category is variability-selected blazars. The FAVA catalog lists these objects [S. Abdollahi, 2017]. As a *Fermi*-LAT catalog, the objects are gamma-ray-selected. High-energy blazar flares could be correlated with neutrino emission, so this selection is relevant for neutrino source searches.

1.3.1 Non-thermal Emission

Blazars are extragalactic sources of photons in all wavebands. They emit dominantly non-thermal from their highly relativistic jet. Three processes are believed to produce non-thermal radiation (compare [Gaisser et al., 2016, chp. 14]):

1) Synchrotron radiation

2) Inverse Compton Effect

3) Photopion Production

1) Synchrotron radiation is emitted whenever a charged particle at relativistic velocity experiences a Lorentz force and therefore a change of propagation direction. In a blazar jet, a population of charged particles can lose energy via this process in strong magnetic fields. Electrons are responsible for most

of the synchrotron radiation that is detected. They are accelerated to relativistic energies quickly and experience strong trajectory changes from Lorentz force - both due to their low mass. This creates synchrotron photons at energies between the radio and soft X-ray band.

2) The Inverse Compton effect occurs upon scattering of photons with fast charged particles. In the Compton process, a high-energetic photon loses energy by transferring its momentum to an electron in an atom. The electron gains energy and may leave its bound state. The opposite is what occurs in the Inverse Compton Process: low energy photons - for example from synchrotron processes - scatter off relativistic particles and gain energy. This produces photons at the highest energies observed, in the gamma-ray band up to 100 TeV. The scattering partners of the accelerated photons lose energy [Mastichiadis and Kirk, 1997].

3) Photo-Pion production occurs whenever a fast nucleus interacts with ambient particles (matter or photons) and produces pions. In an example process, a proton hits target material, producing a pion:

$$p^+ + \text{target } X \rightarrow \pi^0 + X' \tag{1.1}$$

$$\pi^0 \rightarrow \gamma + \gamma \tag{1.2}$$

X and X' are particles or composites, X' can contain the educt proton. Neutral pions decay into two photons. The produced photons can have energies up to the VHE gamma-ray band.
In hadronic processes involving pions, not only photons, but also neutrinos can be created [Mannheim, 1995]. For neutrinos, charged pions have to be produced:

$$p^+ + \text{target } X \rightarrow \pi^+ + X^-$$

$$\pi^+ \rightarrow \mu^+ + \nu_\mu$$

One (anti-)muon decays into two (anti-)electron neutrinos + one (anti-)electron. A correlation can be found for photon and neutrino numbers: a π_0 decays into two photons, a charged pion into 3 neutrinos. Since those arrive in a flavour ratio 1:1:1, one muon neutrino in IceCube comes with 2 photons in this simplified picture. This does of course not account for absorption of gamma-photons.

Photons at TeV energies undergo pair production with ambient EM radiation fields (Extragalactic Background Light, EBL). During propagation, they lose energy or get absorbed. The longer the travelled distance, the fewer photons one sees due to this attenuation. For TeV observation, this creates an effective horizon or depth in redshift behind which sources cannot be detected, if they don't emit at high luminosities.

Neutrinos do not lose energy until they reach the observer, but they are hard to detect due to their low cross-section. One does not see only astrophysical ν_μ or ν_e on Earth - neutrinos oscillate during propagation. If they can travel without weak force interaction, neutrinos assume their mass Eigenstates. Those are each mixtures of all three flavour Eigenstates. The transition probability between them depends on the mass difference, and the travelled distance[2]. Different transitions have different 'baseline' distances, but on cosmic length scales, all occur in the equilibrium of equal flavour proportion. For neutrino source searches on muon track samples, this means that neutrinos from any source will arrive partially as muon neutrinos [Gaisser et al., 2016, chp. 7]. For a brief discussion of neutrino oscillations and their physical implications, see the appendix, Sec. A.1.

[2]The dependence is approximately linear for small lengths or high energies

1.3.2 Neutrinos from Blazars

Blazars are potential sources of astrophysical neutrinos. Detection of a blazar in neutrinos would be a smoking-gun proof of hadronic interactions in blazar jets. A direct $\nu - \gamma -$connection could not yet be established. For now, there are no single sources with sufficient neutrino emission to be detected with high significance by an unbiased IceCube search. More precisely, in the IceCube 7 year point source sample, no single spot in the sky passes the 5σ threshold for detection. Hotspots above the 3 or 4σ threshold exist, but after correcting for a possible *Look-Elsewhere*-effect, no significant spot could be claimed. Details of a point source search on 7 years of through-going muon tracks can be found in [Aartsen et al., 2017a]. The event selection and analysis methods are very similar to the analysis presented later in this work. Fig.6 of [Aartsen et al., 2017a] shows the all-sky scan results: IceCube neutrinos are in every point on the scanned grid compatible with diffuse emission.

Using the Hotspot Population Analysis contained in [Aartsen et al., 2017a], one can draw conclusions on population searches with IceCube. Instead of one strong source, it tests for an accumulation of intermediately significant spots (local maxima on the all-sky). The threshold for significance is set to

$$-log10(\text{p-value}) \geq 3.$$

. The expectation of n hotspots above that value is calculated on randomized trials. The number of passing spots on real data is compared to the trials. If there are weak sources present in data, one would expect more spots in the real sky: the random fluctuations plus the real sources. Here as well, no excess over background is found. This allows to set limits on the minimal number of sources that contribute to the total neutrino flux: in the north, at least 1000 weak sources are required to explain the diffuse flux. In the Southern hemisphere, the limit is less strict: 40 sources. The difference is due to the analysis being more sensitive in the north. This calculation assumes a weakly emitting population where each source has an equally significant contribution/strength. If blazars are responsible for the diffuse astrophysical flux measured by IceCube, a large number of them has to emit weakly. In short:

- Single blazars cannot be detected by IceCube in an unbiased search or without a more refined hypothesis to be tested.
- If blazars produce the entire diffuse neutrino flux, there must be a large number of them contributing.
- Astrophysical neutrino emission can not be distinguished from a diffuse flux by an unbiased search.

The first and third bullets contain a way to find neutrino sources despite previous non-detections. The analyses in [Aartsen et al., 2017a] are 'unbiased'. They test two mutually exclusive hypotheses against each other: H_0: There are no neutrino point sources (pure diffuse background). H_1: There are neutrino point sources.
This is a clean and model-independent approach. No prior knowledge enters in the test. If a physics model has to be tested on the other hand, one can choose different hypotheses. In the blazar case:
H_0: A set of blazars produces no neutrino signal (pure diffuse background at the blazar positions).
H_1: A set of blazars shows an excess in neutrinos.

Various searches for neutrino sources in blazar populations have been performed. They resulted in non-detections and therefore upper limits on the maximal contribution of blazars to the diffuse neutrino flux. The results and limits should not be mistaken for an exclusion of blazars as neutrino sources.

In [Huber, 2017], neutrino emission from blazar populations is investigated by stacking. Compared to single point source searches, stacking accumulates signal from all sources. This increases the chance of a detection. For stacking, one preselects sources and calculates a combined signal hypothesis. The preselection is done by using a catalog of blazars.
Corresponding catalogs or subsamples have been investigated in [Huber, 2017]: the 2WHSP, a catalog of HSP blazars, the 2FHL HSP selection and the 3LAC FSRQ sources are stacked [Chang et al., 2017] [Ackermann et al., 2015] [Ackermann et al., 2016]. No significant excess could be found in any of the tests, placing strict upper limits on the maximal contribution of the respective blazar selections.

In [Aartsen et al., 2017b], a different selection is tested. The FermiLAT 2LAC [Ackermann, 2011] was the largest blazar catalog in gamma-rays available for this (early) study. It contained all well-identified FermiLAT sources at that time, but neglects selection biases in the gamma band. The 2LAC uses the first two years of FermiLAT mission time and has been updated multiple times since.
It is estimated that 70% of the extragalactic gamma-ray background (EGB) originate from the 862 blazars in the 'clean sample' part of the 2LAC (see the reference for details). Based on this, an extrapolation from the 2LAC to the entire population is made: assuming known neutrino-gamma correlations, limits on the total blazar neutrino emission are given. Two scenarios are calculated: all blazars emit neutrinos equally vs. all blazars emit proportionally to their gamma-ray flux. The stacking analysis finds no significant excess and therefore places upper limits on neutrino emission from blazars. In the first approach (equal emission), no more than 27% of the diffuse neutrino emission can be attributed to the 2LAC blazars. The limit assumes that blazars emit with the spectral index of the diffuse neutrino flux. For harder spectra ($\gamma = 2.2$), the limit weakens to $\approx 50\%$. With a physically motivated weighting scheme ($F\gamma \sim F\nu$) the limits is stricter (10% of the entire neutrino flux).

The limits indicate that neutrino emission from blazars is not fully understood: physical properties of blazars that come with neutrino production have not been found yet. No blazar selection or catalog could be shown to contain dominantly neutrino emitters. Concepts have been restricted, but many remain to be tested. Signal can also be time-dependent and rare. In that case time-integrated searches would be dominated by background, but time-dependent or triggered searches will be successful.

In contrast to stacking limits, there are tests that find hints at correlations between blazars, neutrinos and cosmic rays. In [Resconi et al., 2017], 51 IceCube high-energy starting events and 28 additional track events (see Sec. 1.5) are examined together with blazars and cosmic rays. These blazars are listed in catalogues as above and lie either within or outside of a neutrino error circle. The neutrinos divide them in on- and off-event sources, effectively filtering the catalogs. Both on/off types are then tested as sources of cosmic rays, looking at spacial correlation. A likelihood ratio test is performed for: 1) the on-event vs. the off-event sources. 2) 2FHL HBL-type blazars. 3) catalogs from the stacking analysis above.
For the blazars connected to the neutrinos ('on'), excesses are found for different subsamples. The complement ('off'-event sources) does not show a correlation. None of the excesses are above detection threshold. For 2FHL HBL sources, the excess almost reaches the evidence threshold (2.8σ). The on-vs.-off test favours the on-event neutrino-filtered sources by 2.9σ. All p-values are trial-corrected for the number of (nested) tests. This is a strong indication to a common origin of gamma-rays, CR and neutrinos: blazars.

Blazars are good source candidates for neutrino emission. Strong hints of neutrino emission from blazars exist in connection with the blazar flux or the HBL classification. So far, no specific blazar type or property could be identified with the capability of neutrino production. There are strict limits on neutrino emission of blazar subsets, and subsequent extrapolations to the entire population. In consequence, new searches have to be defined to determine the physics behind blazar emission and the origin of the IceCube neutrinos.

1.3.3 Blazar flares

If blazars emit neutrinos time-dependently, this can be used to increase point source search sensitivities. If those flares are correlated with gamma-ray flares, this is another boost of the analysis performance. Time-dependent $\nu - \gamma$ correlation can be theoretically motivated (see the appendix). A detection in this channel would reveal new physics in blazars.

Blazars are stationary sources, but not necessarily continuous neutrino emitters. In photons, especially in gamma-rays, they display high variability. In a similar manner, they can potentially launch neutrino outbursts. For neutrino searches, this could provide a tool for background suppression and increased chance of detection [Ahlers and Halzen, 2014].
A time-integrated search will find the same result for continuous emission and a source that emits the same number of neutrinos in flares/bursts. If a source exhibits flares, one can select time-windows with high emission to efficiently reduce the background and only accumulate the signal. This increases the sensitivity of an analysis to variable sources - flaring blazars can be detectable as neutrino emitters. Furthermore, blazars provide a potential guide to finding suitable time-intervals: they flare in photons. Especially states of high gamma-ray luminosity are good candidates to accompany neutrino emission. If they can be successfully used as triggers for time-variable neutrino emission searches, source detections in IceCube neutrinos should be the consequence.

In [Halzen and Kheirandish, 2016], two blazars known for strong variability in gamma-rays are investigated: 1ES 1959+650 and 3C 279. For 3C 279, detailed calculations of the expected number of neutrino events are made. The authors treat both pp and $p\gamma$ interactions as possible neutrino production mechanisms [Stecker et al., 1991] [Mannheim, 1995]. For all three flares of the object combined, they find a number of 4 (pp) or 2 ($p\gamma$) expected neutrino events in the [1 TeV; 10 PeV] range. They compare this to a number of 1/1000 atmospheric background neutrinos expected in IceCube in a 0.3° radius. The conclusion is that under these assumptions, a detection in IceCube is possible.
For 1ES 1959+650, an IceCube follow-up campaign of a flare in 2016 has been run [IceCube et al., 2017]. 1ES 1959+650 is an HBL blazar. A previous flare from this object was lacking X-ray emission - this is in tension with purely leptonic models of emission. Hadronic models give a better description of the multiwavelength emission and predict a neutrino flux during the so-called 'orphan flare'. For the flare in 2016, an orphan flare can be excluded for the largest part of the time-window. The campaign found no significant neutrino emission over background in all three sub-analyses. Future modelling can be improved based on this result.

Recent theoretical studies of blazar flares use multiwavelength data in different blazar emission states to predict neutrino fluxes. By energetic arguments, fits to the SED can be used to predict a neutrino flux. Essential in this frame is a precise knowledge of gamma-ray fluxes in the different blazar states. The MRK 421 (fig. 1.2) emission is known down to short timescales. It is a well-studied target for physical modelling. In [Petropoulou et al., 2016], it was used to verify this type of model successfully.

Leptohadronic models attempt to predict the spectra of particle species in an acceleration region. Blazar emission is calculated via the escaping products of the region. An early example of this is [Mastichiadis and Kirk, 1995]. Here photons, electrons and protons are included in one single acceleration region. They undergo reactions where they lose energy and produce particles, leading to a gain-and-loss equation for each species. Important channels for production: photons serve as scattering targets, electrons produce synchrotron emission, protons undergo hadronic processes. Hadronic processes are mainly pion or neutron production, leading to neutrino emission. [Mastichiadis and Kirk, 1995] underestimates achievable neutrino emission energies - they predict a cutoff at 10 TeV. This is corrected in more recent approaches. A more detailed view on the complexity of the model as well as a novel dynamical approach is given in the appendix.

1.4 The IceCube Detector

IceCube is a gigaton-water-cherenkhov neutrino detector located at the geographical south pole at a depth of 2450 km to 1450 km. It consists of 86 'strings' on a hexagonal grid with 125 m spacing between two strings, carrying in total 5160 optical modules (DOMs). The DOMs contain photomultipliers, digitizing and calibration electronics and are connected to the IceCube Counting Lab via the cables along their respective string. Thus one cubic kilometer of high-purity deep ice is instrumented with photodetectors as shown in Fig.1.3. Events from the full sphere (4π) of incoming directions can be detected with a near-perfect uptime. Located directly at the South Pole, the event detection is perfectly axisymmetric to the earth's rotational axis and therefore isotropic in rightascension. There are two main detection regions divided by the horizon: for atmospheric muons and neutrinos, the south is 'open' and the Northern hemisphere is shielded by the earth. In consequence, high energy neutrinos, but also background muons, are suppressed in the north [M.G. Aartsen, 2017b].

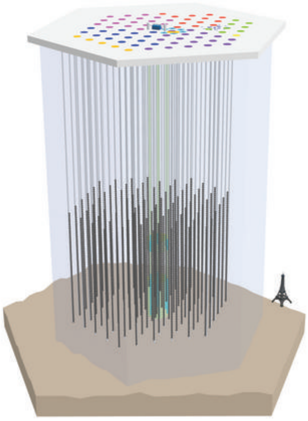

Figure 1.3: *Left: the IceCube detector array, colors indicate different deployment seasons. The instrumented part is highlighted grey and reaches from 2450m to 1450m depth. The innermost (green) 8 strings belong to the IceCube DeepCore array (light blue) for low-energy measurements. The horizontal gap in DeepCore is at the height of the dust layer at ca. 2100 m, a plane in the ice where, due to sediments of volcanic activities in the distant past, the ice is impure. The optical properties are less optimal than for the rest of the detector: shorter scattering length, higher absorption. This has a strong impact on the event reconstruction in this part of IceCube. HESE cascades are very much affected by the diminished light count there. Muon track reconstruction is less impaired, but a directional shift by very small angles can't be excluded for current Ice models. Eiffel tower for scale next to the array. Right: Digital Optical Module connected to the counting-house via the string. The PMT points downwards, in the upper half of the sphere the electronics are located. http://gallery.icecube.wisc.edu/internal/v/graphics/arraygraphics2011/ArrayWSeasonsLabels.jpg.html*

Neutrinos have very small cross-sections for interaction with matter[3], making them hard to detect. The cross-section rises approximately linearly with energy, so higher-energetic events are more likely to be seen, but they are still very rare events compared to the abundant atmospheric and cosmic radiation particles [Patrignani et al., 2016, ch. 35]. The large underground detector volume is therefore serving three purposes:

1. At the depth of the detector at 1450 m, the large ice overburden serves as passive Veto.
2. The mass of ice serves as target material, providing an immense amount of nucleon to scatter with.
3. The instrumented volume is large enough to contain directional information of secondary particles, allowing for reconstruction of the ν direction of origin.

When a sufficiently high-energetic neutrino interacts in or near the detector volume, the charged lepton leaving the charged-current interaction produces Cherenkhov light [Patrignani et al., 2016, ch. 33.7]. That is the case as long as the particle speed exceeds the speed of light in the medium. Light is emitted in a cone around the particle path and propagates through the ice. In contrast to water, the southpole ice has a large absorption length on the order of 120 m and excellent purity. This justifies the large the inter-string spacing and allows for the instrumentation of an extremely large volume. Due to the short scattering length on the other hand, photons will rarely reach a DOM without having been subject to scattering. This introduces a delay in arrival time compared to photons with a straight path to detection. Sophisticated reconstructions have been devised to calculate the most precise representation of a lepton path (and therefore original neutrino direction) from detected Cherenkhov radiation in the ice [E. Andres, 2000].

There are two types of interaction, neutral current (NC) and charged current (CC). Both are exchanges of weak gauge bosons. NC interaction occurs via Z channel resulting in an energy transfer between a neutrino and a lepton (provided by atoms in the ice). In CC interactions, neutrinos convert to the lepton of their doublet via $W^{+/-}$-exchange. This can produce electrons, muons and tauons. These three leptons produce three different event topologies in the detector. Electrons lose their energy fast by scattering and radiative processes and thereby can be detected as 'cascades', visible as compact, near-spherical bursts around the interaction vertex. Muons lose their energy slowly via cherenkhov light and scattering and can be seen as 'tracks', paths of light emission that can also enter or leave the detector. Tauons have a very short lifetime and can travel only a few (tens of) meters before they decay themselves. Tau neutrino events should be detectable as 'double bangs': one observes a shower both at the interaction vertex and at the position of tauon decay.

The energy of muons can not be perfectly reconstructed in the ice because muons usually don't deposit their full energy inside the instrumented volume. This is only the case if the track is fully contained in the detector. The long muon tracks point along the incoming neutrino path and can be used for a reliable directional reconstruction. For point source searches, this property is of cardinal interest, so a sample of muon tracks will be used for this analysis [Aartsen et al., 2017a].

1.4.1 Diffuse Astrophysical Neutrino Flux in IceCube

In [Aartsen et al., 2013a], IceCube reported the first evidence for an extraterrestrial neutrino flux. The analysis is based on 28 high energy starting events (HESE) including two cascade-like events above 1

[3] ν - nucleon cross section at $E_\nu = 1$ TeV : $10^{-35} cm^2$

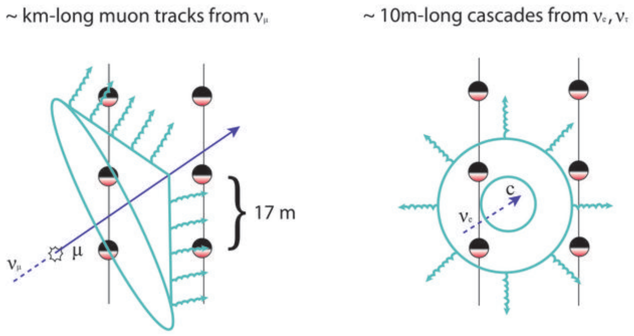

Figure 1.4: *Event topologies in IceCube. Long tracks are produced by muons and their progenitor neutrinos. Their long 'lever arm' makes them ideal for directional reconstruction. Cascades originate from electron and tauon CC or NC interactions. They often lose the majority of their energy in the detector, so this quantity can be estimated more precisely for cascades. Red bubbles are DOMs with early hits, green to blue are later charges on DOMs.*
(18-03-06, http://gallery.icecube.wisc.edu/internal/v/graphics/results/events_001_001/pastedGraphic.jpg.html)

PeV. HESE events have their interaction vertex contained in the detector fiducial volume. This provides an effective veto against atmospheric muons that enter from the detector boundaries. Restricting the event selection to >30 TeV removes most atmospheric neutrino background, as its spectrum is softer than the astrophysical neutrino flux.
In the data-taking period 2010-2012, only 11 atmospheric events would have been expected. Detecting 28 events excludes the background hypothesis at 4.1σ (see the reference for the calculation details). An update of the analysis can be found in [H.M. Niederhausen, 2017]: the per-flavour flux at 100 TeV is found to be

$$E^2\Phi(E) = (1.57 + 0.23 - 0.22)^{-2.48\pm0.08} \times 10^{-18} GeV/cm^2/s/sr$$

in the energy range between 12 TeV and 2.1 PeV.
A second approach uses muon tracks from the Northern hemisphere [C. Haack, 2017]. The atmospheric muon background is shielded by the earth leaving only neutrinos in the sample. A fit to the measured event spectrum can distinguish the different components: astrophysical, atmospheric, prompt (charmed meson decays). 8 years of data yield a significance of 5.6σ and a neutrino flux at 100 TeV of:

$$E^2\Phi(E) = (1.0^{+0.26}_{-0.23})^{-2.19\pm0.10} \times 10^{-18} GeV/cm^2/s/sr$$

The sensitive energy range is given by [119 TeV, 4.8 PeV]. Both results are compatible at high neutrino energies. At the given point, the tension between muon tracks and the latest cascade-only search diminishes [H.M. Niederhausen, 2017]. At high energies, both results are compatible: see Fig.1.5.

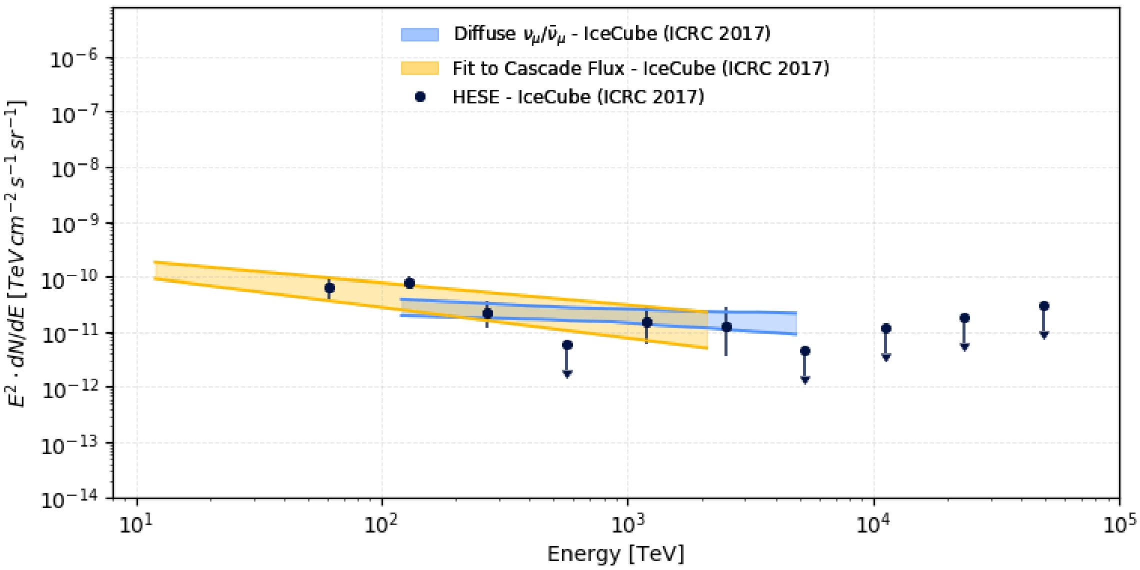

Figure 1.5: *Diffuse astrophysical neutrino flux as measured by IceCube. The orange area is the fit (+uncertainty) performed on High Energy Starting Events (for all flavours). The fluxes from single events, scaled to all-flavour, are shown as points. The blue area is the fit on muon track data. Both digress on a level of p-value = 0.04, but are compatible at high energies.*

1.5 The IceCube Realtime Alert System

A number of neutrino source candidates are transient sources (see the previous sections, or [Waxman and Bahcall, 1997] for GRBs). Therefore, deploying a system that recognizes events quickly is crucial for neutrino and multimessenger astronomy. The IceCube realtime alert system fulfils that purpose [M.G. Aartsen, 2017a]. It consists of five main 'streams': three follow-up streams (optical, X-ray, gamma-ray), the High Energy Starting Event (HESE) and the Extremely High Energy (EHE) alerts. HESE and EHE will be described in detail below. The follow-up streams are event selections configured to search for temporal[4] and spacial clustering of neutrino events. Signal events can be distinguished from background by their high energy and reconstruction properties (good angular resolution). The events are subjected to a multivariate classifier, a Boosted Decision Tree, that improves the distinction even further. There are two classifiers, one for each hemisphere (see Sec. 1.4), accounting for the differences in incoming events. In the optical and X-ray, neutrino multiplets within 100 s and a radius of 3.5 ° from each other are selected, leading to $\sim$ 5 alerts per year to partner telescopes. These can subsequently start their observations of the event origin to reveal a possible transient source.

1.5.1 GFU stream

The gamma-ray follow-up[5] is a program to facilitate coincident detections of IceCube neutrino bursts with highest-energy photon events. IceCube is a 4π-detector with nearly 100% uptime, but current Imaging Air Cherenkhov Telescopes (IACTs) suffer from narrow fields of view. They are limited to

[4] 100 s scale for optical, 3 weeks for GFU

[5] Reference and an extensive introduction to the entire topic can be found in [The IceCube Collaboration, 2016], here only the relevant aspects will be treated.

few tens of square degrees[6]. Rare neutrino multiplets and their direction need to be relayed to them quickly, so IACTs can direct their field of view in a way that allows simultaneous observation. It is therefore essential to notify such experiments in real time.

IACT observation time is limited to clear nights. This forces those experiments to make economical decisions on their scheduling, and only high-quality reliable alerts can be followed. To reduce the number of fake background alerts from IceCube, a pre-selection of 184 sources is made that mark targets for the IACT observatories. Apart from galactic sources, those consist of blazars known to exhibit variable behaviour and exceed certain quality thresholds.[7]

On the IceCube side, the GFU employs neutrino selection schemes following closely the selection in [Aartsen et al., 2017a]. Those techniques are commonly used and typical for point source neutrino samples as signal/background filters. A single multiplicity trigger, activating data acquisition upon at least eight hit DOMs in a narrow time-window (SMT8) reduces the raw data. It is followed by the *Muon Filter* algorithm based on Linefit and SPE fits as described in [E. Andres, 2000] to identify muon events. The events surviving these cuts are still background-dominated, so the MPE-seeded Online Level2 selection is applied. Level2 selects muons with probably astrophysical progenitor neutrinos by quality cuts to the muon reconstructed tracks and gives a single-event angular uncertainty. The resulting sample has a median angular resolution of $0.5°$ and a rate of about 2 mHz for an E^{-2} spectrum.
To this sample, a time-clustering algorithm is applied that searches for correlated events with a Poissonian Likelihood Approach in 21-day windows for an unbiased flare search. Alerts are generated based on a total likelihood combining the time-clustering with a spacial clustering around a source as shown in Fig.1.6.

1.5.2 HESE and EHE alerts

High energy starting events (HESE) and extremely high energy (EHE) tracks are among the rarest types of neutrinos regularly observed in IceCube.[8] The first HESE events were for a while the most interesting result of neutrino astronomy (fig 1.7 or [Aartsen, 2013]). The HESE selection consists of high-energy events of both cascade and track topoloy that have their interaction vertex inside the detector. The selection vetoes events at the detector boundaries to remove entering muon events. This means that the remaining events have to be of neutrino origin and are most likely astrophysical due to their energy. In consequence, this channel is almost background-free, containing a large fraction of astrophysical events - a fact that warrants attention by follow-up searches in all wavelengths. Yet because of their large error circle, HESE cascades are hard to directionally reconstruct. This effectively disqualifies those for alerts. Only HESE tracks with a minimum track length of 200 m are sent out. Their angular uncertainty is calculated in real time and added to the notice to constrain the search radius for the follow-up partner observatories.

[6] https://magic.mpp.mpg.de/
https://www.mpi-hd.mpg.de/hfm/HESS/
https://veritas.sao.arizona.edu/about-veritas-mainmenu-81/

[7] z<0.6, flux thresholds in the dominant energy regions for BL Lacs and FSRQs respectively and a cut on Fermi spectral index for BL Lacs

[8] Tau-induced double bang events are not yet detected, the existence of detected Glashow resonance events is under investigation at the moment.

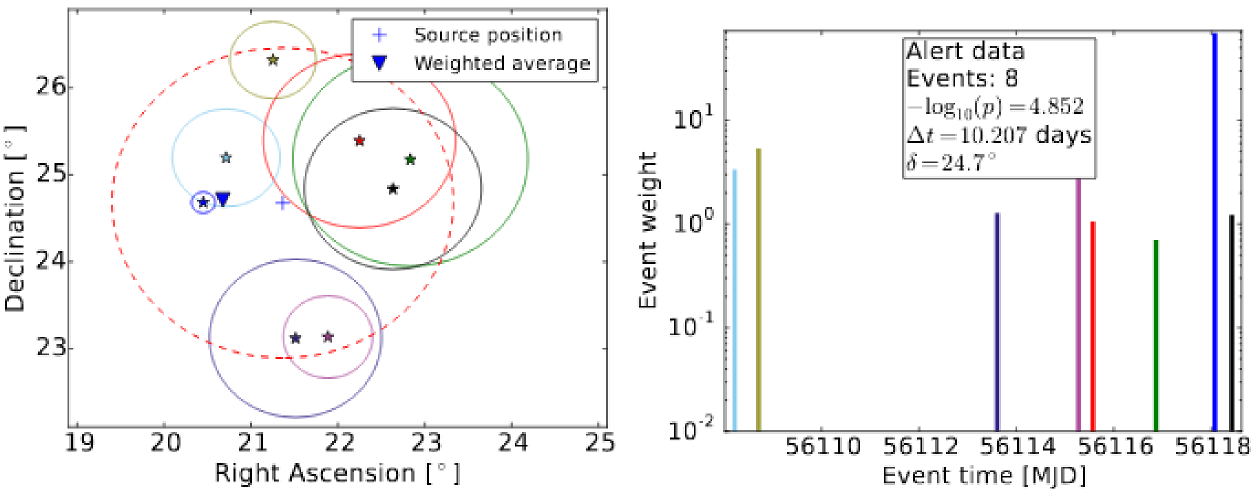

Figure 1.6: *GFU test alert of 8 events detected within 10.2 days. The left plot shows the spacial, the right the temporal distribution of events contributing to the alert. The circles on the left depict the angular uncertainties. The bar height on the right proxies the single-event weight. The source is one of the 184 known variable gamma-ray sources marked as suitable targets for the Imaging Air Cherenkhov Telescopes. Taken from [The IceCube Collaboration, 2016]*

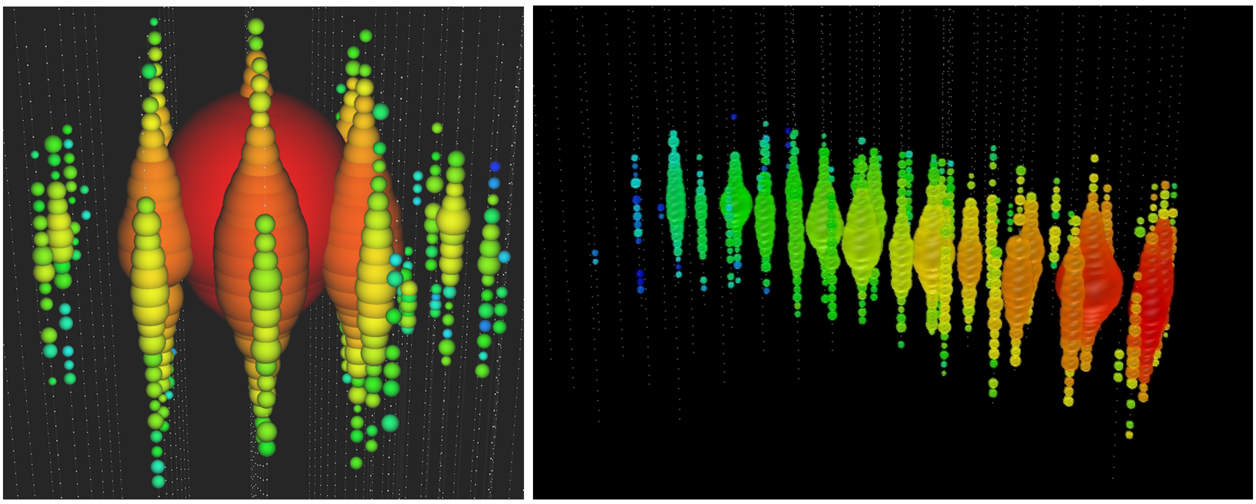

Figure 1.7: *Left: High Energy Starting Event of cascade topology found by IceCube in 2014, dubbed Big Bird. [18-03-08 http://icecube.wisc.edu/news/view/292] Right: track-topology event released in Science in November 2013 [18-03-08 http://icecube.wisc.edu/gallery/press/view/1964]*

The EHE selection is based on an analysis searching for GZK neutrinos from the cutoff in the cosmic ray spectrum.[9] The necessary cuts are easy to implement Online (at the pole): muon tracks with a good angular resolution $< 1°$, at least 300 hit DOMs and a deposited charge of $> 10^{3.6}$ photoelectrons to maximize sensitivity between 500TeV and 10PeV. Because this does not *a priori* guarantee a good background distinction, there are secondary cuts in place, the most important one on the combined zenith and energy pdf of the events. The remaining events can be used for very accurate directional searches (angular resolution $\sim 0.22°$) and show up with a rate of only ~ 4.25/year. EHE events are well-reconstructed tracks at highest energies, possibly pointing back at the most powerful neutrino sources in the universe. It is therefore essential for the multimessenger community to be notified about those rare occurrences.

[9] The energy of the cosmic rays can exceed the threshold for a reaction with the CMB photons, resulting in CR-disintegration above $\approx 10^{20} eV$ [Greisen, 1966] [Zatsepin and Kuz'min, 1966], possibly producing neutrinos at high energies.

Chapter 2

Follow-up on IceCube-170922A

2.1 IceCube-170922A

On September 22nd 2017, 20:55:13 UT, IceCube issued a GCN alert via AMON[1], stating that there has been an EHE event detected by IceCube - by convention named IceCube-170922A. The online event reconstruction was followed by an automated improved processing, which gave a direction of RA 77.43° DEC 5.72° and an energy of $\sim$ 120 TeV. The relevant properties sent out with the alert or as a GCN circular[2] four hours after are shown in table 2.1.
AMON is network of high-energy, multimessenger and follow-up observatories distributing candidate transient events in near-realtime, facilitating the search for shortlived events in the sky that are of high relevance to fundamental physics and astronomy [Smith et al., 2013]. It contains IceCube EHE events because of their good reconstruction and energy, which makes it likely for them to point towards an interesting source. They are very rare occurrences - 2017 saw only three EHE events in total (see Sec. 1.5), expected are four per year [The IceCube Collaboration et al., 2018]. Other events sent via AMON are HESE tracks and neutrino track multiplets from the GFU stream.

[1] https://gcn.gsfc.nasa.gov/amon.html
[2] https://gcn.gsfc.nasa.gov/gcn3/21916.gcn3

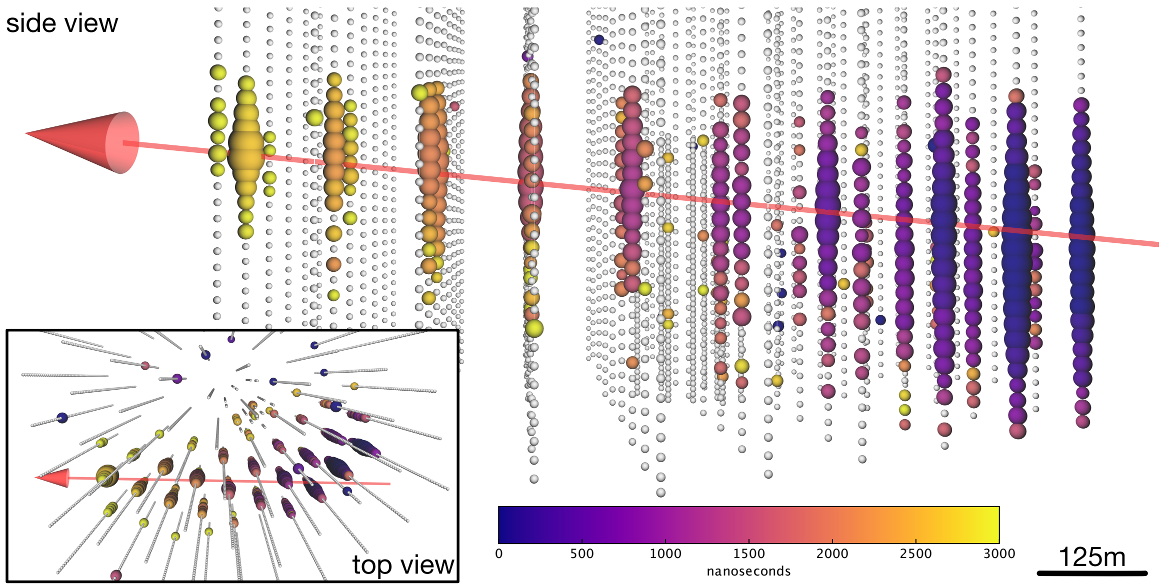

Figure 2.1: *IceCube-170922A - EHE event that triggered an Extremely High energy event alert on Sept. 22nd 2017 - within the IceCube detector. Shown are the Digital Optical Modules of IceCube (white spheres) located on the vertical strings in the ice. DOMs with a signal response ('hit') are coloured corresponding to the arrival time of the light at the DOM, the size of the bubbles corresponding to the charge collected by the module. All hit DOMs form a trace of the muon track that resulted from the neutrino event interacting outside of the detector. From [The IceCube Collaboration et al., 2018].*

Table 2.1: *Properties of the neutrino EHE event IceCube-170922A as stated in the GCN circular on Sept. 22, 2017. GCN Circular errors are 90% PSF containment, coordinate system is J2000 for both alert and circular.*

property	GCN alert	GCN Circular
RA	$77.2853° \{+05h09m08s\}$	77.43° -0.80 /+1.30°
DEC	$+5.7517°+05d45'06"$	5.72° -0.40 /+0.70°
Angular error [50%]	14.99	
Energy	1.1998e+02 TeV	
Signalness	0.56507	
Charge	5784.9552 pe^3	

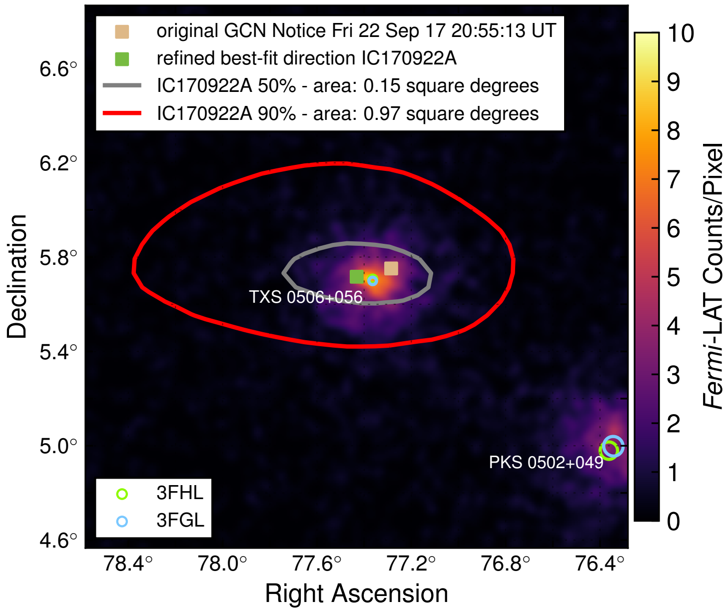

Figure 2.2: *Skymap showing the uncertainties of the event reconstruction of IceCube-170922A, overlaying the gamma-ray profile as measured by Fermi (Maximum-Likelihood fit of available Fermi-LAT data above 1 MeV). Additionally, the locations of the blazar TXS 0506+056 in the event uncertainty region is shown, and the reconstructed direction given in the GCN. From [The IceCube Collaboration et al., 2018].*

Upon report of a flaring source candidate by the *Fermi*-LAT Collaboration[4] (see sec 2.2 and [Tanaka et al., 2017]), the event was again reexamined, yielding a deposited energy of 22 TeV, a total energy of 290 TeV and a recalculated signalness[5] of 48±0.04% [The IceCube Collaboration et al., 2018].

2.2 TXS 0506+056

Following up the alert IceCube-170922A, the *Fermi*-LAT collaboration reported a known blazar in the event error circle [Tanaka et al., 2017]. This source candidate, TXS 0506+056 (referred to as TXS), is a known BL Lac object also listed in the 3FHL catalog [Ajello et al., 2017] as 3FHL 0509+541 with previous periods of variability. Blazars which are detectable in gamma-rays by Fermi are good candidates for neutrino sources. The neutrino production mechanisms are believed to parallelly produce photons, and a high flux in those gamma-ray photons might hint at a high neutrino flux. The TXS gamma flux is extraordinary (see fig 2.3 and 2.7) even in the *Fermi*-LAT integrated measurement in the 3FHL.

It also displays variability in gamma-rays. Notably, it was in an active state during the arrival of the alert event IceCube-170922A. It has not shown neutrino emission above the detection threshold in the 7 years point source search, time-integrated all-sky [Aartsen et al., 2017a]. With more data or using its flaring as a trigger, it is still possible to find a significant neutrino point source at this position - despite a non-detection in the time-integrated search. The blazar stacking limits calculated by IceCube do not restrict detection: they are only valid for the full population and do not rule out single or multiple blazars as neutrino sources.

[4] https://fermi.gsfc.nasa.gov/

[5] This value denotes the probability of an event being an astrophysical neutrino, induced from its energy and incoming zenith angle.

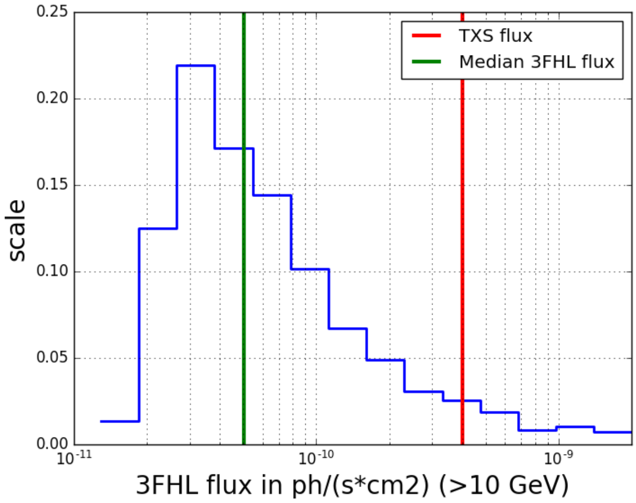

Figure 2.3: *Histogram of the average photon flux (10-2000 GeV [Ajello et al., 2017], in gamma rays) of all sources in the 3FHL. The green line shows the median flux, the red line the TXS 0506+056 flux. The fraction of sources that are gamma-brighter than the TXS 0506+056 is small (less than 7%), so not only is the possible counterpart to an EHE event a known blazar, it's also an outstanding object in the population. This statement should in general be taken with caution since any measurement of flux in a certain band depends on the exact shape of the blazar spectral energy distribution.*

TXS is a intermediate-peaked-BL Lac (IBL) object in quiescent state - its synchrotron peak is at $10^{14.4}$ Hz, therefore in the range of $10^{14} - 10^{15}$ Hz (compare Fig.2.4 and 2.6). In active state, the peak shifts to higher energies. It therefore classifies as IBL/HBL.
The peak position ranking also applies to their detectability in gamma-rays: the shape of the typical blazar SED in the HBL case displays its second hump at HE (Fermi band) to VHE energies (IACTs). Shifting the second peak to lower frequencies/energies draws the downwards slope of the hump into the instruments' band, thus visibility for current-generation gamma-ray telescopes is smaller for smaller synchrotron peak frequencies. As an IBL/HBL, TXS was already detected in gamma-rays by Fermi, allowing variability monitoring via FAVA[6] [S. Abdollahi, 2017] and could in high state be detected by ground-based Imaging Air Cherenkhov Telescopes following up the EHE event, first by MAGIC [Mirzoyan, 2017].

Having a complete picture of a candidate source in gamma-rays is even more rare [The IceCube Collaboration et al., 2018]. Up to that point, the redshift of the object was not known precisely, but later determined to $z = 0.34$ using the 10.4 m Gran Telescopio Canarias by [Paiano et al., 2018].

Multiwavelength Picture of the TXS 0506+056 VOU-Blazars [Chang, 2018] is a tool which provides a multiwavelength (planned for the future: multimessenger) view of any sky window, and searches for blazar-like objects and candidates through >30 catalogs that are publicly available, including *Fermi*-LAT and IACT gamma-ray data (if available). The sky around the TXS scanned for blazars can be found in Fig. 2.8. There is one additional source in the vicinity which is a known blazar, PKS 0502+049. It is an FSRQ, therefore not a priori a good neutrino or cosmic ray source [Resconi et al., 2017]. Its SED is shown in the appendix, Fig. A.3. One can see that its photon flux

[6] https://fermi.gsfc.nasa.gov/ssc/data/access/lat/FAVA/

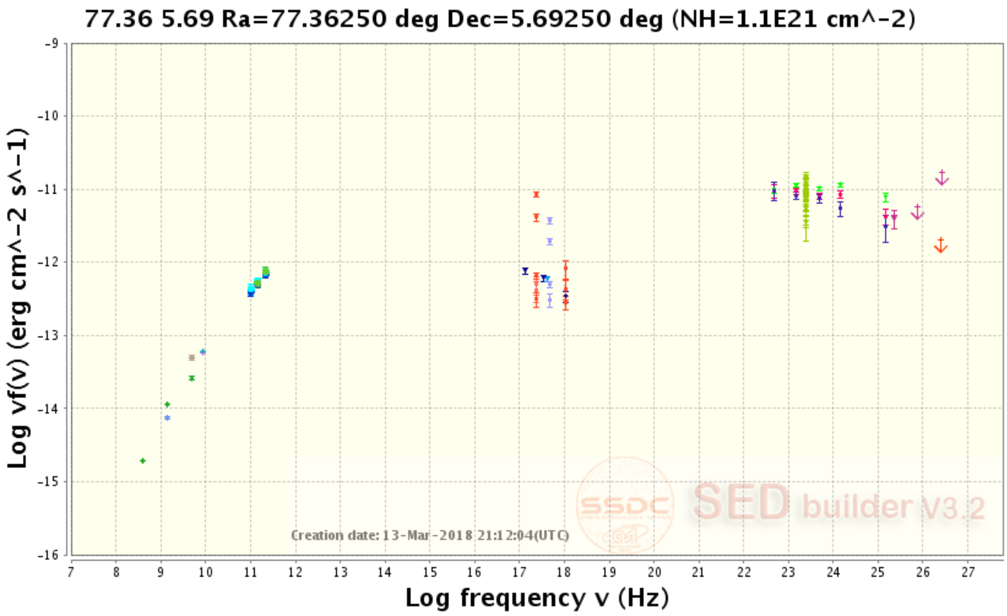

Figure 2.4: *Spectral energy distribution of the TXS 0506+056 from http://www.openuniverse.asi.it/ as by Oct. 2017. Different colors mark observations from different observatories. It has been detected and catalogued in radio/infrared, X-ray and in high-energy gamma rays. The two humps are recognizable: the X-ray band is clearly variable as it has a band of flux values for given x-ray frequencies. The synchrotron peak seems to lie in the low optical (also νpeak, here around $10^{14}Hz$). A more detailed SED is shown in [The IceCube Collaboration et al., 2018]. If one would shift the second hump to higher energies, keeping the flux the same, the flux in a small band around $10^{25}Hz$ would increase: it would catch an area closer to the peak flux. This is one possibility how gamma flux increases during a flare, the other is a simple shift of the whole curve upwards in flux. This figure shows the information that was available at the time of the alert, a more complete plot can be found in Fig. 5.4, also including the neutrino flux of the object.*

drops too quickly in the very high energy regime to be a target for current-generation IACTs.

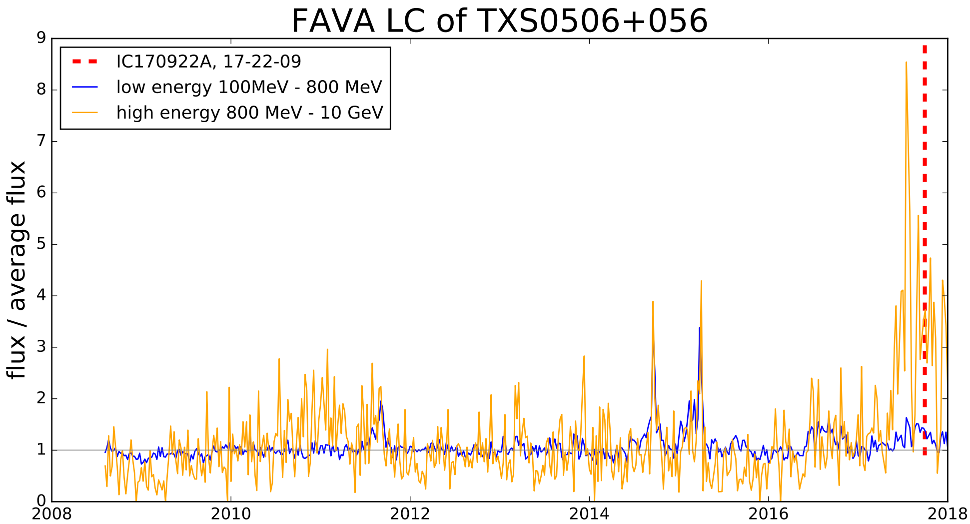

Figure 2.5: *Gamma-ray lightcurve of the TXS 0506+056 from weekly FAVA data [S. Abdollahi, 2017]. The curve starts with Fermi LAT data taking in 2008 and ends with the neutrino sample endpoint used in the analysis presented in this work. One can see that for the last section in 2017 (starting in May), the TXS source is in a high state in gamma flux.*

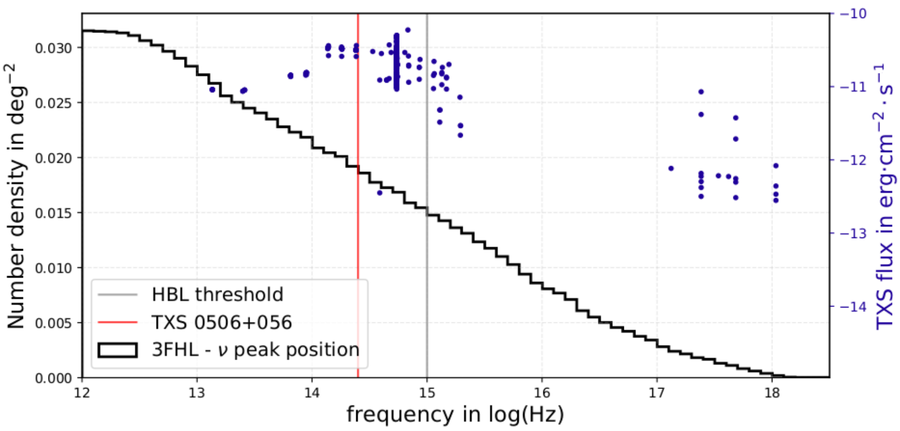

Figure 2.6: *3FHL ν peak distribution. In black is the number density of 3FHL [Ajello et al., 2017] sources sorted cumulatively by their synchrotron peak position in frequency. HBL sources are to the right of the grey line. Even though the TXS 0506+056 is not an HBL source in quiescent state - as illustrated by the red line and the SED (blue, second axis) - it is still detectable in VHE gamma rays in flare. This makes it a potential neutrino source [The IceCube Collaboration et al., 2018]. Its behaviour can be interpreted as an indication that time-integrated observations and the exclusion of steady emission models only provide limited insight in blazars. Some gamma-bright objects like the MRK 421 seem to emit below-threshold in neutrinos [Padovani et al., 2015]. Low-luminosity objects in gamma-rays are apparently capable of short-duration bursts in gammas and hopefully neutrinos. A correlation between the highest-energy photons and astrophysical neutrinos is still likely to exist, but the exact manner of the connection requires careful examination.*

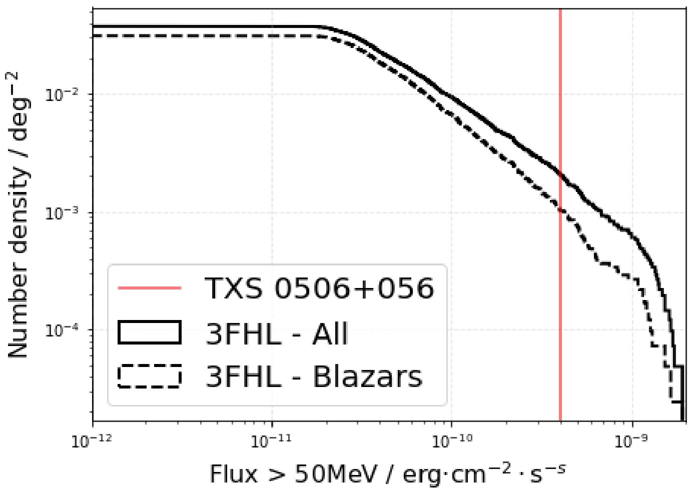

Figure 2.7: *3FHL flux distribution. The number density of 3FHL [Ajello et al., 2017] sources binned cumulatively in their flux is shown for all objects as well as only the identified blazars. In contrast to Fig.2.6, the TXS 0506+056 is a rare object in terms of its flux. Indeed its flux in the different wavebands is at the same level as the MRK 421, a blazar ten times closer to us. Original by A. Turcati, reproduced with permission.*

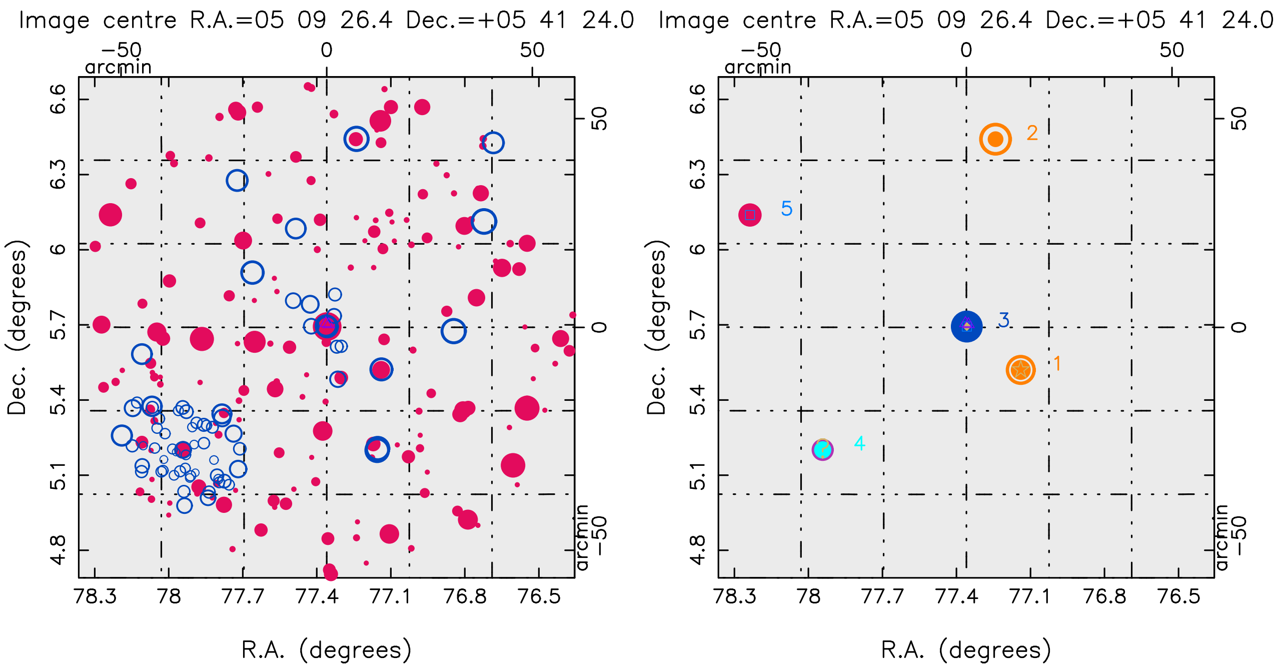

Figure 2.8: *View of the region around TXS 0506+056 (center in both) with the VOU-Blazars tool. On the left is the full image with all radio and X-ray sources. On the right is the same image filtered for blazars by applying constraints to X-ray and radio band emission and searching online for existing associations. Each match is displayed as a symbol referring to a certain catalog, red circles mark radio, blue circles X-ray sources. In the direct vicinity of the TXS, there is the source PKS 0502+049 (nr. 1) at RA 76.35 DEC 4.99, which is a known FSRQ. There are no other catalogued blazars in the area.*

2.3 The Neutrino Sample

In IceCube, neutrino induced through-going muon tracks are preferentially used for point source searches. They can be directionally reconstructed for full and partial containment in the detector volume, effectively increasing the interaction volume beyond the instrumented part of the ice [Aartsen et al., 2017a]. IceCube can detect neutrinos from all directions on the sky sphere, but there are differences between the Northern and Southern hemispheres (see Sec. 1.4 and Fig. 2.10). In the south, atmospheric muons are the main source of background. To filter them, one looks for other muons from the same air shower and vetoes the coincident detection of muon bundles. In the north, atmospheric muons are shielded by the Earth and this background type is suppressed. Still, there are atmospheric muons from the south that are misreconstructed as upgoing (coming from below the detector, thus from the earth shielding), which are irreducible background for Northern Hemisphere event reconstruction. The rate of both background types exceeds by far the expected signal rate from astrophysical neutrinos. For both hemispheres, the spectrum of signal astrophysical neutrinos is expected to be harder than the respective background, aiding further distinction. In the North, neutrinos at highest energies are rare as the interaction cross section rises with the neutrino energy. Up-going events traverse a long distance of high matter density - travelling through the Earth - and have their chance to reach the detector decreased [Aartsen et al., 2016b] [Coenders, 2016, p68ff].

The 7 years point source sample[7]. includes the years 2008-2014 (IC40, IC59, IC79, IC86, IC86_II-IV by detector seasons).[8] Detector configurations differ in acceptance, therefore each has its own Monte Carlo simulation set (MC) and has to be treated separately for sample generation and analysis. In the last three periods, the MC did not change anymore, making it possible to summarize 3 years into one season. These five subsamples of track selection are in detail described in [Aartsen et al., 2017a]. The gamma-ray flare of the TXS 0506+056 happened in 2017. The 7 years point source sample does not cover this time window where one would expect signal if the gamma-ray emission is hadronic. Aiming to identify a neutrino point source, a method to cover the remaining 2.5 years was found. The IceCube gamma-ray follow-up GFU [M.G. Aartsen, 2017a] [The IceCube Collaboration, 2016] provides a track selection with the same purpose and a very similar, yet slightly improved event selection as 7yrPS. It can be processed into an equivalent sample of muon track events. With coverage up until October 31, 2017, it has exactly the properties one needs for the analysis and can easily be merged with the existing 7yrPS sample (see Fig.2.9). After the initial unblinding, an update with 0.5 years of additional GFU data has been performed.

In total, 9.5 (update: 10) years of muon track data have been prepared for this analysis and future point source searches.

2.3.1 Reconstruction and Pull Correction

IceCube reconstructions are nominally divided in stages called levels (LX with integer X). The nomenclature starts at L1 for the trigger processing, L2 denotes the filtering of atmospheric background. L3 is an event selection that is specifically designed for certain types of analyses. Sometimes L0 is used to refer to raw pulses data, and L4 can denote the analysis-ready processed data.

[7]abbreviated: 7yrPS

[8]Each season starts in late spring, so the last year extends into 2015.

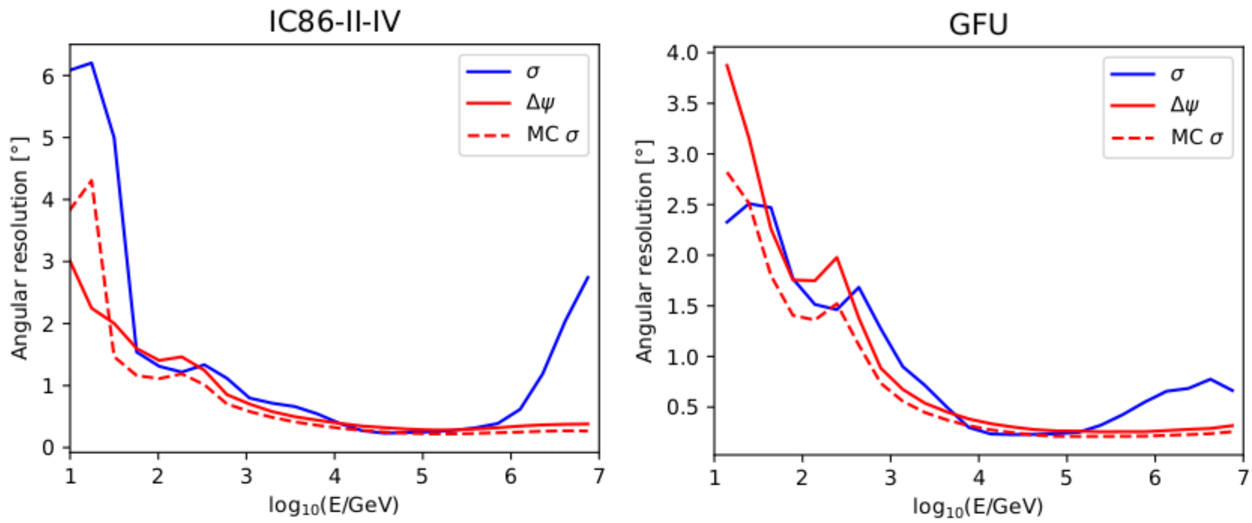

Figure 2.9: *Angular resolution of the events over energy for the two largest subsamples: IC86_12-14 and the GFU (2014 to October 2017). One subsample is defined as all runs sharing the same Monte Carlo simulations. The red dashed line is the MC angular resolution, the blue line is the one for the reconstruction. For low-energy events, the light yield in the detector is small and the precise track reconstruction is hard. Therefore, the resolution at low energies is worst, but getting better to higher energies. The red line is the median difference between simulated and reconstructed angle per event. It follows the reconstructed resolution closely, validating the method. Between the two samples is very little difference as they rely on the same set of basic cuts and reconstruction method.*

Reconstruction Schematics

The L1 background rejection techniques are in detail described in [E. Andres, 2000, Sec. 6] as they are inherited from the predecessor experiment AMANDA. They are used with little modification in IceCube.
The L2 selection is composed by a series of cuts and basic fits. It starts with a cut on the total event charge (number of photo-electrons in the detector). Events lacking sufficient energy are discarded. Then, specific cut variables are calculated and applied. All basic reconstruction fits are then performed with the cleaned track events. Using the track fits and resulting track characteristics, background is then further reduced by applying cuts (on the variables (b) to (f), see below).
The L3 selection applies a *SplineMPEparaboloid* fit to improve the L2 reconstruction and estimate angular uncertainties for each event (see below).
The resulting sample is processed by a multivariate selection, so called Boosted Decision Trees (BDTs), which on the final level lead to a rejection of 99.94% of background muons while retaining 90% of the signal [Coenders, 2016].

In the frame of this work, an L3 event reconstruction tool has been implemented[9]. It includes a reprocessing of the basic event direction fits after the IceHive Module cleaned the sample from potential noise clusters[10].
The filters and fits used are in detail described in [E. Andres, 2000] and will only briefly be described

[9]http://code.icecube.wisc.edu/projects/icecube/browser/IceCube/sandbox/bkrammer/bootcamp - Access restricted to IceCube members.
[10]The original idea for the selection has been developed by Kai Krings. The implementation was performed in collaboration with Maximilian Kronmüller.

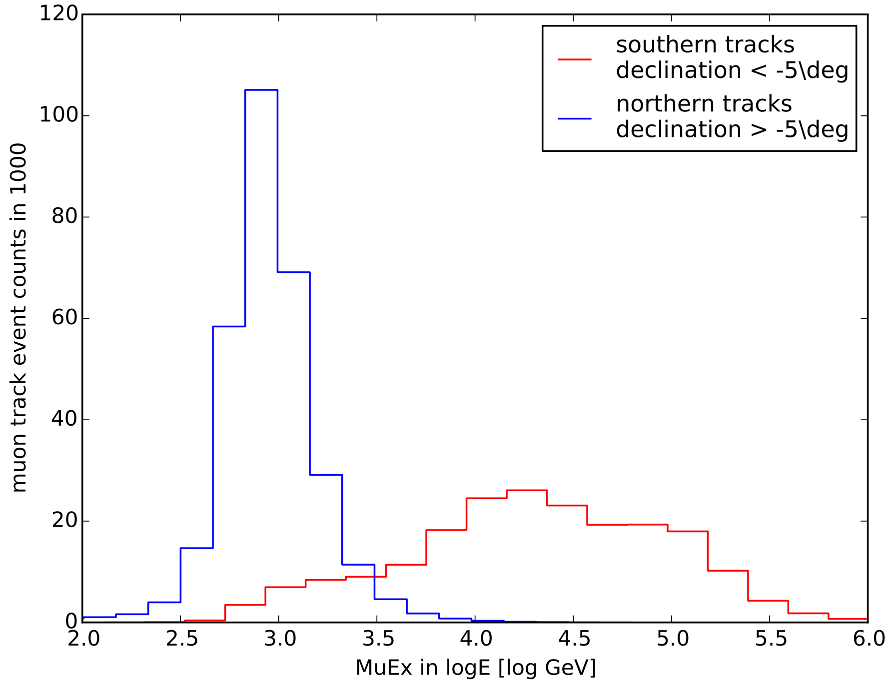

Figure 2.10: *Countrate (indicating Acceptance) over Energy of the GFU data events after the selection process for the entire 2.5 years. The x-axis shows MuEx, the energy proxy from the IceCube reconstruction, which can be used as a lower limit to the actual track energy for partial deposition. One can see the difference between Northern and Southern selection clearly: the south has more high-energy neutrinos which get filtered by the earth in the Northern Hemisphere, the north is less background-contaminated and therefore can safely use lower-energetic events because they are unlikely to be of atmospheric origin.*

here. A complete sample selection can be found in [Coenders, 2016, chp. 4.6f, chp. 6]. To make use of the high number of events, a sample for a point source search should be executed on muon track events. Therefore the starting point is a large sample of data events that passed the *Muon Filter* or *EHE Filter* (see Sec. 1.5). After a first selection of candidate tracks, improved reconstruction is applied: tracks are fitted with a Multiphotoelectron (MPE) fit [E. Andres, 2000] including splined photon time residuals due to ice properties.

Cut Variables

During processing, the events are first filtered by their total charge deposited in the detector, then a standard set of cut variables is calculated:

a) Average Charge-Weighted Distance of Closest Approach (AvgDist)

b) Hit Multiplicity

c) Hit Statistics

d) Direct Hits

e) Track Characteristics

f) reduced log-Likelihood (rlogL)

AvgDist (a) is the distance of each hit DOM[11] to the best-fit track reconstruction weighted by the DOM charge. A large value here means that the reconstruction deviated from the line of closest approach to all charges. If a fit disagrees strongly with this analytical 'first guess' of the track, the event is likely noise-dominated or not track-shaped. Ideally they would align almost perfectly.

Quantities (b)-(e) help to select and remove noise events with irregularities that make them pass the previous cuts, for example a 'track' where a high charge comes from one DOM: the event is reported as 'good' due to high charge. The fit finds a fake track through that DOM and a cluster of noise events somewhere in the detector. The four hit variables show that both components (DOM and cluster) are by themselves not relevant. The high-charge DOM is not track-like, the noise cluster has little charge. This pseudo-event is marked and can be cut on.

Direct hits (d) are an important quantity for signal/noise distinction: photons that are not scattered in the ice and directly hit an optical module are the most reliable traces of an event. Based on the Best Track one can calculate which photons had the minimal travelling time between emission and detection.

Track characteristics (e) contain the 'empty length' - if a track consists of two clusters of hit DOMs with a long stretch of no detection in the middle, it is unlikely to be a real single track. Instead it might be two coincident events.

The reduced log Likelihood (f) is the fit LLH normalized to the number of deposited charges and can be used as a measure of the fit quality. *LineFit* is assigned an arbitrary, large value to account for it being a fallback fit in this context.

The Best Track is chosen from the four fast likelihood reconstructions *MPEFit*, *SPEFit2*, *SPEFitSingle* and *LineFit*. The sophistication of the algorithm decreases from first to last. *LineFit* is an analytical calculation of the line with the lowest charge-weighted distance to all hit DOMs. *LineFit* has the advantage that it can run Online (at the South Pole) very quickly in spite of the limited computing resources. *SPEFit*s ('single photo electron' likelihood fits) derive a track based on the likely arrival time of the first photon at a DOM. They take the *LineFit* as a seed, and the second *SPEFit* is an iteration seeded with the first *SPEFit*. The *MPEFit* also includes later photons and takes the *SPEFit* as a seed.

Event Angular Uncertainty

The event angular uncertainty in the point source and GFU samples is derived by fitting a paraboloid to the reconstruction likelihood space and using the opening angle of the parabola to approximate the angular uncertainty on the arrival direction. *MPEFit* tends to underestimate this uncertainty at high energies where it does not account properly for stochastic energy losses [Aartsen et al., 2014]. Reconstruction algorithms that treat stochastic energy losses precisely have been implemented in IceCube. Applying those to the entire sample is not feasible though - they are computationally too expensive. This issue can be mitigated by pull correction. 'Pull' refers to the too-small *MPEFit* angular uncertainty estimate. This is introduced by the *MPEFit* not treating stochastic losses of muons entirely correct. The pull correction is an approximation that has been optimized on MC. The

[11] A DOM that detects at least one photon.

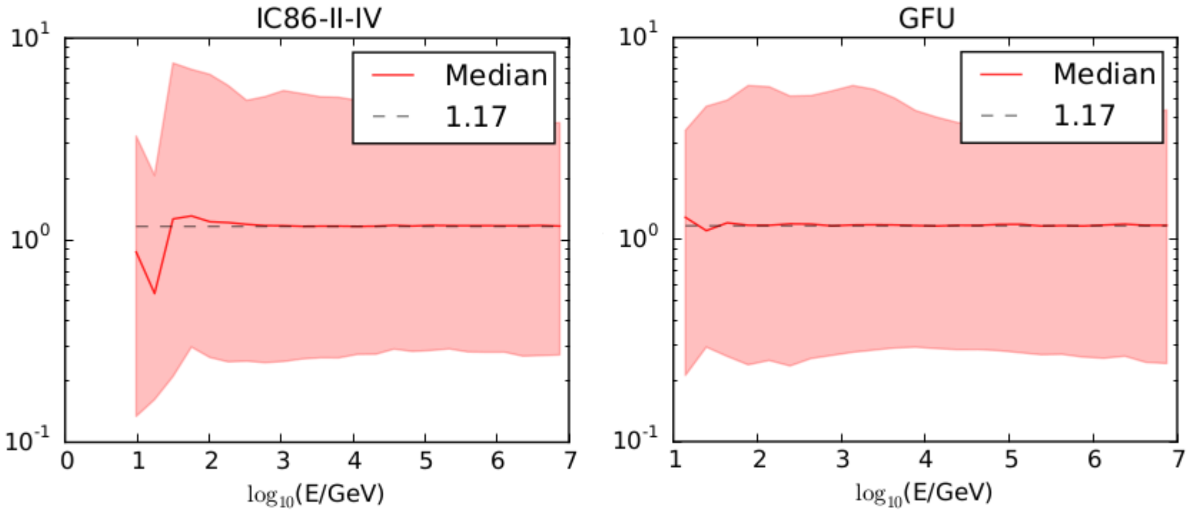

Figure 2.11: *Per-event angular resolution of the two latest subsamples as 90% CL bands. The red line shows the median over energy. Dashed is the value to which the median was normalized. The lowest-energy bin displays fluctuations since the reconstructional uncertainty there is too large to be fully accounted for. IceCube has not yet detected data events beyond 10 PeV, so the plot is cut there.*

distribution of angular uncertainties is corrected so that the median shifts to 1.1774. This number is the proportionality factor between a 2D-Gaussian's standard deviation (desired uncertainty) and the median (sample property). The procedure for this is fitting a curve[12] through the median angular resolution over energy for the entire energy range of the sample. Then a renormalization is applied to the median angular resolution by the curve value at each energy. Consequentially, the highest and the lowest energies are not perfectly described by the fit, but the effect is small. In the high-energy regime above 3 PeV, IceCube has not yet detected track events. MC events in this regime are described only approximately, but the real data is unaffected. In the low energy range, reconstruction quality drops, but events at these energies have a high probability to be background-like. Those will have little impact on the analysis in a point source search. An example for this behavior is shown in Fig. 2.11.

[12]Polynomial of order 6.

Chapter 3

Analysis and Methods

The analysis used in this work is optimized to find signal clusters over isotropic background. In a nutshell, every event is assigned a probability to be signal or background based on its angular distance to the source position and reconstructed energy. A fit of the total likelihood is performed. A proxy of signal strength ('Test Statistics value') is obtained. A p-value is calculated by counting fluctuations of the same 'signal' strength in pure background: a set of random skymaps determines how unlikely it is to observe the observed signal in a no-signal case by chance. The method is identical to the one used in [Aartsen et al., 2017a].

3.1 Likelihood formalism

Point-like neutrino sources should reveal themselves as spacial clusters of events around a source position. In the case of source variability, signal can also arrive time-clustered. Atmospheric background is emitted isotropically. This section will answer the following questions:

- How does one define (and quantize) a correlation between an event and a source?
- How does one treat the background-contaminated sample to optimally extract signal?
- What is the expected number of background events for the source position?
- How to evaluate significance? When to claim a detection?

A simple counting experiment will not lead to a satisfactory answer. Instead one would like to assign weights to single track events that are determined by the physically motivated weights - a spacial weight and an energy weight.

The resulting procedure is called 'unbinned maximum likelihood formalism'. Each event in the sample is assigned a probability weight to originate from the source. In the case of a neutrino point source search, the weight is composed of a spacial term that quantifies the distance source-event, and an energy term. This takes into account the reconstruction angular error estimate and that high-energy tracks are more likely to be of astrophysical origin. The fact that astrophysical neutrinos are supposed to follow a harder spectrum than atmospheric background and therefore dominate at high energies is useful to distinguish signal.

A fit of the Likelihood Ratio of the hypotheses is performed:

$\mathcal{H}0$: The data is compatible with pure background.

$\mathcal{H}1$: The data contains background and astrophysical neutrinos from the source position.

Each event contributes fractionally to the Likelihood Fit, yielding a best-fit result for the number of total signal events over background in $\mathcal{H}1$. The chance to obtain a given signal strength by random background fluctuations is quantified as a p-value. The procedure performs better than a binned or pure counting approach [Braun et al., 2008].

3.1.1 Event weighting

To determine whether events cluster around a source position, two aspects have to be treated: the first is the angular distance of an event to the source. For putative signal events this is realized by a Gaussian penalty term with the angular distance as the argument and the event uncertainty as the variance. This gives a measure of how likely an event originates from the source knowing its reconstructed direction. A Gaussian approximates the per-event reconstructed directional likelihood space well. In consequence, well-reconstructed events are preferred by the weighting, and the closer an event in units of its angular error, the higher its weight. Background events are distributed isotropically. The IceCube acceptance is uniform in rightascension and only varies in declination δ. The respective background probability therefore depends on $sin(\delta)$.

The second aspect is the event energy. Both background and signal event energies follow certain distributions that are assumed to be described by powerlaws of the form $d\phi/dE \sim E^{-\gamma}$ with the energy E and the spectral index γ. The background consists mainly of atmospheric events with a soft spectral index of $\gamma = 3.7$ while the signal distribution depends on the source. Since the source candidate emission is not known *a priori*, this is left as a free parameter to be determined by the analysis. The spectral index of the total astrophysical flux is harder than that of atmospheric background, so high-energy events are more likely to be signal in general. The signal and background probabilities for one single event then look like:

$$\mathcal{S} = \frac{1}{2\pi\sigma_i^2} e^{-\frac{|x_S - x_i|^2}{2\sigma_i^2}} \times \mathcal{E}_\mathcal{S}(E_i, sin\delta_i, \gamma)$$
$$\mathcal{B} = \frac{\mathcal{P}_\mathcal{B}(sin\delta_i)}{2\pi} \times \mathcal{E}_\mathcal{B}(E_i, sin\delta_i)$$

where $\mathcal{S}$ is the signal probability, $\mathcal{B}$ is the background probability, σ_i is the event angular uncertainty, x is the position of the source s or the event i, $\mathcal{E}$ is the energy-dependent term and $\mathcal{P}_\mathcal{B}$ the background probability differential in declination. $\mathcal{P}_\mathcal{B}$ will be derived from data (see Subsec. 3.1.2).

Now that expressions for the signal and background probabilities have been defined, one can combine them into the likelihood of **event i** originating from **source s** for all events. The signal and background probabilities for one event can be combined linearly into one likelihood term $\mathcal{L}_i$. Each term is parametrized by the fraction of signal events n_s with respect to all events N. n_s is a free parameter in the fit. This quantity is unknown and has to be determined by fitting. The total likelihood for the source is the product of all N event likelihoods and depends on two free parameters, the number of signal events n_s and the source spectral index γ [Braun et al., 2008].

$$\mathcal{L}(n_s, \gamma) = \prod^{N} p_i(\mathcal{S}_i, \mathcal{B}_i)$$
$$\mathcal{L}(n_s, \gamma) = \prod^{N} \left(\frac{n_s}{N}\mathcal{S}_i + \left(1 - \frac{n_s}{N}\right)\mathcal{B}_i\right)$$

To find the parameter set corresponding to the excess of neutrino events at the source, one maximizes $\mathcal{L}$.[1] A large value of the resulting maximum likelihood indicates high signal strength. The fit parameters are correlated and contain physical information. A source with a hard spectrum (small γ) will send few high-energetic signal events and a soft-spectrum source will display high emission in comparably low-energetic neutrinos. From both values, a neutrino energy flux from the source can be calculated.

So far, one homogeneous sample can be treated with this formalism, but the muon track data consists of different detector seasons and configurations. Each of those has a different effective area and neutrino event acceptance. In the case of steady emission, one can assume a constant flux through all samples - then the number of expected signal events is proportional to the sample effective area and livetime. For the j^{th} sample, the fraction of signal is given by:

$$n_s^j = n_s \times \frac{\int_0^\infty dE\ A^j_{eff}(E, sin\delta)E^{-\gamma}}{\sum_i \int_0^\infty dE\ A^i_{eff}(E, sin\delta)E^{-\gamma}}$$

A_{eff} is the IceCube effective area, a quantity that yields the expected event count rate in IceCube when folded with the incoming flux at a certain declination angle and energy [Aartsen et al., 2017a]. For sources that display time-dependent behaviour, a flare in neutrinos in one subsample will contribute to the total signal of a time-integrated search. In general though, the ideal method to treat a time-dependent source is a time-dependent search.

3.1.2 Significance and p-value

To calculate the significance of an excess emission at a source position, one has to define a statistical test. By the Neyman-Pearson lemma, the most powerful test of two complementary hypotheses is a likelihood ratio test[2]. Here one defines a proxy of this likelihood ratio, called Test Statistics, as

$$\mathcal{TS} = 2\frac{log\mathcal{L}(n_s = \hat{n}_s, \gamma = \hat{\gamma})}{log\mathcal{L}(n_s = 0)}. \tag{3.1}$$

In the denominator, the null hypothesis states that there are no excess events over background. In the enumerator is the signal hypothesis with maximal n_s and the matching spectral index. In the case of a (single-) point source search with data-generated background, $\mathcal{TS}$ is monotonous in signal strength and positively definite, ergo a good measure of signal. Nonetheless, clustering of background events **by chance** can lead to high $\mathcal{TS}$ values, mimicking a point-like source when instead one sees a statistical fluctuation. To counteract this, one needs to quantify how many times signal 'appears' by chance. For this, one constructs a large number of background skymaps ('trials') and evaluates the Test Statistics at the source position for each one. The result should be close to $n_s = 0$ (no signal) in the majority of

[1] In practice, for computational purposes, we prefer to instead minimize the negative logarithm of $\mathcal{L}$

[2] The previous simple counting experiment would be a valid alternative, but lacks in power and $\mathcal{S} - \mathcal{B}$ distinction.

cases, with fewer and fewer outliers to higher values. The frequency of occurrence of these outliers is the probability for a false-positive excess.

An example at the TXS 0506+056 position is given in Fig. 3.1 which shows the distribution of $\mathcal{TS}$ values. For a given source, one can read out the probability to find a certain $\mathcal{TS}$ in a pure-background case. This can be obtained by integrating from the $\mathcal{TS}$ value to $+\infty$ in the plot, and comparing to the total integral (see Eq. 3.4). The fraction is called p-value of the distribution with respect to a certain $\mathcal{TS}$ value, and is usually translated into a significance level by the following relation:

$$\text{p-value} = \sqrt{2}erfc(\frac{\sigma}{2}) \tag{3.2}$$

$$erfc(z) \equiv \frac{2}{\sqrt{\pi}} \int_0^z e^{-\tau^2}\, \mathrm{d}\tau \tag{3.3}$$

with the Error function $erfc(z)$. Two significance levels are by convention important to note: a 3σ (p-value $= 2.7 \cdot 10^{-3}$) excess is called **evidence**, a 5σ (p-value $= 2.867 \cdot 10^{-7}$) excess is called **discovery**.

Clarification regarding significance

The p-values quoted in this work are the tail probability of the $\mathcal{TS}$ distribution (pdf) as shown in Fig. 3.1:

$$\text{p-value} = \frac{\int_{\mathcal{TS}}^{+\infty} pdf(\mathcal{TS}) d\mathcal{TS}}{\int_{-\infty}^{+\infty} pdf(\mathcal{TS}) d\mathcal{TS}} \tag{3.4}$$

In this hypotheses framework, the definition implies that all $\mathcal{TS}$ values in the distribution are possibly background fluctuations. The p-value gives the probability that a fitted signal originates from such a fluctuation. Small p-values and consequently high significances therefore indicate that the signal is unlikely of background origin. Conversely it is not a measure of how likely it is true signal, or a probability of correctness of the test hypothesis ($\mathcal{H}1$: existence of a point source at the examined position, in this case). The statement one can make after fitting a small p-value is the rejection of the background hypothesis.

3.1.3 Trial Generation

Estimating the neutrino background from a source position by calculation or simulation is nontrivial or computationally too intensive. Instead, data events are used to determine the background of most IceCube point source searches: one reassigns each event in a sample a uniformly random rightascension value. This procedure is called scrambling. For a single source position, one generates a new, random sky in neutrinos: any clustering of events at that position is purely coincidental. Hidden in this procedure is the assumption that the real sky contains little signal, which seems justifiable from previous analyses [Aartsen et al., 2017a]. No-signal is a conservative assumption: true signal is in the case of a signal-filled sky less significant in comparison. On each of these random skies, a fit is performed at the source position and a $\mathcal{TS}$ value is extracted. The $\mathcal{TS}$ distribution is shown in Fig. 3.1 and behaves as expected: most trials are signal-empty, some show positive fluctuations. The significance of a fit can now be expressed in terms of partials of this distribution.

In addition to pure background maps, scrambling can also be used to simulate a source on top of background by artificially adding simulated MC events [Aartsen et al., 2016, for details on MC]. For a

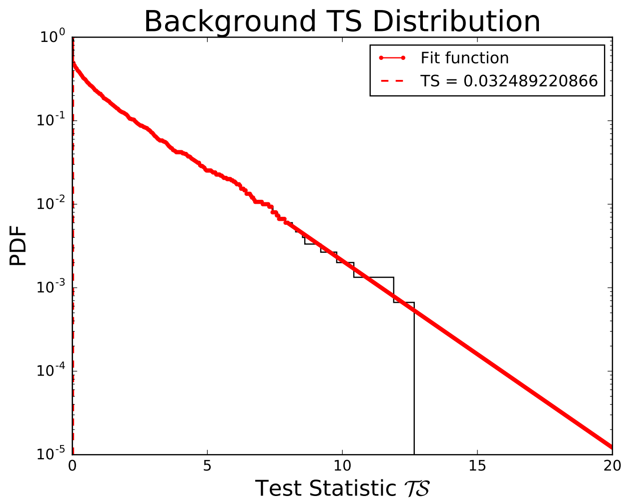

Figure 3.1: *Background trial test statistics distribution in black (counts over value histogram). The dashed red line is the median of the distribution, so most trial $\mathcal{TS}$ values are equal or close to zero (= no signal). To the right, there are outliers marking upwards fluctuations of clustering background events. If one sees an excess in the data, the relevant question is: how likely is it to have pure background fake this magnitude of signal. The solid red line shows the trial histogram up to a $\mathcal{TS}$ value of 8. For larger values, a fit (simple exponential) to the entire distribution is used, excluding a delta peak at 0. For large signals, the fit can replace generating trials on the order of 10^6 or more, saving a massive amount of computation time. The lack of statistics for high signal can be seen from the black line which is real trials. The fit approximates the tail distribution well.*

known source spectrum, one adds MC following this spectrum ('injection'). Events that get injected at the source (true direction = source direction) cluster around this source, but rarely directly on top of it due to their reconstruction. A sky realization of scrambled background + MC injected events ('injected trial') can be used to estimate three important quantities: sensitivity of the analysis to signal, the analysis discovery potential, and a best-fit result.

Simulated events are generated and propagated through the detector where they are subject to the same reconstruction as the data events. In consequence, they have a true and a reconstructed direction. Upon injection, their true direction is rotated to the source position. Their reconstructed direction points to a spot near the source. This accounts for IceCube reconstruction effects in the estimation of signal strength.

3.1.4 Sensitivity, Discovery Potential and Best Fit Result

The value of a flux is usually given as the flux normalization ϕ_0 at the pivot point 1 TeV for an E^{-2} spectrum. For a single powerlaw spectrum, one uses the relation for the flux F:

$$F(E, \gamma) = \phi_0 \left(\frac{E}{E_0} \right)^{-\gamma} \tag{3.5}$$

With this, the flux is well defined for all energies. Note that the flux is in this framework given as the differential $\partial N / \partial E$. Integrating over an energy range gives the absolute incoming particle count in that range.

The **sensitivity** of an analysis is widely defined as the 90% Upper Limit one would place in the case of no signal. For point source analyses with monotonous $\mathcal{TS}$ distributions, this is realized as following: one builds a $\mathcal{TS}$ distribution and then samples injected trials with an (n_s, γ) combination so that exactly 90% of the trials yield $\mathcal{TS}$ values larger than the median of the distribution. The median is usually close to zero (see Fig. 3.1) and the resulting flux can be quoted as the minimal flux IceCube is sensitive to. For the TXS 0506+056, the sensitivity is one single value, which is put in the context in Fig. 3.2 of the 7 years point source search sensitivity on the whole sky. For the TXS 0506+056, the value is $3.04 \cdot 10^{-13} TeV/cm^2 s$ or 5.22 fitted signal events, lower than for only 7 years of data.

Discovery Potential refers to the flux where one would claim evidence (3σ) or detection (5σ). In this work it is used, if not explicitly stated otherwise, as the 5σ threshold. Ideally, one wants to inject the exact flux where a fit of the trial gives the p- and $\mathcal{TS}$ value corresponding to 3σ (5σ). Due to statistical broadening, one instead has to search for the flux where the median of injected trials yields this threshold significance (50% of injected trials above $\mathcal{TS}$ value corresponding to 5σ significance). The discovery potential at the TXS 0506+056 is $0.978 \cdot 10^{-12} TeV/cm^2 s$ or 17.1 fitted signal events. The best fit flux is the flux (tuple of n_s, γ) one has to inject to find the median $\mathcal{TS}$ value obtained by fitting the real data.

Fluxes can be calculated as differentials, using only parts of the sample. Common differentials are infinitesimal/binned energy and declination angle. In both, one obtains ranges of the quantity where the analysis is most sensitive. For the sensitive energy range of this analysis, see Fig. 3.3.

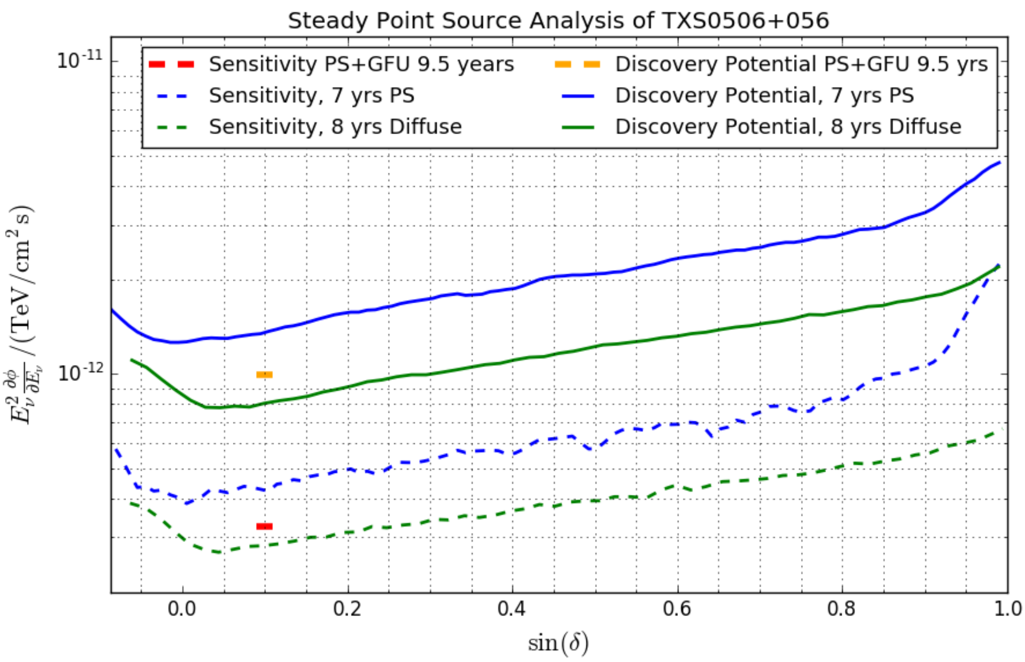

Figure 3.2: *Sensitivity (red) and Discovery Potential (orange) for the TXS 0506+056 position with the combined total 7yrsPS+GFU sample. For the entire Northern hemisphere, the 7 years Point Source sample sensitivity and discovery potential is shown in blue and for the 8 years Diffuse sample in green. Fluxes are given as the flux normalization to an E^{-2} power law over energy. Adding 2.5 years of GFU data to the Point Source sample improves the sensitivity, almost to the quality of the Diffuse sample. The Diffuse sample was considered as an option to perform the analysis on, since it's the most sensitive sample for point source searches in IceCube. It was disregarded because adding the GFU data is not as straightforward as for the PS sample due to differences in the event selection. The TXS 0506+056 source is in the area of the highest IceCube sensitivity around the horizon, making it a perfect target for a point source search. The Discovery Potential flux is higher than the sensitivity, more injected signal is needed for a discovery (50% of trials in the 2.867e-7 quantile of the $\mathcal{TS}$ distribution) than for the 90% UL in background case (90% of trials above median).*

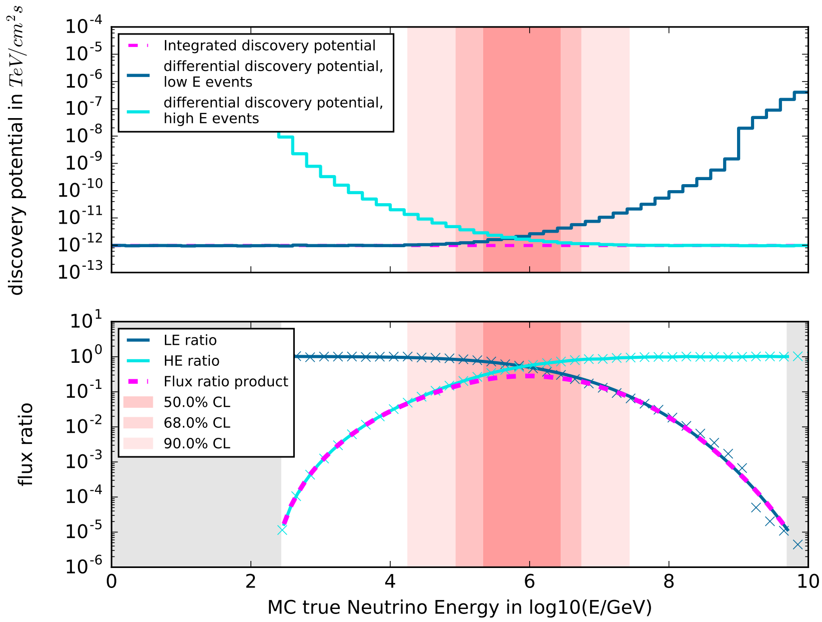

Figure 3.3: *Differential Discovery Potential for the TXS 0506+056 position with the combined $7yrsPS +$ GFU sample split in bins of one energy decade for an assumed spectral index of 2. The flux is calculated for each bin by using all events with energies higher (dark blue) or lower (cyan) than the bin mid. By normalizing this to the total sensitivity flux (which should always be smaller than the differential one) and taking the maximum of the two curves (lower-higher), one obtains the central energy range in which the analysis is sensitive. The 68% range for this analysis is [89.1 TeV, 5.3 PeV].*

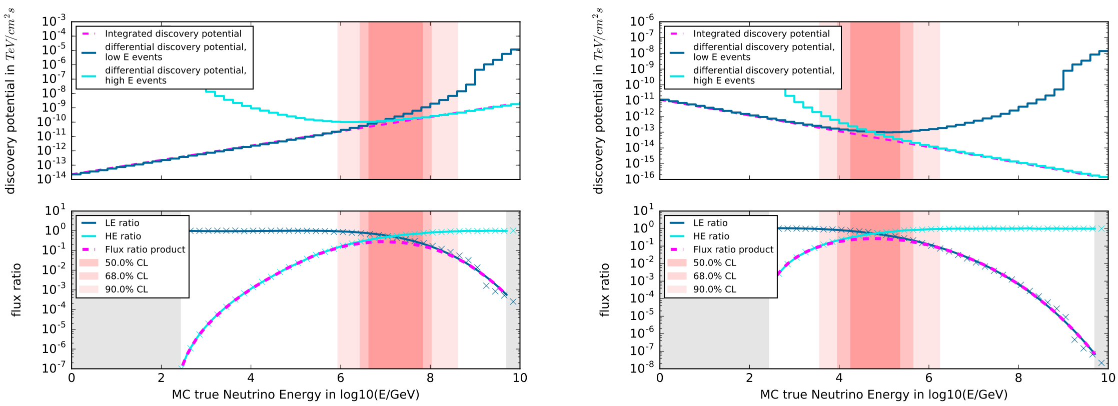

Figure 3.4: *Differential Discovery Potential for the TXS 0506+056 position for gamma = 1.5 (left) and gamma = 2.5 (right). For softer source spectra, the IceCube sensitivity would be shifted to lower energies. In this case one expects a large number of low-energetic neutrinos making up the signal. For harder source spectra, the probability to see PeV tracks would increase, making higher energies accessible.*

Data Blindness

In particle and astrophysics, there is a large number of testable hypotheses on data that has to be preprocessed under analyser-defined assumptions. An analyser needs to take care to avoid biases or false claims of correlation. Those could arise from the possibility to shape the result by means of changing the dataset or by constructing a hypothesis that matches the circumstances a posteriori. Analyses are constructed on blind data or a 'Burn Sample'[3]. For this analysis, testing and performance assessment, sensitivity and discovery potential calculations, are performed on data scrambles (experimental data with right ascension randomized, see Sec. 3.1.3). The actual analysis is performed after a review process verifying procedural and physical correctness as well as sufficient performance. This review is finished by setting the exact analysis plan, which can not be changed again as soon as real data entered the process.

3.1.5 Software

The analysis relies for central tasks on the software *skylab*[4] which has been developed for unbinned likelihood maximization for point-like neutrino source searches. Meanwhile it has been expanded to extended sources and cross-correlation multimessenger searches. Being under active development by IceCube, core parts of the software have been improved within the frame of this work, aiming to further improve performance and increase the area of possible applications. *skylab* is a high-performance toolset optimized for large data sets. Crucial analysis parts executed in this framework include the generation of randomized background maps, source simulation, generation of data/MC probability density functions, likelihood weighting of the data events, and fitting.

For the publication of IceCube data, events, and detector information connected to the TXS 0506+056 point source analysis, a software tool has been developed within this work[5]. It generates the necessary information in machine- and human-readable format. It can also perform the fits to reproduce the analysis presented here and shown in [The IceCube Collaboration, 2018] using these reduced data. It is based on *skylab*, but improvements to performance (and readability) has been made. It also contains fitting, configuring and loading routines that are not part of *skylab*, but can be used to analyse the released data. In contrast to *skylab*, it does not require MC simulations to generate the event pdfs, but uses the published detector properties and real event data instead.

Investigation of IceCube data and reconstruction has been conducted using official IceCube software, including IceTray for large-sample processing and steamshovel for visualization - event images can be found throughout the work. The event reconstruction designed in this work is also based on IceTray and makes use of standard IceCube reconstruction software packages.

[3] A part of the data that is used to verify the method, and does not enter the analysis execution.

[4] https://github.com/mhuber89/skylab/blob/stacking/skylab for the exact code, original by Stefan Coenders [Coenders, 2016]

[5] Access (restricted to IceCube members) under
http://code.icecube.wisc.edu/projects/icecube/browser/IceCube/sandbox/bkrammer/TXS_Paper

3.2 Unblinding

The procedure of performing an analysis on true IceCube data (as opposed to scrambled, randomized pseudodata) is called Unblinding. It requires an analysis concept that was proven to be procedurally correct and effective. The analysis is required to produce new scientific output. This can be achieved either by resulting in new knowledge or improving old analyses beyond a certain threshold (for example, 20% sensitivity improvement). The concept has to undergo review and collaboration approval and cannot be changed a posteriori.

The unblinding plan worked out for the TXS 0506+056 steady point source search with 9.5 years of muon track data (7 years point source sample + 2.5 years of GFU data) included:

a) Likelihood fit and p-value of the exact source position on the whole data sample

b) Likelihood fit and p-value excluding the EHE event IC170922A

c) Visualization of both results in a 4x4 deg^2 skymap section: p-value and fit parameters

Using the whole dataset for the analysis is an obvious, intuitive and straightforward path and well-suited for a pure follow-up analysis to figure out whether there is signal in the data. Running it enables the analyser to make a statement about how well they can reject the background hypothesis (compare subsection 3.1.2). While this is a useful first step, it is fundamentally flawed in the case of the TXS 0506+056.

The reason to perform this analysis at this exact spot in the sky is that IceCube has detected a certain event, IceCube-170922A, coincident with a flaring blazar there. This event is the 'trigger' for the analysis, but is also contained in the sample. This essentially biases the result statement. The solution for that dilemma is to simply remove IceCube-170922A from the experimental data (item b). Given the size of the sample, this does not necessitate recalculations of the simulated data or effective area and is therefore viable. It means though that one has to make a very arbitrary modification to the dataset to obtain an unbiased result. The cleanest way of presenting a result of this analysis as a whole seems to synoptically quote both values next to each other, explaining the benefits and flaws of both. This also allows to assess the impact of the EHE event by itself.

The visualization is intended to serve as a spacial crosscheck. If the TXS 0506+056 is a neutrino point source, excess signal should be confined to a small area around the source. If the result is dominated by a different nearby source, this should be visible by the maximum of the excess area not coinciding with the TXS 0506+056 position. One can also check for irregularities in the fit parameter maps to validate the fitter performance. The parameters are usually accurate in the case of signal, but for small fitted events, the fitted spectral index is not well-constrained and therefore not reliable. The map is generated by scanning a fine square grid equipartitioning the window, and fitting for signal at each intersection. As any point on the grid is close to the central source, I take the background estimate at the source position for the entire grid in very good approximation. The visualization is not the main result of the analysis, and there is formally no Unblinding of any grid point except for the center, the TXS 0506+056.

Chapter 4

Analysis Results

Here the results of the time-integrated neutrino point source search at the TXS 0506+056 position with 9.5 years of IceCube through-going muon track data are presented. I will show the analysis results on the dataset without the triggering EHE event IceCube-170922A, thus an unbiased sample, and afterwards the analysis on the full dataset. For comparison, I recalculated the same analysis on the 7-years point source sample previously published in [Aartsen et al., 2017a] and discuss the implications of the change in signal.

4.1 Results on the dataset excluding IceCube-170922A

The analysis on the 9.5 years removing IceCube-170922A finds a $\mathcal{TS}$ value of 5.86 at the position of the source, corresponding to a p-value of 0.012 and subsequently a significance of 2.3σ. This is a weak rejection of the background hypothesis, compatible with the no-source pure background hypothesis.

The fitted parameters are $n_s = 13.03$ and $\gamma = 2.12$. The spectral index is very close to the expectation of $\gamma \approx 2$ for a blazar and astrophysical neutrinos (Sec. 1.4.1). Compared to the CR spectrum [Gaisser et al., 2016], the fitted spectrum is hard. Subsequently, 13 signal events as found by the fitter is a large number of events, though not sufficient for a discovery (n_s =17.1). The values are put in context by figure 4.1 where the sky around the source position is shown. The source (at the center) is not a very rare excess. On the other hand it displays a narrow area of elevated significance as expected from a point source. So collecting more data might help reveal an actual excess here. This point will be discussed in Sec. 4.3.

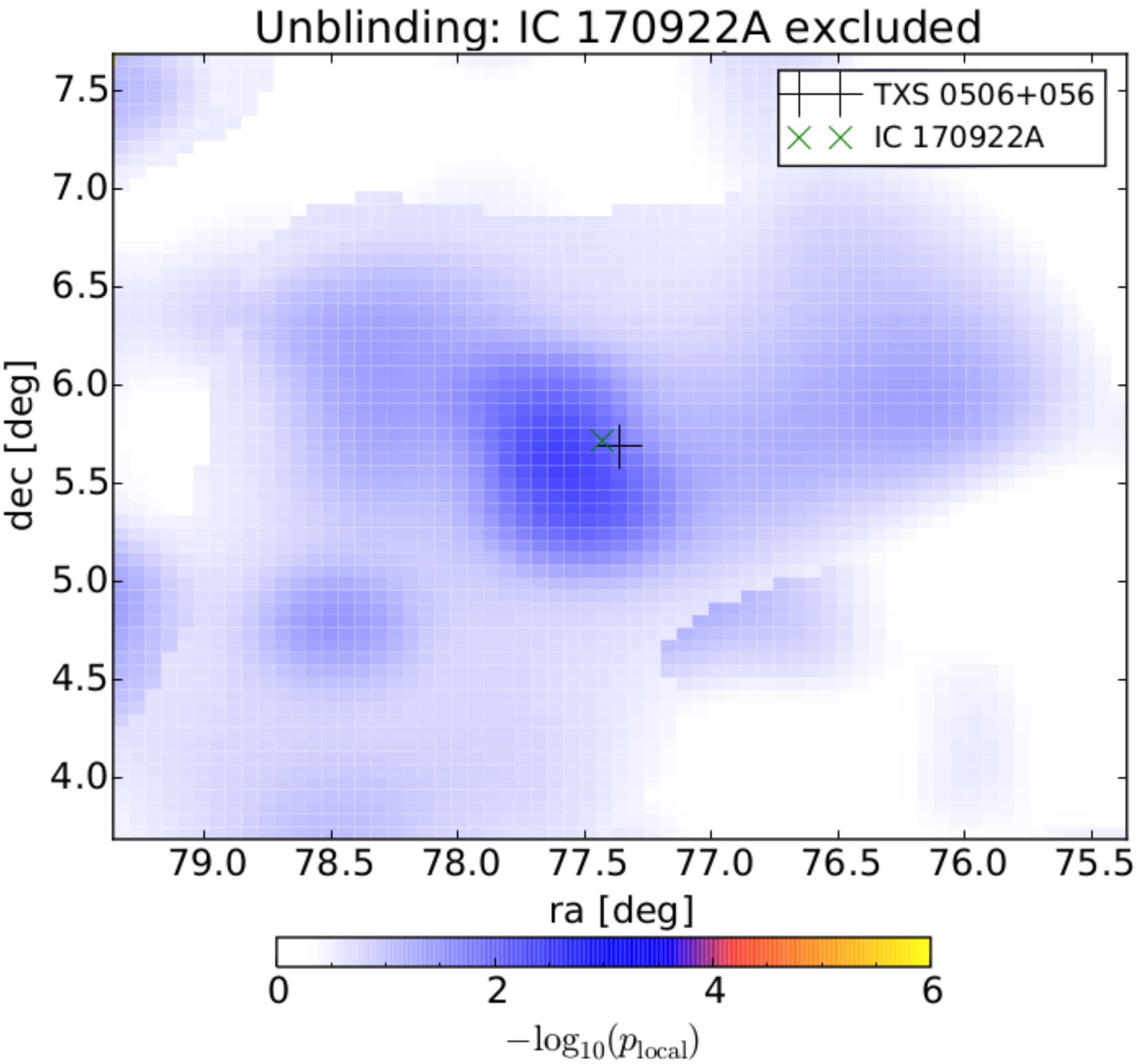

Figure 4.1: *This 4 by 4 deg^2 skymap section shows the p-value distibution around the TXS 0506+056 tested source location. It is pixelized in 64x64 cells equipartitioning the degree scale. This is not precise due to the curvature of the sky sphere, but a near-perfect approximation around the horizon. The EHE event best fit location (from https://gcn.gsfc.nasa.gov/gcn3/21916.gcn3) is marked for completeness. Looking at the center TXS 0506+056, one will immediately realize that spots with comparable signal strength are no rare occurrences on the whole sky. For this reason, the unbiased trigger-EHE-excluded analysis finds no sufficient excess from the source at this location.*

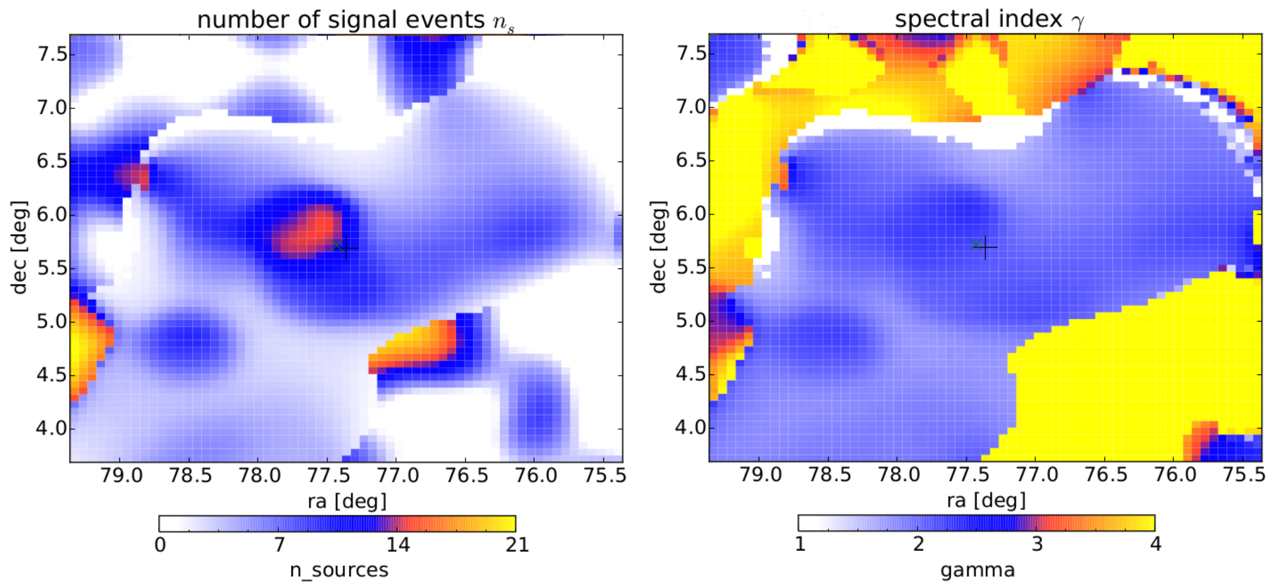

Figure 4.2: *Skymap sections for number of signal events n_s and spectral index γ on the full 9.5 years of data. For the n_s map, there are some off-source spots with large values. Those look interesting when one searches for high signal, but when comparing the respective γ values, they are comprised by many, but low-energetic events: the total likelihood to have signal in those places is not very high. For the γ, bright spots mark high spectral indices, thus soft spectra. Yellow regions are therefore background-dominated, blue-white ones are likely signal. The TXS 0506+056 source is stable throughout all fit parameters, the fitter performs optimal in the presence of signal. A discontinuous stripe feature in the p-value map to the lower right of the center can be explained by an area transition in the $n_s - \gamma$ maps.*

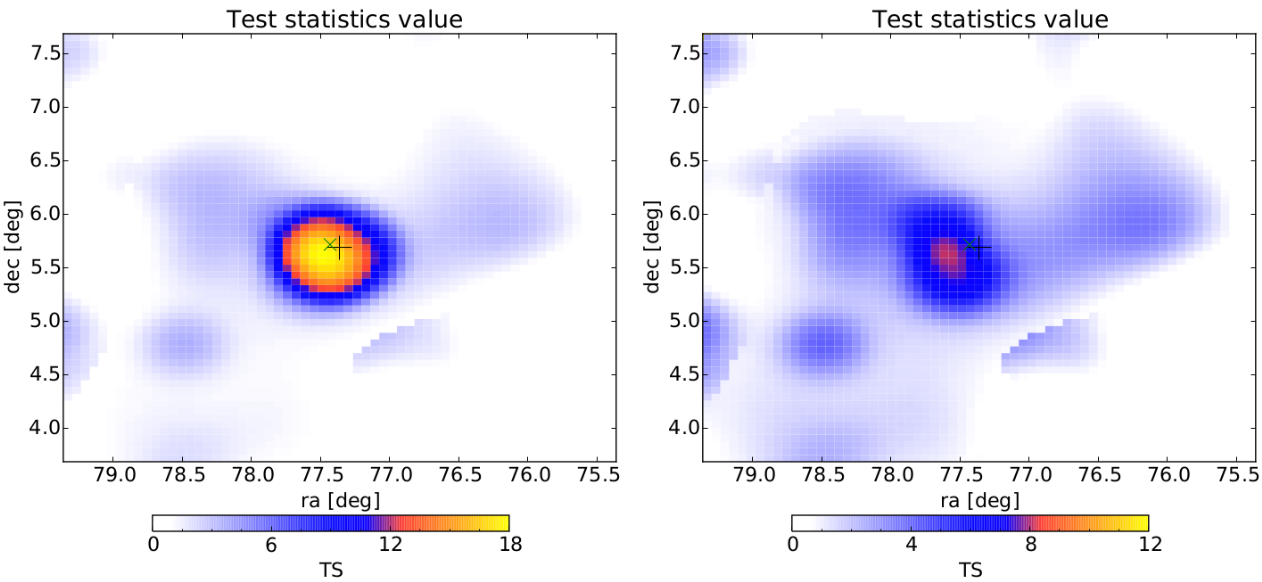

Figure 4.3: *Skymap sections for test statistics map including (left) and excluding (right) the EHE event IC170922A. The test statistics distribution is calculated once for the central source, as the premise of the analysis is to only test the central position. Any other point on the map is approximated using the central distribution.*

4.2 Results on Full Dataset

For the second analysis, the full dataset including IceCube-170922A is used. It finds a $\mathcal{TS}$ value of 18.15, resulting in a p-value of $2 \cdot 10^{-5}$ and a corresponding significance of 4.1 sigma. This is strong evidence against the background hypothesis at the source position.

In this case, one has to keep in mind that **the observation one makes here is biased**. In analogy: one sees a single event from this direction, and then asks the question whether neutrinos are coming from there. Including the initial event, one will in this case always 'count at least one'. Taking this back to the likelihood fitting method, the picture is not that simple. If there was no source, and one saw the single event by accident, one would not detect a very significant excess. The fitter would count one event over background expectation, returning a comparably low $\mathcal{TS}$ value. This is not the case here, and indeed one sees from the previous section that there is an excess of 13 signal events at this position. So one takes a look at the fit parameters yielding $\gamma = 2.00$ and signal events $n_s = 14.32$. By adding one event, n_s is not expected to rise by more than roughly one event. The additional margin is generated by the small change in spectrum. The signal event count is therefore within sensible bounds. Adding a high-energy event naturally makes the spectrum harder. For an unstable fit result, γ will likely vary a lot, most probably from a very soft to a harder spectrum. Observing only little change in γ implies that the event matches the overall emitted spectrum from the warm spot found in the previous section.

Overall, this is consistent with the results with IceCube-170922A excluded, providing additional validation for both. One can assume that the first result where a single event was artificially and arbitrarily removed from the sample is not impaired by this procedure. The second result - which is biased by including into the observation the reason why one observes - still fits in with the unbiased measurement. Both methods are therefore valid and consistent within their respective limitations. The central hotspot in the map in figure 4.4 clearly displays the expected point source shape. The hottest pixel is neither coincident exactly with the TXS 0506+056 nor the EHE event. The former is tolerable since the sample median angular error (0.5°) is larger than the distance between source and p-value peak. The spacial discrepancy with IceCube-170922A shows again that the additional significance boost by adding the event is a conglomerate of many events contributing to the LLH, and not only due to the observation trigger. This all in all gives a consistent picture, hinting at a potential neutrino source TXS 0505+056.

The second method including the trigger event has one more advantage: as the full dataset is used, one can calculate the best fit flux for the source. One does not rely on the spectral assumptions anymore, but can use the parameter set from the likelihood fit. Previous concerns about the fitter performing suboptimal in the case of no signal are void - signal is present here. Following the prescription in section 3.1.4, the flux of the source is $7.44 \cdot 10^{-13}\ TeV/cm^2 s$. This is shown in the context of the 7 years all-sky search in Fig. 4.5 [Aartsen et al., 2017a].

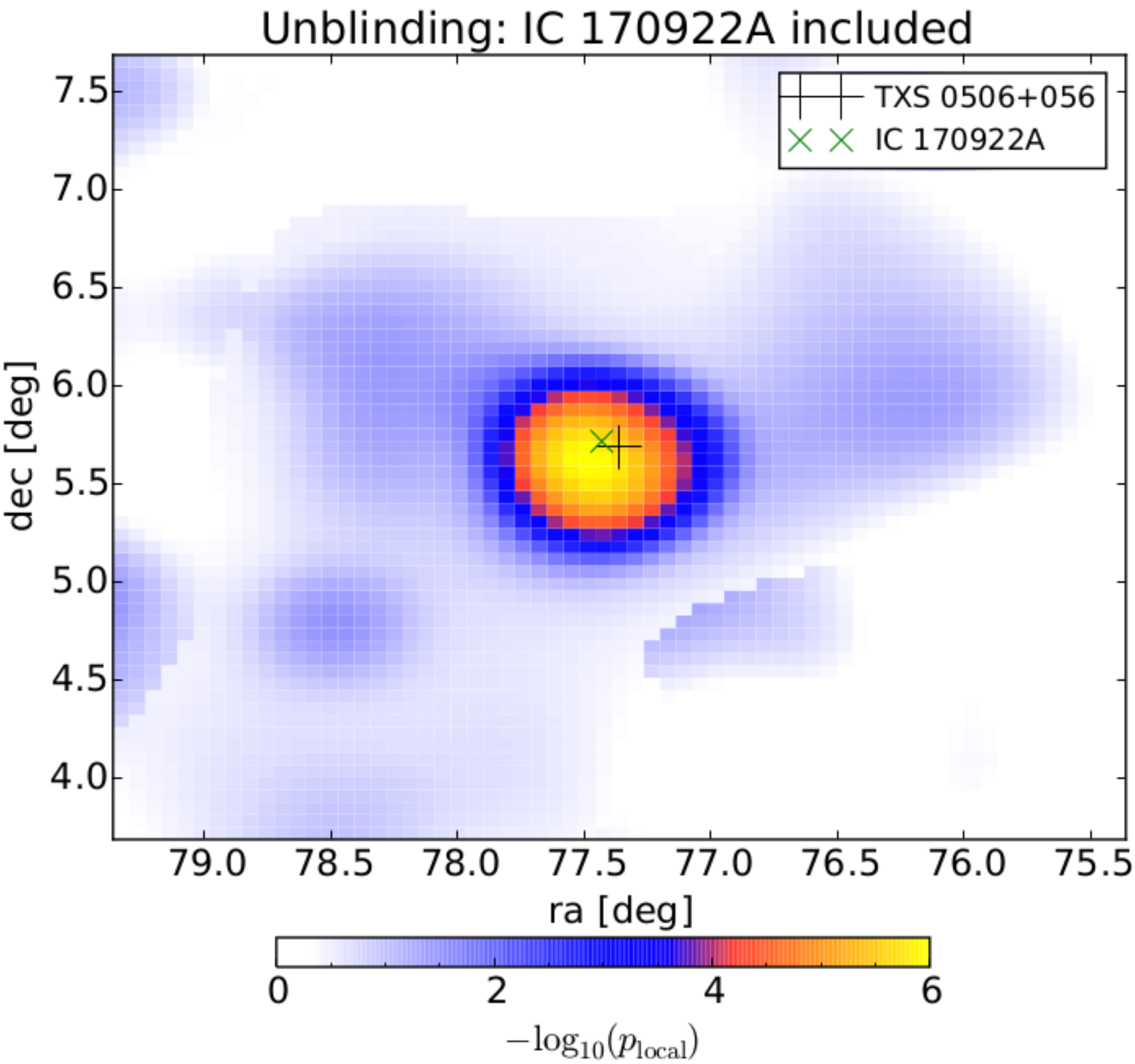

Figure 4.4: *This 4 by 4 deg*^{2} *skymap section shows the p-value distibution around the TXS 0506+056 tested source location. It is pixelized in 64x64 cells equipartitioning the degree scale. This is not precise due to the curvature of the sky sphere, but a near-perfect approximation around the horizon. The EHE event best fit location (https://gcn.gsfc.nasa.gov/gcn3/21916.gcn3) is marked for completeness - here it is also included in the sample. One sees a clear hot spot at the position of the prospective neutrino source that is spacially very much confined. Important to note here is that this only marks evidence for a neutrino point source from the direction of a blazar, which is different from claiming a discovering detection of a neutrino-emitting blazar point source. This constraint lies in the construction of the analysis. The hottest spot in the center is not exactly coinciding with the TXS 0506+056, but taking into account the median angular event uncertainty of tracks as* $0.5°$. *This is well within tolerance.*

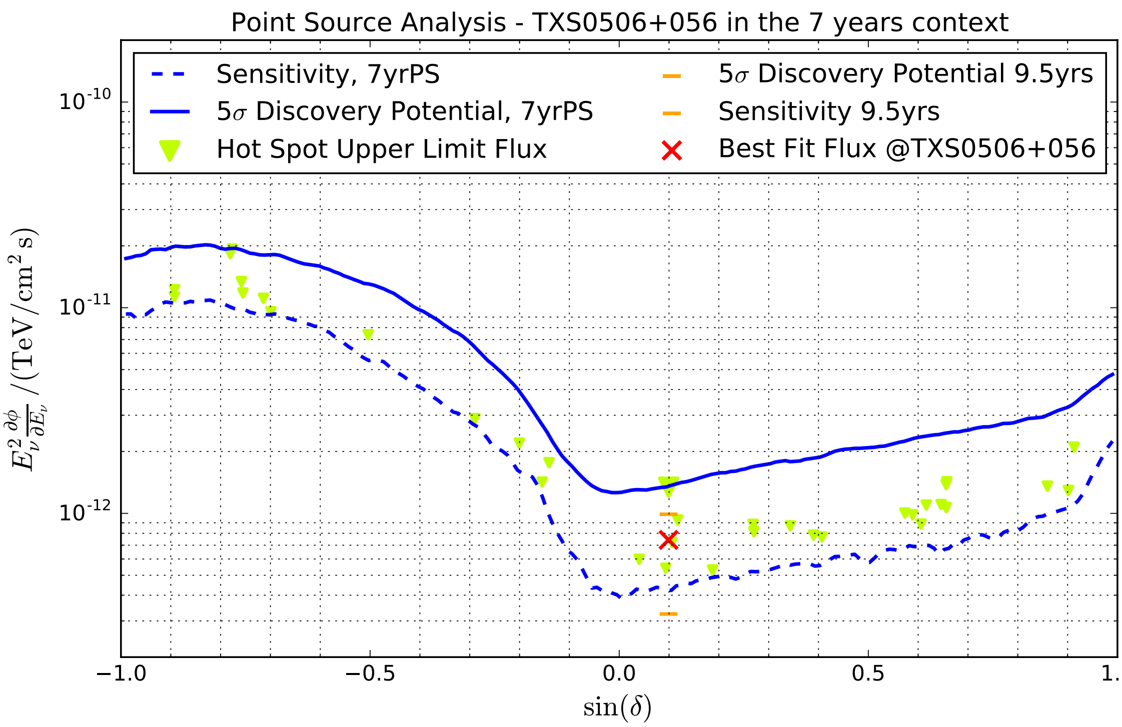

Figure 4.5: *Sensitivity and discovery potential of the 7 years all-sky search for point-like neutrino sources (blue) and the upper flux limits at the hot spots in the source list (lime triangles) [Aartsen et al., 2017a]. In orange is the sensitivity (lower) and discovery potential for the TXS 0506+056 with the current analysis using 9.5 years of data. The big triangle marks the upper flux limit for this analysis, the cross the best fit flux at the TXS 0506+056. Fluxes are given as the flux normalization to an* E^{-2} *power law over energy.*

4.3 Results from 7 years point source sample analysis recalculation

The 7 years point source unblinding is an all-sky and source list unblinding described in [Aartsen et al., 2017a] performed on IceCube muon tracks. The all-sky search divides the sky in equidistant grid points and performs a fit on each point to hotspots and significant event clusters on the whole sky. The source list contains objects that are possible neutrino sources, among them a few blazars (TXS 0506+056 not included). For a comparison of the results, one needs to rely on the closest grid point, which is less than 0.2° away. Against the muon tracks' median angular uncertainty of 0.5°, this is negligible in good approximation. The event selection starts with IC40 and ends with IC86-IV. From the current point, looking back at archival data has the purpose to assess how the excess at the tested position changes over time. Real signal is, in contrast to background fluctuations, expected to increase with more data/time. The exact comparison of values can be found in Tab. 4.1. A recalculation of the flux was necessary because the flux value for each all-sky grid point was not stored after the analysis.

The results from the 7 years Unblinding seem immediately consistent with the analysis on 9.5 years. The excess has grown, again indicating true signal from this direction. The fitting parameters are equivalently reassuring. Striking is only that adding 2.5 years of data only yielded 2 more signal events in the non-IceCube-170922A case. Looking at the event distributions, the GFU mainly adds low-energy events to the position fit. These are fitted to be background, so this is a real effect. It will be discussed in the following chapter why adding a large data-taking period to a fairly high signal only leads to such a small increase in significance.

4.4 Dataset and Systematics

Post-Unblinding, the neutrino track data was checked for particularities and systematic effects. The goal of this procedure was to quantify the signal further, and to investigate qualitatively physical correlations.

4.4.1 Systematics and Validation

To validate the results that have been presented above, a study on systematic effects was performed. The analysis itself does not account for potential sources of systematic errors, for example by fitting additional nuisance parameters. The hypothesis test and likelihood method are stable, but the sample selection can be affected by not-yet-fully-understood properties of the detector.

The South Pole Ice was characterized using calibration devices onboard of the DOMs [Aartsen et al., 2013b]. All DOMs carry LEDs that can emit short light pulses. The ice properties can be assessed by the scattering and absorption of photons traversing the ice from the 'flasher' to the neighbouring DOMs. The surrounding DOMs detect pulses from these 'flashes', their relative brightness and delay between photons. From this data, an Ice model can be constructed.

Despite these efforts, the South Pole Ice can still introduce systematic effects to the sample. For example, the flashers do not emit light isotropically. This limits the calibration effectiveness - at the current reconstruction precision of IceCube, the effects are large enough to play a role for the event selection. Calibration devices are currently being developed and tested to fulfil even higher demands to precision and versatility. Until their deployment, analysers need to carefully check their results.

Table 4.1: *Here, the analysis results, p-values, significances and test statistics values, are synoptically summarized. Both analyses performed are shown, and the recalculated results from the archival 7 years point source unblinding [Aartsen et al., 2017a] are included for comparison.*

	IC170922A excluded	full dataset	archival 7 years sample
p-value	0.012	2e-5	0.017
$\mathcal{TS}$	5.86	18.15	5.66
significance	2.3	4.1	2.1
γ	2.12	2.00	2.13
n_s	13.04	14.32	11.06

Especially critical in this regard is the directional reconstruction of the events. For a band around the horizon, events that enter the detector at a certain height are strongly affected by the "dust layer". The dust layer is a horizontal plane in IceCube at a depth of about 2 km where the scattering length of photons in the medium is short (on the order of 10 m). Only very bright events or events with light emission near the DOMs are detected as the scattering length is shorter than the inter-string spacing. IceCube reconstruction is taking this into account, but a perfect Ice Model has yet to be developed. Looking at each event separately for the highest-weighted events can be illuminating. Refer to Fig. 4.6 for an impression of the effects of the systematics.

4.4.2 Angular Uncertainty Crosschecks

The *SplineMPEparaboloid* fit for reconstruction usually performs well even in cases that are hard to judge by eye. Ambiguous events are assigned fairly large angular uncertainties. This decreases the overall contribution to the significance near the center, but widens the area where it contributes - the event gets washed out. As a measure of how much the spacial term contributes, refer to Fig. A.1 in the Appendix. There is a second check one can make to investigate whether one's per-event angular uncertainties are sensible: one can make changes to the events 'by hand' and compare the results. A pragmatic first change is to set all angular uncertainties of all events to a fixed value and look at the results. The effect is that events with good directional reconstruction decrease in LLH weight since they get broadened out the most. With increasing uncertainty value the analysis loses the capability to resolve structures that are smaller than the artificial uncertainty value (Resolution > Scale).
As flat values, integer numbers from 1 to 3 degrees were chosen. The result is not conclusive in that everything behaves as expected without any new insights - but also no appearing issues. A visualization can be found in the appendix as Fig. A.2.

A more effective approach is to blow up the per-event angular uncertainty by adding or multiplying to the existing errors. I favoured the method where one adds to the angular uncertainty. There one simulates the reconstruction being too optimistic by a small angle. The multiplication could suffer from a number of high-energy events with large error: those could enter into the likelihood calculation from far away, but due to their energy increase the LLH. The addition does not have this problem and is more robust. Addition is of course disproportionate by nature: well-reconstructed events double their uncertainty if tenths of degrees are added, while badly reconstructed events will change only little in that case. For checking whether the reconstruction influences the result, this is a conservative and sensible way. The chosen angular differences to add span roughly the same range as the actual per-event angular uncertainties, in steps of 0.1°.

The results are shown in figs. 4.7 and 4.8. With increasing uncertainty, the central excess expands

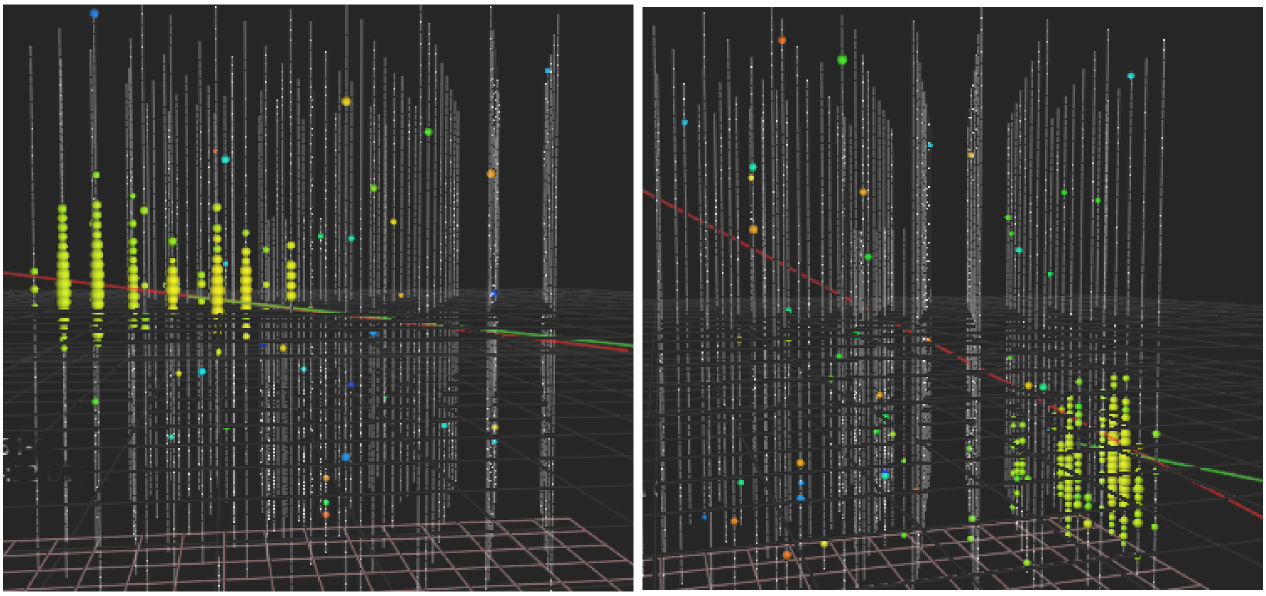

Figure 4.6: *Two events from the 7yrPS+GFU sample that have been investigated. White dots are the DOMs on their strings (white lines). The brown grid on the bottom is the bedrock, the black plane marks the dust layer. DOM hits are shown as coloured balls, the collected charge is visualized as the size of the balls, the color shows the arrival time on a scale from blue (early) to red (late). On the left is a track that is partially contained in the dust layer. A first-guess fit in red without Ice Modelling gives a reconstruction that is slightly off. The green high level algorithm recognizes the dust layer behaviour and gives a proper direction. On the right, there is an event from a partial detector configuration that is even more affected by the dust layer. Here the first-guess fit in red is not at all reliable, but the green high-level one finds a good track axis. It assigns a large angular uncertainty to the event. This accounts for the short track length and is desired behaviour.*

radially, but retains the majority of its significance. The excess is apparently robust against systematic effects.

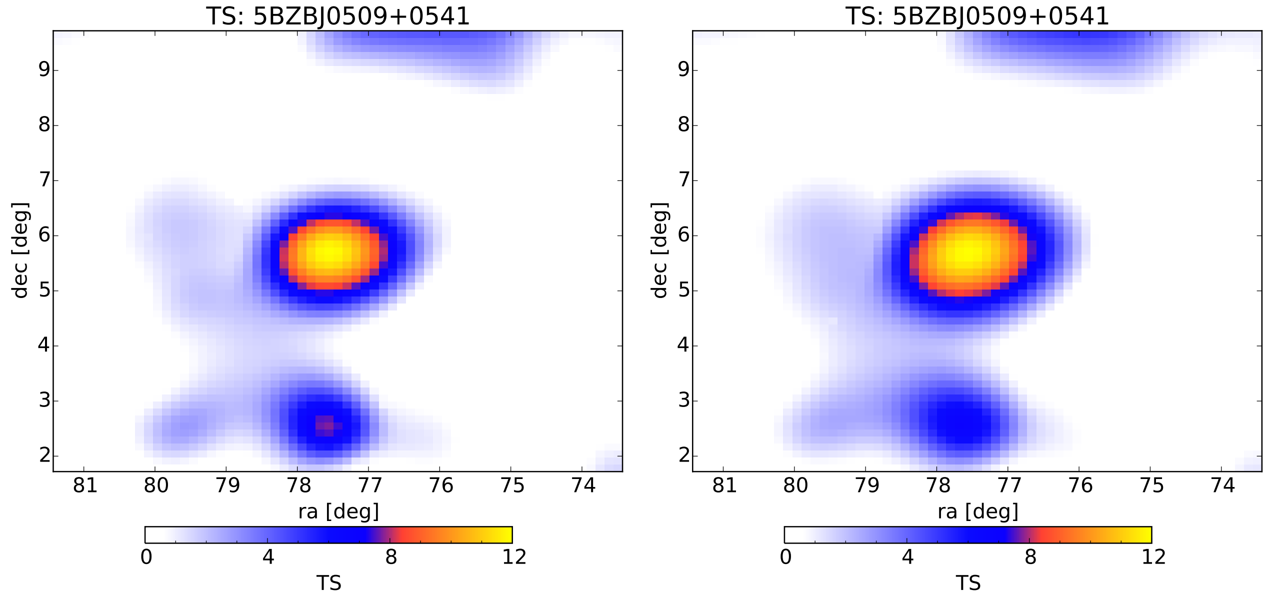

Figure 4.7: *Skymaps of LLH fits of and near the TXS 0506+056 with increased per-event angular uncertainty. Shown is the test statistics as a proxy for signal strength. The uncertainties increase by* $0.1°$ *per plot starting at* $\sigma_0 + 0.3°$. *Comparing Fig. 4.4 and the first map with increased angular uncertainty, there is little difference. The TXS 0506+056 excess expands as the angular resolution* ***of the analysis*** *worsens. There is no large loss in significance. Note that the TS distribution in Fig. 3.1 is not valid anymore for these maps.*

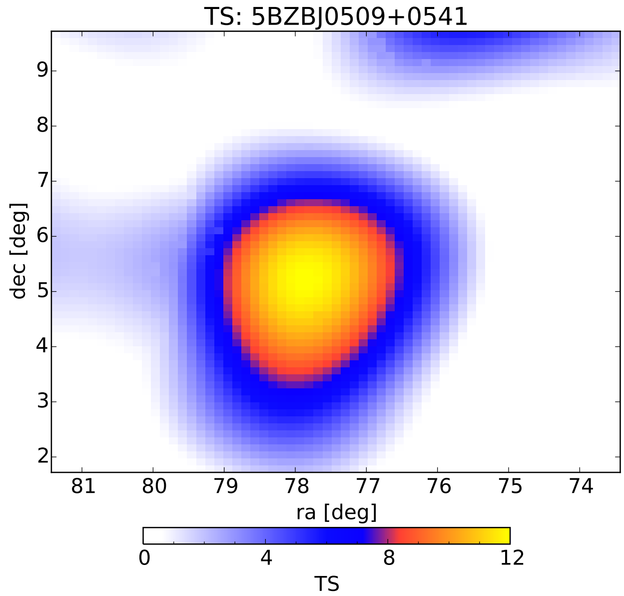

Figure 4.8: *Skymap of LLH fits of and near the TXS 0506+056 with increased per-event angular uncertainty. For this* $\mathcal{TS}$ *map, the angular uncertainty of each event has been increased by* $1°$. *One can see the same effect as in Fig. A.2 in the appendix: if the reconstruction is worse than* α, *then one can't resolve structures that are* α - 2α *or less apart. Interesting here is that the TXS 0506+056 remains a strong source.*

4.4.3 Systematics: Seeding and Bootstrapping Crosschecks

A different method to test for systematic errors on the result is changing directly the reconstruction of the events contributing to the significance of the source position. This can be achieved with different goals in mind and consequentially different setting choices. One can change:

a) The Ice Model

b) The reconstruction seed

c) The reconstruction method

a) IceCube has a set of models implemented that describe ice systematics with increasing precision. This includes to the dust layer, anisotropies in the ice, hole ice etc. Hole ice is the fact that the drill holes were filled with water and refroze under less pressure than the original ice, leaving long upwards cylinders of low-purity ice where the strings were inserted.
b) Reseeding the reconstruction means that the high-level uncertainty algorithm starts with a different set of initial parameters to check if it finds a different minimum.
c) For reconstruction, IceCube uses a chain of successive event fits described in 2.3.1. The 'end of the chain' is in this case called *SplineMPEmax Paraboloid* fit. It implements a multiphotoelectron likelihood at highest precision, Ice Models, and a parabola approximation for the uncertainty likelihood space. If this fit starts with a bad set of parameters, it could in rare cases be unable to find a good minimum. Then it returns a suboptimal reconstruction.

The complexity of the methods increases from (a) to (c), but the latter ones are preferable for a simple reason: to achieve an effect on the likelihood fit with a change in the Ice Models, one would have to reprocess the entire sample - almost 10 years of data. This is possible, but computationally and time-wise expensive.

Changes to the reconstruction can be applied to a small set of events. In principle it would be useful on the whole sample, but resources are limited. (c) is already quite effective to only apply this to the events contributing the most to the excess that needs to be examined. They make up the majority of the significance. If they are affected strongly by a change in reconstruction, the result is affected strongly. For the TXS 0506+056, those high-weight events are listed in the table A.1 in the appendix. A view of all events in the area is provided in figure 4.10.

For one of the events shown in Fig. 4.9, it is immediately obvious when this changing procedure can be of use. An *MPE* fit for this event performs badly. This algorithm is the most sophisticated of the basic ('first guess') fits and seeds higher-level reconstructions. Its failure doesn't seem to have a large effect on the final reconstruction. Caution should be exercised though: an angular distance of 1 degree is hard to spot in the event view, but an enormous difference for a source at redshift 0.3. The idea is now to replace intermediate-level algorithms and for example seed the final fit directly with the first guess. If this doesn't change the result, the reconstruction is good on all levels[1]. For a decent reconstruction of most of the events, one expects minor changes to the map and LLH fit result.

Method (c), the replacement of the final fit in the processing of the sample, has been carried out on the highest weighted events in table A.1. One option is to exchange the final directional fit by the

[1] Or globally wrong.

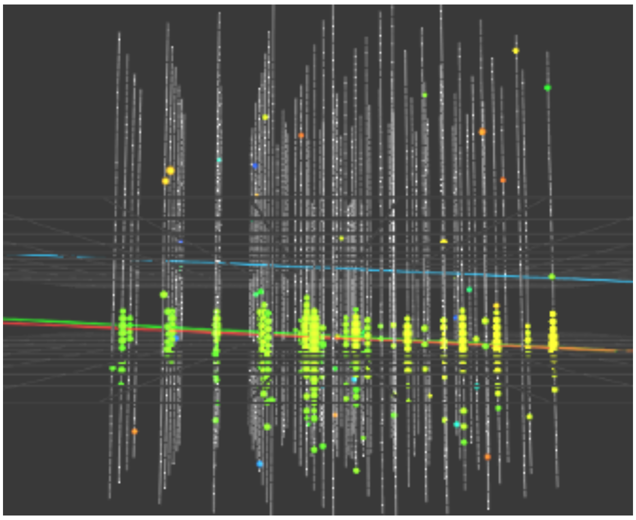

Figure 4.9: *View of a GFU event in the map. The event is completely enclosed inside the dust layer. Its energy information is possibly not reliable, and its directional reconstruction should be examined closely. The reconstructed directions are shown for three fits: the first-guess algorithm LineFit (red) and the final SplineMPEmax Paraboloid (green) agree well. This is due to the fact that the event is horizontal in the dust layer, with apparently minimal changes in ice properties and DOM acceptance. Fitting a line with the minimal distance to all charge-weighted hit DOMs works well. The blue line is an MPE fit [E. Andres, 2000] and performs badly in an attempt to account for ice systematics with a minimum of the necessary configuration.*

first guess *LineFit*. Another option is to use, instead of the paraboloid fit, a standard technique called 'bootstrapping': the brightest hit DOMs are removed and the remainder fitted in the standard way to see if this has an effect on the track. For a straight muon track, the effect should be negligible given a good reconstruction. Bootstrapping is automatically carried out on events with bad reconstruction in the sample as a fall-back fit. Since the GFU sample is reprocessed to be used for a point source search, it is in most cases not being used after a better fit has been administered, but the fit result exists in the file and can be used for crosschecking.

The result for both methods was a small decrease in significance of the TXS 0506+056 position. The most direct influence was for the *LineFit* where events like the one shown in Fig. 4.6 were so far off that they didn't contribute anymore. This is expected, if tracks are not perfectly straight and symmetric, *LineFit* will be inaccurate. The overall result was robust. All of this provides confirmation that the event reconstruction works well within its limitations.

4.4.4 A Note on IceCube Pointing Accuracy

The previous summary of techniques to investigate possible systematic errors with the IceCube muon track pointing is good indication that the reconstruction is trustworthy. Yet the best argument for valid IceCube pointing comes from the detection of the moon shadow [Aartsen et al., 2014]. The general idea is that the position of the moon is very well known. The moon, as a compact massive object, blocks out incoming cosmic rays that would otherwise hit the atmosphere and produce neutrinos. Not detecting neutrinos from the position of the moon must be as precise as detecting neutrinos from a point-like source. An observatory can therefore validate its pointing by analysing the agreement of the visible moon position with its shadow in neutrinos. Cosmic rays with energies high enough to

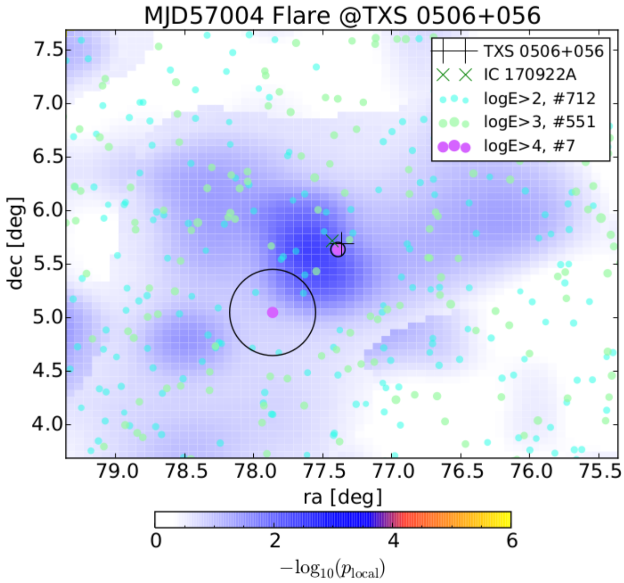

Figure 4.10: *Point Source Likelihood landscape around the TXS 0506+056 (IceCube-170922A excluded from the analysis) overlayed with the events from the neutrino sample. Colours divide the events into bins of their energy proxies. The highest-energetic events have their angular uncertainties displayed as black circles. One can see the events making up the TXS excess while having a direct comparison with background regions. The EHE event is marked as a tilted cross and also shows up as a purple high energy event. Both representations don't match exactly: the more precise and computationally intensive resimulation is used for the cross, while the purple circle is the product of the standard reconstruction used on every event in the sample.*

produce neutrinos in the sensitive IceCube energy range are abundant. The moon shadow analysis can therefore make use of high statistics, which is important when studying a systematic effect precisely. On two partial detector configurations (IC40, IC59), the moon shadow could already be resolved down to a precision of 0.2°.

This is not equivalent to the median angular resolution of the sample, which is quoted in this work as a measure of pointing. For the analyses presented in [Aartsen et al., 2014], this quantity is around 0.7° for the binned and around 1° for the unbinned approach. This shows that while single events may be reconstructed without very precise knowledge of their direction to tenths of a degree, a likelihood fit of many of these events can still achieve accurate pointing. This allows IceCube to be confident in the muon track reconstruction and the analyses based on track samples.

4.4.5 Re-Reconstruction with IceHive

Since the completion of the 7 years point source sample three years ago, new and better reconstruction tools and methods have become available. In the frame of this work, a prototype event reconstruction has been developed and benchmarked on the highest-LLH-weighted events from the 7yrsPS at the TXS 0506+056 position. The events and parameters are listed in Tab. 4.2. The reconstruction can be found in
http://code.icecube.wisc.edu/svn/sandbox/bkrammer/MuPostHive
Improvements with respect to the 7yrsPS L3 processing are reconstruction settings, high-quality paraboloid fitting and the novel use of IceHive pulse cleaning.

Table 4.2: *Event list of the re-reconstructed 10 events from the 7 years point source sample with the highest likelihood contribution to the steady analysis. Right ascension and declination give the event direction, paraboloid denotes the corresponding radial uncertainty, bootstrap is a fallback uncertainty in the case the paraboloid fails. This has not been the case for any of the events in the table, bootstrap is therefore provided for comparison only. Cursive indicates that those events were removed by the diffuse cascade cut.*

Run	Event	ra [deg]	dec [deg]	paraboloid uncertainty [deg]	bootstrap [deg]
126676	8726561	77.56	6.30	0.313	0.238
125414	63641159	77.39	5.43	0.112	0.175
126059	52497651	75.46	4.25	0.360	0.519
125762	*40914587*	74.90	-22.98	2.118	13.758
125583	502182	76.20	6.15	0.273	0.214
128999	44973537	77.53	5.43	0.279	0.378
125748	5363166	77.31	5.50	0.229	0.727
125659	*56262988*	70.32	27.69	1.806	4.039
126130	55370999	77.70	5.90	0.109	0.104
120173	72989335	76.77	5.33	0.355	0.408
127357	17650073	77.99	4.91	0.242	0.721

The reconstruction includes a set of cuts necessary to reduce a L2 dataset for processing by removing events according to Sec. 2.3.1. It then applies the IceHive event splitter which splits coincident events that affect each other and removes noise hits. This effectively cleans the pulsemap and ensures that good track events are not distorted. In rare cases of temporally coincident tracks, IceHive enables the reconstruction to properly treat both events. It does so by segmenting the entire detector into hexagonal substructures and identifying optical module responses as clusters or noise respectively.

After applying IceHive, the cuts need to be redone to check whether the events still fulfil the criteria. Events that were wrongly classified because a noise cluster of pulses faked a good track will be thrown away in this step. Noise that clusters by chance is marked by IceHive and needs to be classified here. This is a new approach - while IceHive has been applied in reconstructions before, the necessary refitting has been omitted until now.

Following the IceHive cleaning, new cuts can be applied to suit the reconstruction goal. In this work, no additional cuts are made since the benchmarked sample already underwent and passed the 7yrsPS cuts, but a template model to implement new cuts is provided. As an additional crosscheck, the cascade cut from the Diffuse Event Selection has been applied, finding that two events do not have a sufficient track length. One of them is shown in Fig. 4.6 on the left - it is visible by eye that it is not a good track. Running the prototype reconstruction effectively removes it from the TXS position as well.

The remaining high-level directional reconstruction and angular uncertainty estimation follows closely state-of-the-art reconstructions. The central algorithm is the *SplineMPE* muon track reconstruction that includes information about South Pole Ice properties. Interpolation tables (splines, hence the name) for absorption and scattering length at all points in the detector are utilized to predict the light yield of an event at each optical module. This improves basic algorithms like *SPEfit*, but can not yet deal properly with asymmetric Ice Models[2] or stochastic energy losses of muons. For the light yield

[2] Those are all Ice Models more recent than SPIce-Mie-notilt, e.g. Lea and SPIce-3.

prediction, and energy estimate of the event is necessary.

Here, the I3TruncatedEnergy IceCube module is used to provide an energy proxy. The energy estimate is based on the fact that above 1 TeV, the energy loss of a muon is proportional to its energy. Large stochastic losses skew this proportionality, so one removes the largest 'bursts' and averages the remaining losses. This also takes the Ice properties into account via photospline interpolation tables.

The *SplineMPE* algorithm does not provide an estimate of the event uncertainty, so these have to be obtained separately. The method already discussed above (Sec. 2.3.1) is the *SplineMPEparaboloid* which fits the log likelihood space with a parabola (equalling a 2D Gaussian in linear space). As a fallback method, the bootstrap uncertainty estimate is also employed. Both are run on the IceHive cleaned pulsemap to achieve an improvement in reconstruction. The 10 events are drawn from different samples and in the energy region where paraboloid pull affects the uncertainties the least, so the pull correction towards slightly larger uncertainties is omitted here.

A comparison to the 7yrsPS reconstruction for these 10 events is provided in the following figures. The impact on the steady point source analysis is within uncertainty bounds of the analysis ($\mathcal{TS} = 18.4$). Since only events with high LLH weight were eligible for this 10-event-testsample, therefore TXS-close events, the expected deviation points away from the TXS. Other events that are in the analysis further away would in some cases move closer to the TXS, increasing the TXS. Even with this selection that is not perfectly representative, there is no visible reduction of signal.

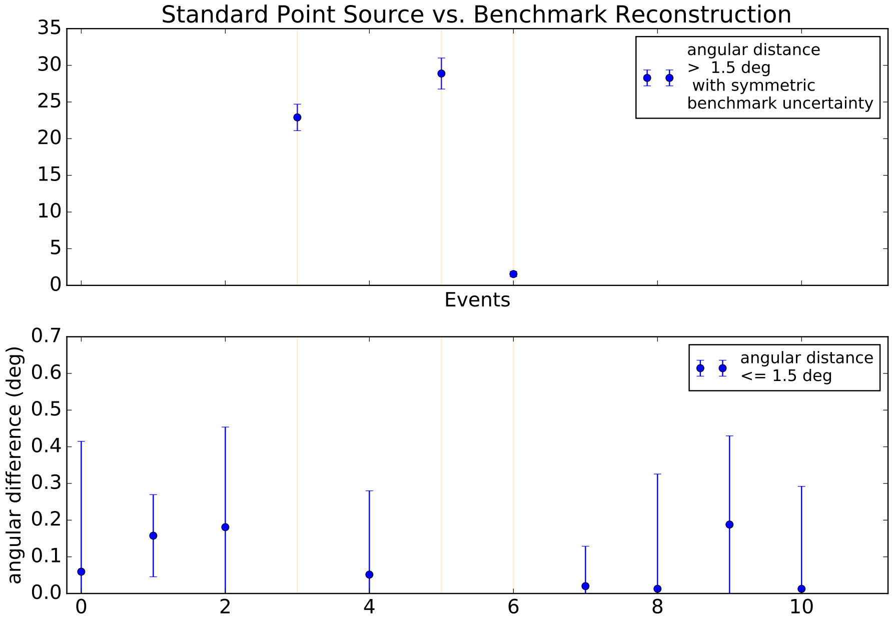

Figure 4.11: *Reconstructed direction difference of the benchmark reconstruction (blue), the 7 years point source reconstruction (red). Events 3 and 5 are removed by the cascade cut (but shown here) due to insufficient track length. Event 6 is affected by the dust layer, but still a good track event. The difference in direction is for most events well within the uncertainty bounds.*

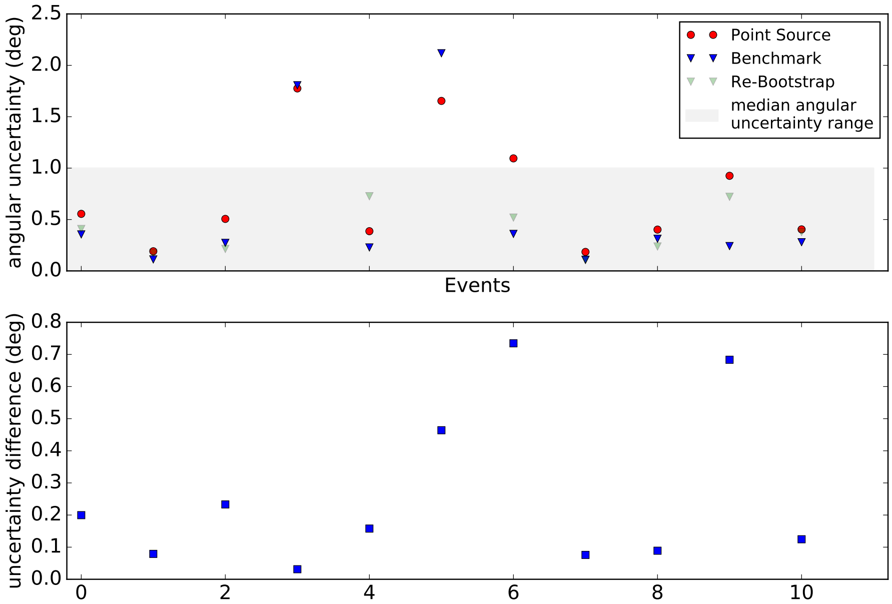

Figure 4.12: *Angular uncertainties of the benchmark reconstruction (blue), the 7 years point source reconstruction (red) and the fallback bootstrap of the benchmark (green). In the lower plot, the difference between the benchmark and pointsource paraboloid uncertainties are shown.*

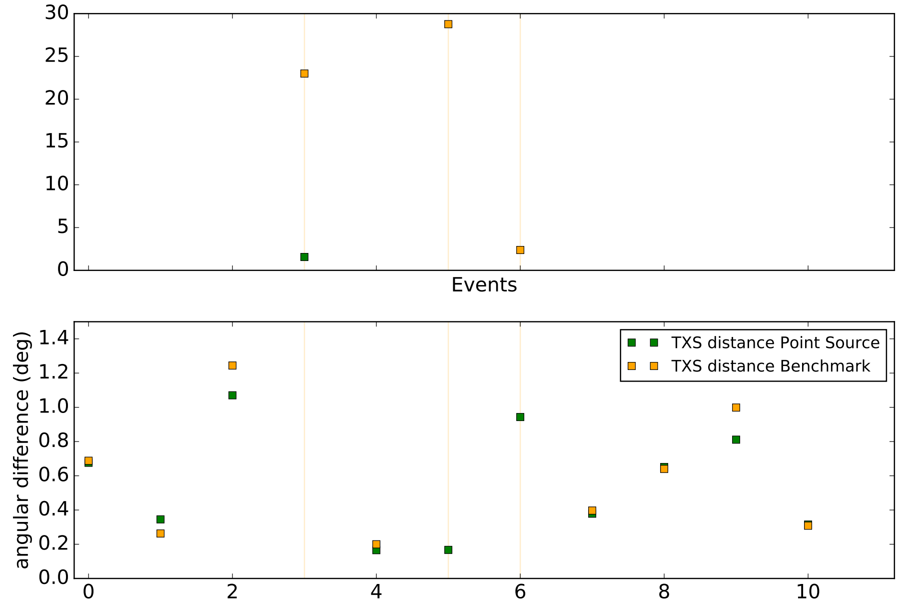

Figure 4.13: *Benchmark reconstruction (blue) and 7 years point source reconstruction (red) event distances to TXS. No large deviations in the analysis are expected, as the difference in per-event-distance is small for all good tracks.*

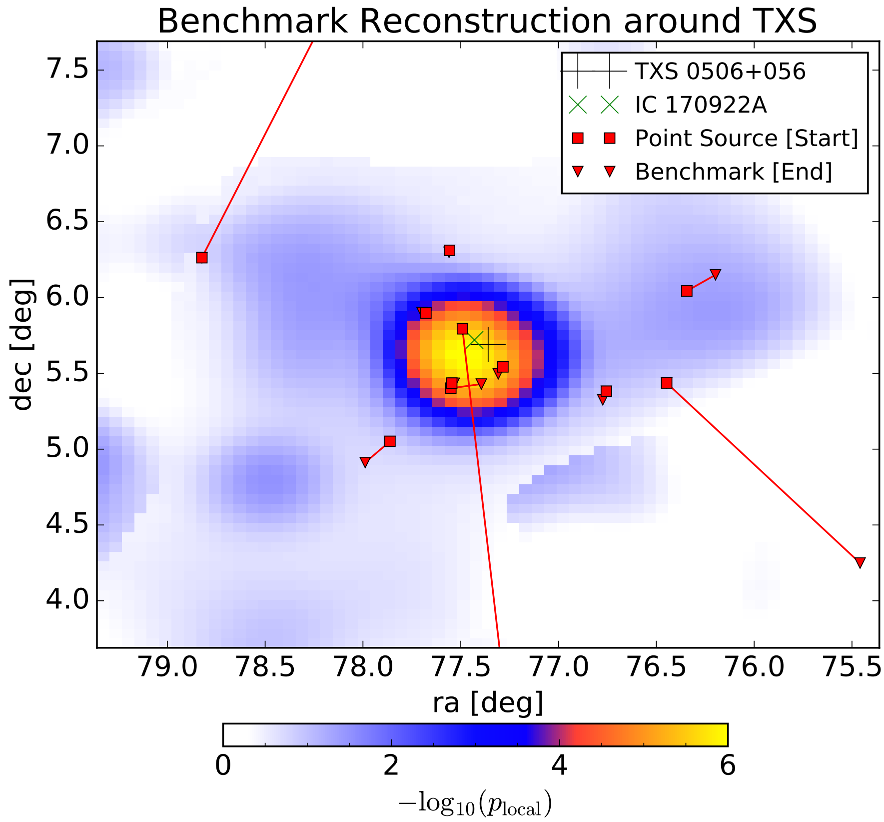

Figure 4.14: *Skymap of the 10 re-reconstructed Events over the steady analysis skymap including the EHE event. Red lines indicate the distance between the position of the events in the 7yrsPS sample and the new Benchmark reconstruction. Two events (nrs. 3 and 5 in the plots above) have a vastly different directional reconstruction - they are possibly misreconstructed cascades. The overall impact on the analysis is small. In total, the events seem to move away from TXS with the new reconstruction, but that is likely a selection effect: they were chosen by their $\mathcal{L}$-weight which includes spacial proximity. Shifting them by little within their uncertainties is more probable to move them away from the TXS. The default reconstruction proves stable against possible noise misclassification.*

4.4.6 Resimulation of Events

The most effective reconstruction available to IceCube is the DirectFit resimulation of events [Chirkin, 2014]. This method simulates a neutrino event, interaction vertex and predicts the resulting secondary particles and photon cascades. Their subsequent interactions are modelled down to photon propagation in the South Pole Ice from the particles and vertices to the detector optical modules. Then it calculates the likelihood of the measured pulses originating from this event, and redoes the simulation with more probable parameters until a good fit is reached. While *SplineMPE* reconstructions are limited to the usage of symmetric Ice models, DirectFit can account for Hole Ice, tilted Ice layers, bright DOMs (modules with saturated PMTs, e.g. near vertices) etc. The trade-off is its immense use of computation resources.[3] Performing the fit on the 10 highest-LLH-weighted 7yrsPS events has been attempted to validate the TXS 0506+056 steady point source analysis.

The results were good for a few events, but overall there manifested some problems: While IceCube-170922A as a high-energetic event with many hit DOMs could be reconstructed very well, reproducing existing fits accurately, the picture is different for standard sample muon tracks. Fewer total charge and shorter track length in the detector allow different simulated events to result in approximately correct pulses (equal to the measured event). For the final best fit, this is mostly not an issue. The directional uncertainty calculation though suffers from this. The event uncertainty regions are determined by finding the inner contour that contains a fraction CL of all simulated events, with the confidence level CL and the final statement being 'CL of all resimulated events lie within this contour.' Badly restrained behaviour before the best fit leads to large uncertainty regions - test events are scattered over a large area. This can be counteracted by setting lower tolerances, but the resulting increase in computation cost was deemed unfeasible in the set time frame.

[3] Even though it relies on GPUs for cascade simulation, a single events takes days to weeks.

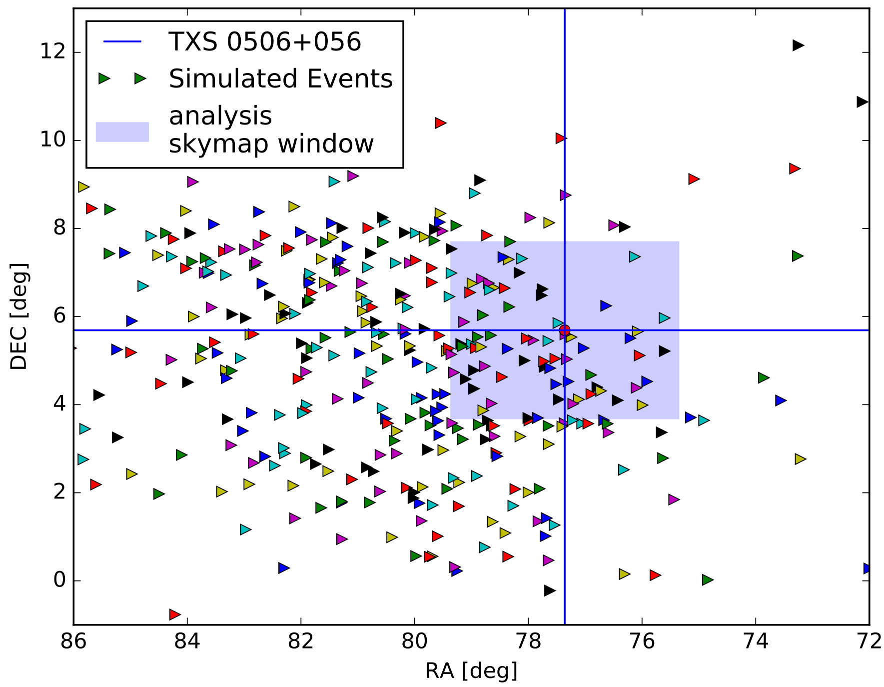

Figure 4.15: *Resimulated event distribution of an event from the 2014 flare. The reconstruction at this precision level is not sufficient, the spread region is too large to derive a useful uncertainty. Still, the event is located around the TXS 0506+056, however the uncertainty region is not centred on it.*

4.5 Second Unblinding with 10 years of data

The analysis presented here has subsequently been updated with more data: an additional half a year of data is available at the time of writing this. The new GFU data has been processed up to 25th of March 2018. It is added to the previous 7 years of point source sample + 2.5 years of GFU sample, covering almost the entire time before the new analysis execution. The analysis process is exactly the same as the first unblinding described above. The procedure comprises a first attempt to establish routine or fast-track unblinding updates in IceCube point source searches.

The TXS 0506+056 source flared a second time in high-energy gamma-rays in the added time-window [Ojha and Valverd, 2018]. The flare is reported to have been observed for one day, only emitting a few high-energy events before the alert. According to the Astronomer's Telegram, during the flare a spectral hardening of the source emission was visible.

The resulting skymap section can be found in Fig. 4.16. There has been no significant change to the fit results compared to the previous ones: the final $\mathcal{TS}$ value is 17.30, n_s is fitted to 13.62, γ is determined to 1.99. The flux decreases from $7.44 \cdot 10^{-13}$ TeV/cm^2s to $7.32 \cdot 10^{-13}$ TeV/cm^2s. All changes can be explained by fluctuations. Compared to the expectation of a decrease in significance and softer spectrum, this shows marginally more signal than the 9.5 years sample. Adding more background than signal lowers the flux (energy of events per time). Not observing a signal decrease in the steady analysis hints at the presence of neutrinos from the source in the added time window, though the result is quantitatively inconclusive. The TXS 0506+056 does not appear to be a steady source, but rather emit signal in a time-dependent fashion in 'bursts' or flares. Observ-

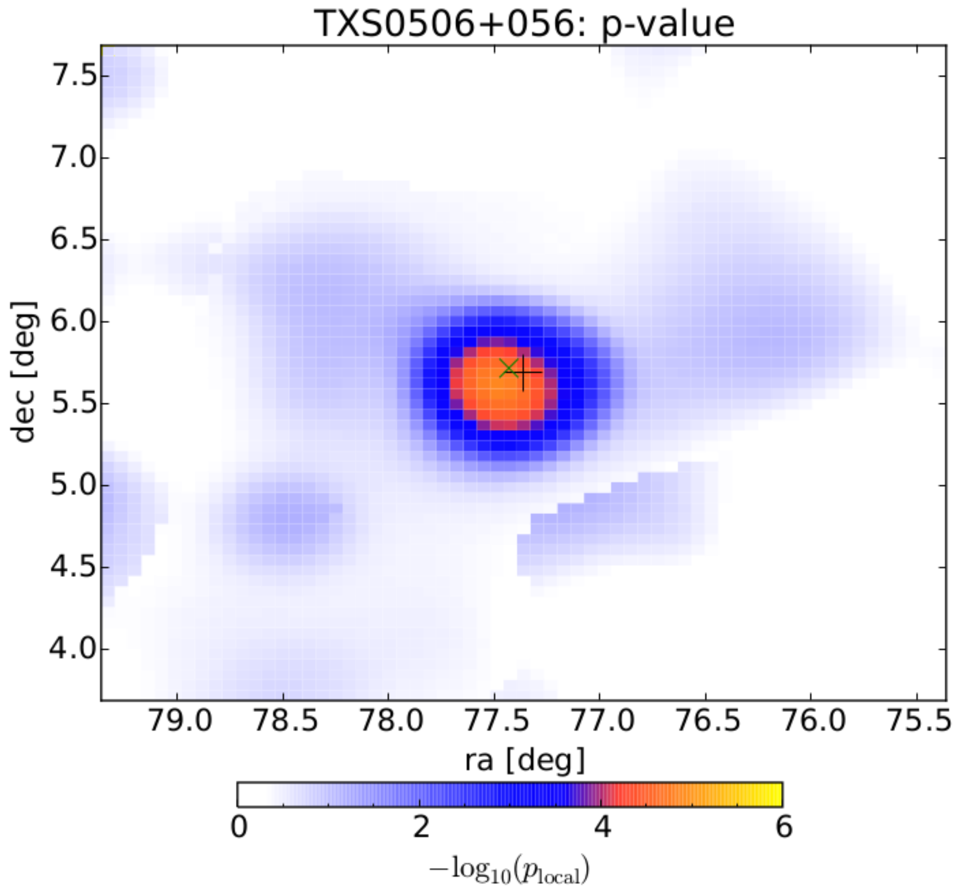

Figure 4.16: *Point Source Likelihood landscape around the TXS 0506+056 with 10 years of data (full sample). There is little change compared to the map with 9.5 years of data. The exact center of the map, the TXS 0506+056, is almost unaffected. The surrounding excess seems dimmer, but sharper and more centralized.*

ing a longer flare with the same properties can still strengthen a neutrino-gamma-correlation hypothesis.

The TXS 0506+056 will remain an interesting target of neutrino point source searches and multimessenger observations in general. The possibility to run a fast-track unblinding update within IceCube is an important step towards neutrino astronomy, moving towards observation of sources.

Chapter 5

Discussion

In the context of the TXS 0506+056 flare coincident with an IceCube EHE event, a number of questions remain. The IceCube collaboration investigated whether there is a significant contribution in neutrinos from the gamma-ray flare in September 2017.

5.1 Time-Dependence of the Signal

Most of the high-weighted events contributing significantly to the likelihood originate from the IC86_II-IV sample (15 of 25 total, 7 of 14 fitted events). This is intriguing, as the GFU partial sample has almost the same livetime, but contributes few events to the result (6 of 25, 4 of 14). The subdominance of the GFU period with respect to the IC86_II-IV appears striking - even without the expectation that the TXS 0506+056 emits neutrinos in the strong flare in September coincident with IceCube-170922A. Indeed is this period of gamma-ray activity almost devoid of neutrinos except for the EHE event. Instead one sees a clustering around December 2014 in Fig. 5.1. The events can be found in table A.1 in the appendix.

Hadronic models of gamma-ray emission predict correlated neutrino emission. Neutrino emission models of blazars predict gamma-ray emission alongside the neutrinos (see section 1.3). For the flare in 2017 coincident with IceCube-170922A, IceCube only detected the EHE event. The gamma-ray high-state period from 2017 March to October does not contribute visibly to the neutrino signal. This type of behavior has been found in other blazar objects, for example in [IceCube et al., 2017]. A likely explanation is purely leptonic production of gamma-rays in the source for the time window of the flare. The arrival of the EHE event from the source direction on the other hand is a clear sign for hadronic processes. The physics of the source will need careful investigation, but offer the chance to learn about blazar behaviour and the multimessenger connection of neutrinos and photons.

For IceCube neutrino point source searches, seeing signal in a clearly time-dependent fashion has obvious implications. Assume that the TXS 0506+056 is a typical neutrino emitter: time-integrated source searches as presented here can be improved by adding a time-dependent term to the likelihood. This is what has been done successfully in [The IceCube Collaboration, 2018] additional to the steady analysis in this work. One can disregard background-dominated time windows and selectively accumulate signal. The advantage lies in the possibility to distinguish signal and background better - signal comes in short bursts, background is constant in time. In the case of the TXS, any constant emission could be random noise from a diffuse background. Since this background adds up over the whole 9.5 (10) years of livetime, a significant steady detection needs many signal neutrinos. The discovery

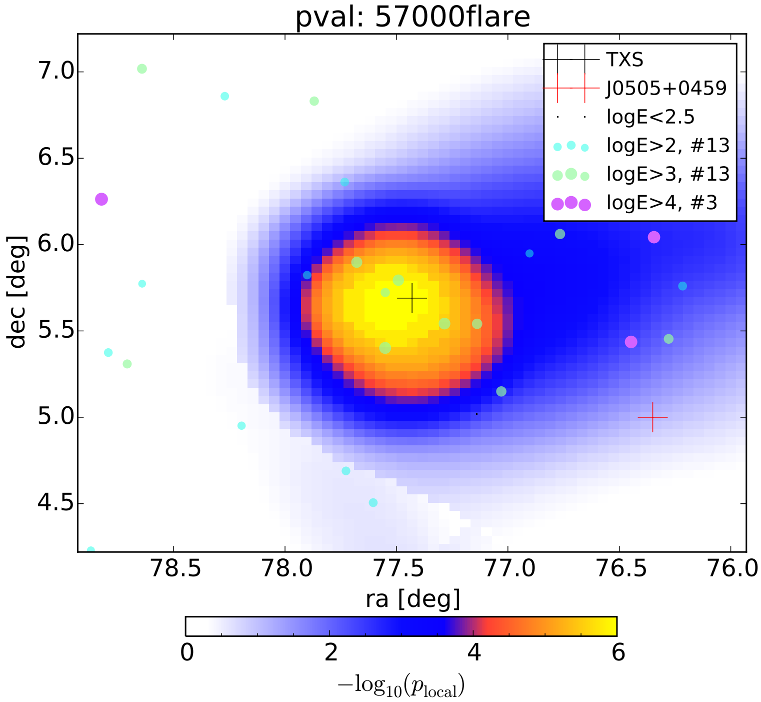

Figure 5.1: *Skymap section of the likelihood landscape around the TXS 0506+056 during the neutrino flare centred in December 2014. The time is restricted to the flare period, and the significance clusters around the TXS. The second blazar in the field, the PKS 0502+049 (marked by its BZCat name) is clearly not connected to the neutrino flare. The large extension of the significant region around the TXS is due to the small number of events contributing to the test.*

potential for the TXS steady analysis lies at 10.5 events for **Evidence** or at 17.08 events for **Discovery**.

In contrast, a flare happens in a possibly very short time window, so the diffuse background events in that window are very few. Here, a much smaller number of signal neutrinos can be enough for detection in a short window flare. Looking at the ~ 13 events during the December 2014 neutrino flare that contributed to the number of fitted events (entering the LLH as 'partial events'), chances of detection are elevated in the time-dependent channel[1].

5.2 TXS 0506+056 in light of the IceCube Blazar limits

With the analysis presented here and in [The IceCube Collaboration, 2018], IceCube has shown that a blazar appears to emit neutrinos as a point-like source. This comes as a surprise after not finding excesses in diverse catalog searches previously, but is well within the bounds set by the analyses in [Huber, 2017], [Aartsen et al., 2017b]. It makes up $\sim 1\%$ of the diffuse astrophysical neutrino flux, therefore being well below the limits set by IceCube.

Previous searches tested single and catalogs of blazars for neutrino signal. The object choices are phenomenologically motivated: Blazars are mainly chosen by proximity and gamma-ray brightness,

[1] [The IceCube Collaboration, 2018] finds a 3.5σ excess for the neutrino flare around December 2014.

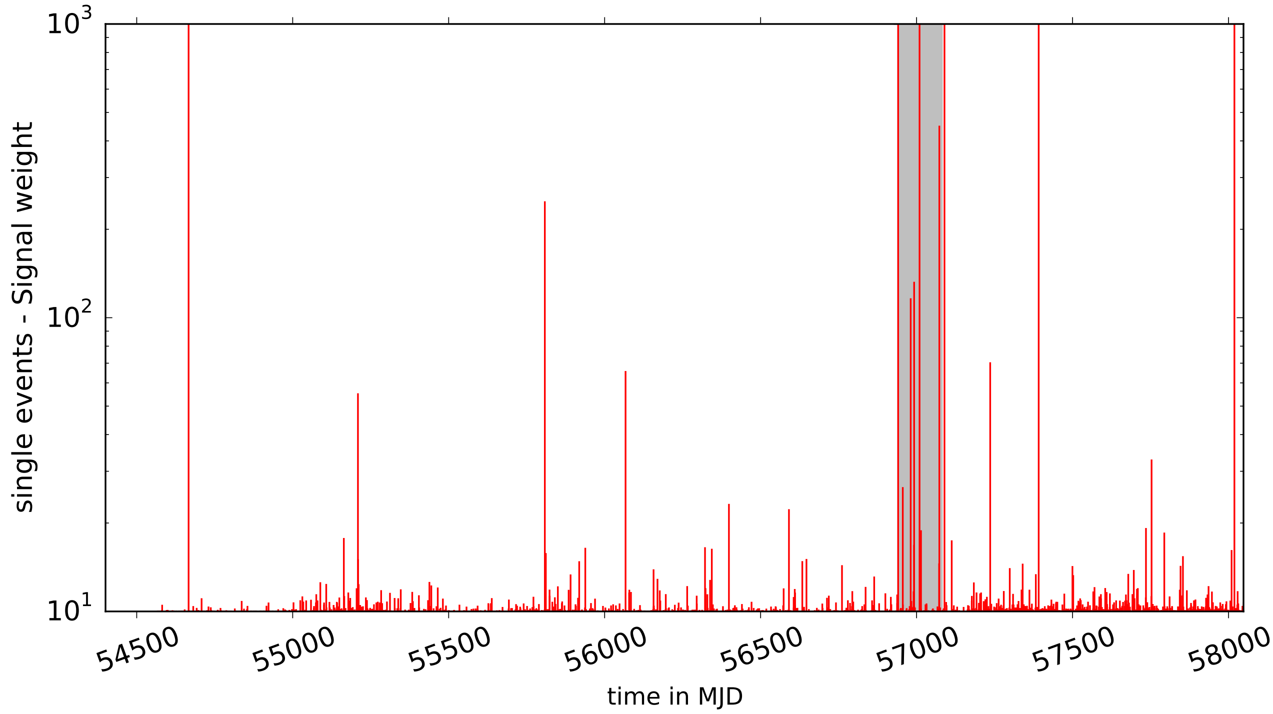

Figure 5.2: *Arrival time of events near TXS 0506+056. Each red vertical line corresponds to one event in the 9.5 years sample. The height of the lines is proportional to the signal weight of an event divided by its background probability. This is a direct measure of how much it contributes to the likelihood. The greyed-out area marks the best-fit time window of the timedependent box analysis (13.12.2014 ± 79 d) in [The IceCube Collaboration, 2018]. It visibly contains more high-weighted neutrino events than at other times during the sample livetime. The signal weight is determined by the spacial proximity measured in angular event uncertainty and by the energy weight. The highest-weighted event at MJD 58018 (corresponding 22.09.17) is the EHE event IceCube-170922A. Since the signal weight of IceCube-170922A is out of proportion with the other events, the plot has been truncated above an arbitrary value. Events that are affected by this cut are with very high probability signal.*

grouped by observational properties. In source list searches (see [Aartsen et al., 2017a]), a selection by photon emission is intended: the closest and strongest photon sources pose outstanding neutrino source candidates. An objects apparent luminosity decreases with the distance - very close sources are brighter in gamma photons and maybe in neutrinos as a consequence. An objects real luminosity in high-energy photons is possibly connected to the neutrino luminosity via the energy content of the source. Conversely, in catalog searches, a selection in gamma-brightness occurs as a bias effect: sources below a certain threshold do not enter the catalog. The results of all searches for neutrino emission in blazars have been negative so far, with only [Resconi et al., 2017] finding an excess in connection with cosmic rays.

This raises the question whether the TXS 0506+056 is an atypical object. In terms of its brightness, it definitely is: comparing the SEDs of MRK 421 and the TXS (Figs. 1.2 and 2.4), they are similarly bright in the radio and low gamma bands. Due to their different distance to Earth, their luminosity must differ as well: the TXS is located at redshift 0.3, the Markarian at z = 0.03. Apparent luminosity in the cosmological framework scales with $1/z^4$, with a reciprocal square contribution from the sphere surface expansion at distance d, a inverse linear contribution from the decreased radiation rate from

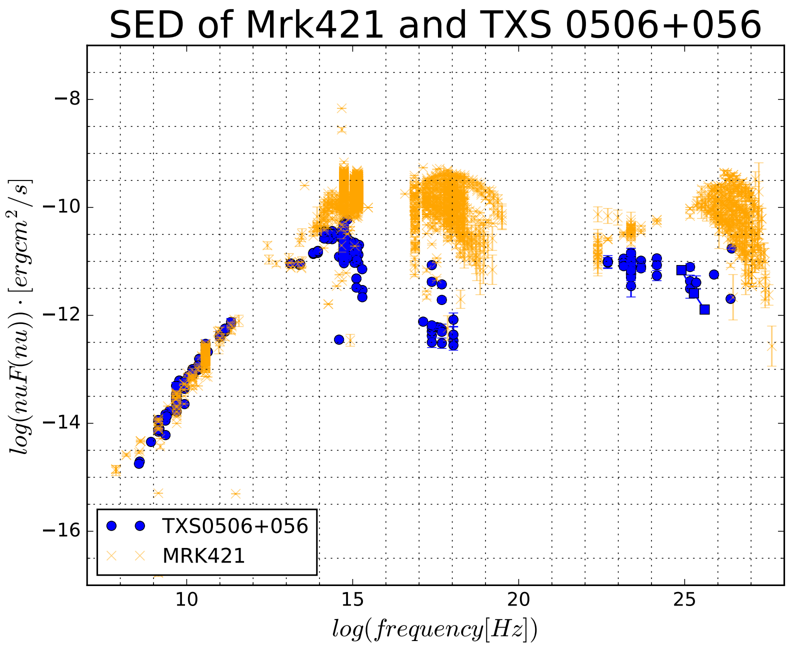

Figure 5.3: *Spectral Energy Distributions of the MRK 421 and TXS 0506+056, energy flux over frequency. Their luminosity in radio is almost identical even though their distance to Earth is not. The TXS is located at redshift 0.3, the Markarian at $z = 0.03$, the luminosity scales approximately with z^{-4} (surface scales with the square, collection area and rate scale linearly with reciprocal z). This means that the TXS is orders of magnitude brighter than the Markarian 421 at the point of emission.*

expanded space during light travel and a final inverse linear from the expansion of the light collection area. In consequence, the TXS is approximately 1-4 orders of magnitude brighter than the MRK 421 in different photon bands. In the 3FHL, there are only 97 of 1558 sources that are brighter than the TXS above 10 GeV.

On the other hand, the limits from previous searches still only allow weak statements on the single source TXS or single blazars in general. Their main statement is that blazars do not contribute a significant fraction to the entire diffuse astrophysical neutrino flux. Especially if the search intrinsically assumes that blazars or subsets of those emit according to the diffuse flux (by looking for the same spectral index for example), the analysis loses sensitivity to more general signal. This does not imply that blazars do not emit neutrinos, nor that a single blazar cannot be a significant neutrino source. Additionally, time-dependent searches provide stronger tools to search for signal in variable objects than the standard steady searches. In the case of the TXS, the steady analysis could not find as much of an excess as the time-dependent, prior to the IceCube-170922A arrival.

In short, the detection of further blazar objects in neutrinos is very well possible. The TXS 0506+056, a variable, bright IBL, can serve as a first example what to look for and how to model blazar (neutrino) emission. Hopefully the discoveries yet to come will lead to detailed understanding of blazars as neutrino and cosmic ray sources.

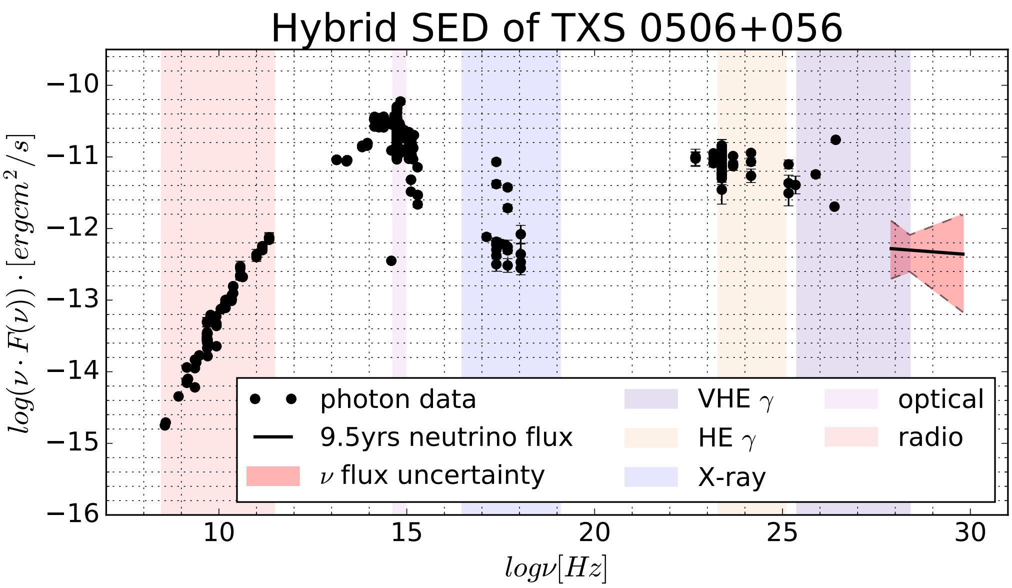

Figure 5.4: *Hybrid spectral energy distribution of the TXS 0506+056 - photon data and the best fit neutrino flux with uncertainties. The different wavebands are marked for convenience. The neutrino flux is translated to photon frequency (on the coordinate) via the neutrino energy to photon energy to photon frequency in vacuum unique relation - the abscissa is a flux, valid for neutrinos and photons. The neutrino energy band is then defined as the sensitive energy range of the 9.5 years steady analysis at 68% CL, 32 TeV to 3.6 PeV for a spectral index of γ =2.1. Qualitatively assessed, the time-averaged (steady) neutrino flux fits in well with the time-averaged photon data of the second hump. As shown above, the source is variable in neutrinos and in gamma-rays, so a comparison in flaring state is also relevant. This is provided for example in [Padovani et al., 2018].*

Chapter 6

Summary and Conclusion

I have presented the time-integrated point source search results at the position of the TXS 0506+056. The arrival of EHE event IceCube-170922A triggered an Online alert finding a coincident gamma-ray flare of the blazar, warranting a deeper search of IceCube data. I find for the unbiased analysis a non-significant excess that is increasing as more data is added to the hypothesis test (2.3σ). For the full dataset, the analysis provides strong evidence against the background hypothesis of no neutrino emission at the position. Following up this observation, there is a detection of an accumulation of signal neutrinos in a time-window around December 2014. A parallel time-optimized search on the same dataset finds statistically significant evidence for this neutrino flare. The IceCube pointing and reconstruction capabilities were validated - for the first time against a likely extragalactic source. Having the source distinction capability verified, a reported high-energy flare at the TXS 0506+056 position at the same time is the only consistent correlation in the region of interest. The TXS 0506+056 is likely the first identifiable point source of astrophysical neutrinos, showing a smoking-gun proof of hadronic acceleration processes and cosmic ray acceleration.

The results have been validated within the sample reconstruction by a number of cross-checks. Those include artificial uncertainty increase and fallback fits within the sample, development of a prototype reconstruction using a new pulse cleaning method and the resimulation of selected events with latest IceModels.

Future neutrino point source searches can draw from this result the necessity to employ time-optimized methods to include source variability into their hypotheses. The exact evolution of this source and the December 2014 flare can be used to model probable processes for neutrino acceleration and re-feed this into source searches. The possibility of fast-track or even automated searches on neutrino data is exciting, as it enables IceCube to move on towards astronomy and observation. Indeed the multimessenger connection is necessary in discovering new physics in blazars. The combination of the complete information available for objects under study is eminently important. Parallel availability of observations in all bands is growing rapidly and will hopefully incorporate neutrino astronomy soon.

The compelling evidence for the first extragalactic neutrino source in IceCube is a major step for neutrino and multimessenger astronomy. As soon as subsequent source detections follow, this will help to solve the century-old puzzle of the origin of Cosmic Rays and open up a new window to the high-energy universe.

Appendix A

Supporting Material

A.1 Neutrino Oscillations

In the Standard Model of particle physics, neutrinos are massless particles. They interact only via weak processes. In this framework, it is expected that the sun emits an electron (anti-) neutrino for each $\beta-$decay process in its fusion reactions. Those leave the sun's core and can be detected at Earth. The number of neutrinos arriving at Earth can be calculated precisely. The theoretical predictions were made by Bahcall in [Bahcall, 1964] and yield a neutrino rate of $2.5 \pm 1 \cdot 10^7 cm^{-2} s^{-1}$ for the ^{7}Be$(p,\gamma)^8$B reaction. The rate that was found by Davis in [Davis et al., 1968] is lower than that: $2 \cdot 10^{-6} cm^{-2} s^{-1}$. More precise measurements revealed that one finds exactly 1/3 of the expected number of electron neutrinos. The missing fraction changed their flavour on the way to Earth. This is possible because the flavour Eigenstates of the neutrinos are not identical to the mass Eigenstates. They are produced and detected in their flavour Eigenstates since they interact weakly in both processes. Once they travel freely, they assume their mass Eigenstates via:

$$|\nu_\alpha\rangle = \sum_i U_{\alpha i} |\nu_i\rangle \tag{A.1}$$

Here Greek letters denote the flavour, numbers the mass Eigenstates. U is the transition matrix element. 'Travel freely' means in this context that the baseline between two weak interactions is sufficiently long. The probability to find a neutrino in mass Eigenstate i after a time t can be expressed as

$$|\nu_i(t)\rangle = e^{-iEt} |\nu_i 0\rangle = e^{-ipt} e^{-m_i^2 \frac{L}{2E}} |\nu_i 0\rangle$$

Here E is the energy Eigenvalue of the Hamiltonian in vacuum. The first term is the stationary solution of the time-dependent Schrödinger equation, which is replaced using the energy-momentum relation $E \approx pc + \frac{m_i^2 c^4}{2E}$. L is the baseline length. A certain transition probability on a fixed baseline L depends on the involved flavours and the neutrino energy. m_i the neutrino mass and has to be non-zero in the case of oscillations - flavour transitions are thereby physics beyond the standard model. The phenomenon is called oscillation as it can be described by harmonic oscillator solutions. Explicitly, for a hypothetical two flavour transition with mixing angle θ, the matrix element reads, in analogy to a 2D rotation,

$$U = \begin{pmatrix} cos\theta & sin\theta \\ -sin\theta & cos\theta \end{pmatrix}$$

Inserting this into Eq. A.1, one finds a transition probability in a two-flavour system of

$$P(\nu_i \to \nu_j|L) = sin^2 2\theta sin^2 \frac{\Delta m^2 L}{4E}$$

As the travelled length L enters in the sine, one observes a periodic pattern in length - oscillations between the two states. In the case of astrophysical neutrinos, the baseline L is on the order of 1 GPc (calculated for the TXS 0506+056 at z $\approx$ 0.33), so one expects all flavours in equal ratio from a faraway cosmic accelerator.

A.2 Fermi Mechanism

The origin of cosmic rays is a still-unsolved and fundamental problem of astroparticle physics. There exists no definite knowledge about their sources, or the process(es) that accelerate them to GeV-EeV energies. Yet taking a look at the observed properties of the incoming particles can lead us towards understanding. This section follows closely [Gaisser et al., 2016, ch.12] for the derivation of Fermi acceleration. Fermi proposed acceleration processes where particles are trapped in cosmic plasma and collide elastically with its magnetic fields. Statistically, those produce an escaping population with an energy distribution which follows a single power law [Fermi, 1949].
The physical principle behind the collisions follows this logic: assume a particle of initial energy E_0 collides n times in the plasma and gains on average an energy of δ. With each collision, it has the probability P_{esc} to leave the confining fields. Then its final energy E_n upon leaving the plasma with probability P_n will be:

$$E_n = E_0(1+\delta)^n \tag{A.2}$$

$$P_n = (1 - P_{esc})^n \tag{A.3}$$

Inversely, one needs n collisions to reach the energy E:

$$n = \frac{ln\left(\frac{E}{E_0}\right)}{ln(1+\delta)} \tag{A.4}$$

The numerical relation for N particles with energies larger than E can be calculated by summing over all encounters m $\gg$ n as

$$N \propto \sum_{m>n}^{\text{inf}} (1 - P_{esc})^m = \frac{(1 - P_{esc})^m}{P_{esc}} \tag{A.5}$$

Substitution of A.5 into A.4 yields:

$$N \propto \frac{1}{P_{esc}} \left(\frac{E}{E_0}\right)^{-\gamma} \tag{A.6}$$

$$\gamma \sim \frac{P_{esc}}{\delta} \tag{A.7}$$

This is a powerlaw distribution where γ denotes the spectral index. The observed spectrum of cosmic rays follows this shape with one limitation: the spectral index of the CR spectrum changes at around 1 PeV from 2.7 to 3.1 [Gaisser et al., 2016, p.2]. The resulting curve is called a 'broken powerlaw' indicating a continuous, but not necessarily smooth transition between two powerlaws of different indices. So the CR spectral shape is a natural consequence of this simple mechanism which was derived by Fermi [Fermi, 1949] from the kinematics of moving gas clouds. The described process is called second-order Fermi mechanism due to the proportionality of $\delta \propto \beta^2$, the speed divided by speed of light. This is derived by averaging over the incoming angles of particles relative to a cloud, then averaging over the outgoing angles. The full calculation can be found in [Gaisser et al., 2016, 12.2]. For known environments containing plasma clouds, the magnetic field strength and kinetic energy stored in the medium is not sufficient to accelerate CR to beyond-TeV energies. More efficient acceleration is necessary to explain the observed CR particles at highest energies. An environment of particles being captured between plane shocks is found to produce more energetic particles. This case can for example be found in supernovae, where the average in outgoing direction yields a linear dependence in β. Supersonic shocks in Supernova blasts provide more kinetic energy than interstellar gas, so the energy gain per collision is on average increased as well compared to the second-order mechanism. It can be shown though that this is not yet sufficient for the highest energetic CR reaching $O(EeV)$ (UHECR, ultra-high energy cosmic rays). They have to be produced in even more energetic environments like Active Galactic Nuclei (AGN) and blazars with jets widely more powerful than supernova shockwaves. If these jets interact either with ambient material or themselves, the combination of high energy gain per particle collision and longer trapping time in the resulting shocks could explain the observed cosmic ray spectrum at highest energies.

This hypothetical framework of acceleration is based on the shape of the cosmic ray spectrum. It is supported by observations of the Fermi mechanisms at lower energy scales, but has still to be verified for UHECR production. For this work, it can be viewed as a first-order approximation of the far more complex mechanism behind CR acceleration. Nevertheless, it comes with two relevant consequences: first, the sources of the highest energetic cosmic particles must be extragalactic, point-like and extreme objects. Second, strong shock acceleration can intrinsically lead to powerlaw spectra.

A.3 Early Blazar models

In [Mastichiadis and Kirk, 1995], a time-dependent, self-consistent model of cosmic particle acceleration in jetted AGN is presented. The underlying mechanism is a first-order Fermi acceleration in the relativistic shock. The kinetic distributions of all particles of the blob are averaged to allow for analytic calculation - the modelling is stochastical and all properties assumed to be uniform through the source. All processes are modelled time-dependently to account properly for source variability. The framework follows, for each type of particle that participates in acceleration, a sinks-and-sources approach. The change in particle density is calculated as

$$\frac{\partial \hat{n}_p(p,t)}{\partial t} + \frac{\partial}{\partial p}\left[\frac{p}{\hat{t}_{acc}}\hat{n}_p(p,t)\right] + \frac{\hat{n}_p(p,t)}{\hat{t}_{esc}} = \mathcal{Q}_{inj}\delta(p - p_{inj}) + \hat{\mathfrak{L}}^p(\hat{n}_p, p, t)$$

In this case, the formalism treats the proton population and is differential in momentum p. All quantities $\hat{x}$ denote averages, t is time, with the acceleration time t_{acc} and the average time after which a proton leaves the acceleration region t_{esc}. p_{inj} is the momentum at which protons are injected. The first term is the change in particle density. Via the second term, the population gains additional energy by Fermi acceleration. The third term accounts for particles leaving the acceleration region. $\mathcal{Q}$ is the source term, collecting particles that are injected into the region. $\hat{\mathfrak{L}}$ denotes the energy losses. This includes all possible interaction reaction, which are well-described for protons. Setting up this equation for all particle species and explicitly defining source and loss terms allows to simplify the system into a set of (cross-coupled) differential equations that the authors solve numerically.

They find that in this framework, non-thermal emission occurs not because of the injected spectrum, but as a result of the acceleration process. Another natural consequence of this model is the existence of feedback loops. As an example, they discuss the pair-production-synchrotron instability. This process occurs when the number density of relativistic protons above a certain energy exceeds a critical value. This triggers pair production from those protons reacting with ambient photons. The pairs lose energy via radiative processes. The emitted photons themselves can interact with the proton population, providing a feedback. The outcome of this scenario can be a catastrophic drive, but more likely, the increase in photon density cools the proton population. The depletion of high-energy protons restores the initial state of acceleration and generates a loop. Accordingly, a source described by this model would display (periodic) variability.

In the successive work [Mastichiadis and Kirk, 1997], a self-consistent model of the photon emission of MRK 421 based on one single population of electrons is presented. Those electrons are contained in a relativistic bulk mass ('the blob') and emit photons in the radio-to-X-ray bands. The photons can undergo Inverse Compton upscattering and get accelerated to gamma energies. The mechanism is called SSC (synchrotron self-Compton) model, as the photons in both bands are from the same initial population.

Motivated by gamma-ray observations of MRK 421, the proton population from the precursory work is disregarded. In this (still simplified) framework, the emitted photon flux in different wavelengths depends on the source radius, the ambient magnetic field strength, the electron spectrum injected into the blob, the effective escape time of the electrons, and the Doppler factor of the blob in the observer's rest frame. The last parameter takes into account that the blob is highly relativistic and beaming of the emitted photons occurs. This is an effect of angular correlations in the special relativistic treatment of the blob. It leads to apparent superluminal motion of the bulk mass. The consequence is an increase in intensity along the axis of motion (the jet axis in the case of blazars) and an apparent shortening of variability timescales (see [Urry and Padovani, 1995] for a detailed discussion).

The authors apply their model to both the steady-state emission of the blazar and the flaring state. In this picture, a change in the electron spectrum (precisely, the maximal electron Lorentz factor) or the ambient magnetic field is sufficient to generate a flare in the source. With respect to the AGN variability observations, it is noteworthy that for a flare generated by a change in the electron spectrum, X-ray variability occurs faster. Longer wavelength photons (optical, UV) respond slower to the flare process. For a flare created by increasing the maximal flatness of the photon spectrum, only the X-ray and TeV gamma-rays show flaring behavior. This reproduces behavior found in some blazar flares. From the model, parameter bounds can be inferred: they find that synchrotron photons are being emitted up to frequencies of 10^{18} Hz and Inverse Compton photons can reach 10^{27} Hz. This aligns well with observed spectral energy distributions of known blazars.
In summary, blazar emission and especially variability can be modelled by assuming one central engine, the jet. Jet non-thermal emission can be explained by a Fermi-based shock acceleration. Even for different blazar flare types, basic assumptions lead to variable behaviour consistent with observations.

A blazar that follows the SSC model will not produce neutrinos since the entire photon emission is purely lepton-induced. For neutrinos, hadronic processes are required. The model in [Mastichiadis and Kirk, 1995] treats a proton population. Here indeed proton collisions generate neutrinos and neutrons which later decay under neutrino emission. Pair-Production-Synchrotron instabilities boost neutrino production, generating 'neutrino flares' in parallel to photon flares. One issue in this context is the final spectrum they find with their parameter set: their neutrino distribution is sharply cut off after a few TeV. With the observation of PeV neutrinos in the diffuse flux in [Aartsen et al., 2013a], this is unlikely the correct description.

A.4 A dynamical Blazar model example

Dynamical models of variable blazar emission are currently being developed. Theoretical descriptions are progressing from stationary solutions towards processes that lead to variable behaviour [Petropoulou and Mastichiadis, 2018]. Strong candidates are self-regulating feedback loops. An example process can look like this:
The proton energy density in a source increases. Protons lose energy via synchrotron photons[1]. With rising proton energy, more photons are created in the source via photon-proton-coupling. This increases the photon density, leads to higher photon production, and further increases photon density. This effects a runaway reaction: photon density increases and increases. Once a threshold is passed, the source/blob enters a critical state. In the critical state radiative cooling of protons can become efficient, removing photons from the region until the state becomes subcritical. Then the initial change occurs again. This means such an object would display strong variability by repeating the described loop. In the following diagram the process is illustrated:

$$
\begin{tikzcd}
\text{Subcritical Blob} \arrow[r] & E_p \text{ increases} \arrow[r] & \text{More photon targets} \arrow[r, bend left] \arrow[d, "{>threshold}"] & \text{Reactions increase } N_{ph} \arrow[l, bend left] \\
& & \text{Critical State*} \arrow[d] & \\
\text{Photon density decreases} \arrow[uu] & & \text{Radiatively efficient*} \arrow[ll] &
\end{tikzcd}
$$

N_{ph} is the number of photons, E_p is the proton energy density. States marked with a * are candidate for neutrino emission: high-energetic protons and a large density of target photons are present.
Tests of these models could provide valuable insights in blazar physics - flares and high states of blazars are not well-understood. Detecting neutrino and gamma emission in coincidence from one source would provide a testbed for these models. In turn, a detailed prediction of neutrino emission from blazar flares can increase the chances of neutrino point source detections.

[1]This process and losses via secondaries (photo-pion etc.) is inefficient. Inefficient proton cooling in the blob leads to a steady state.

A.5 Figures

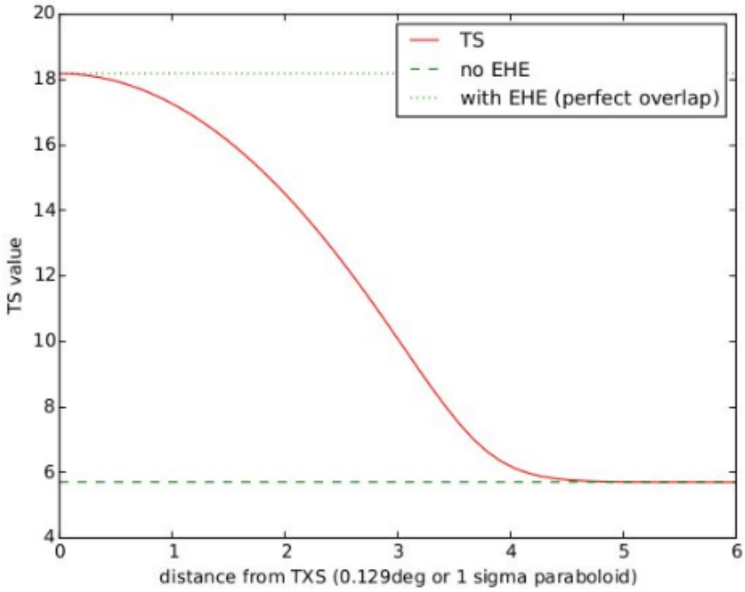

Figure A.1: *Effect of the spacial term on the likelihood. $\mathcal{TS}$ value for the LLH calculation at the TXS 0506+056 position is shown for the EHE event IceCube-170922A. The dotted line is the result of the full dataset, the dashed line is the result with the EHE event completely removed. The x-axis is in units of angular event uncertainty for the EHE event. Moving it out by a few times its error has the same effect as completely removing it. "Paraboloid" refers to the reconstruction fit that attemps to approximate the directional likelihood space with a parabola.*

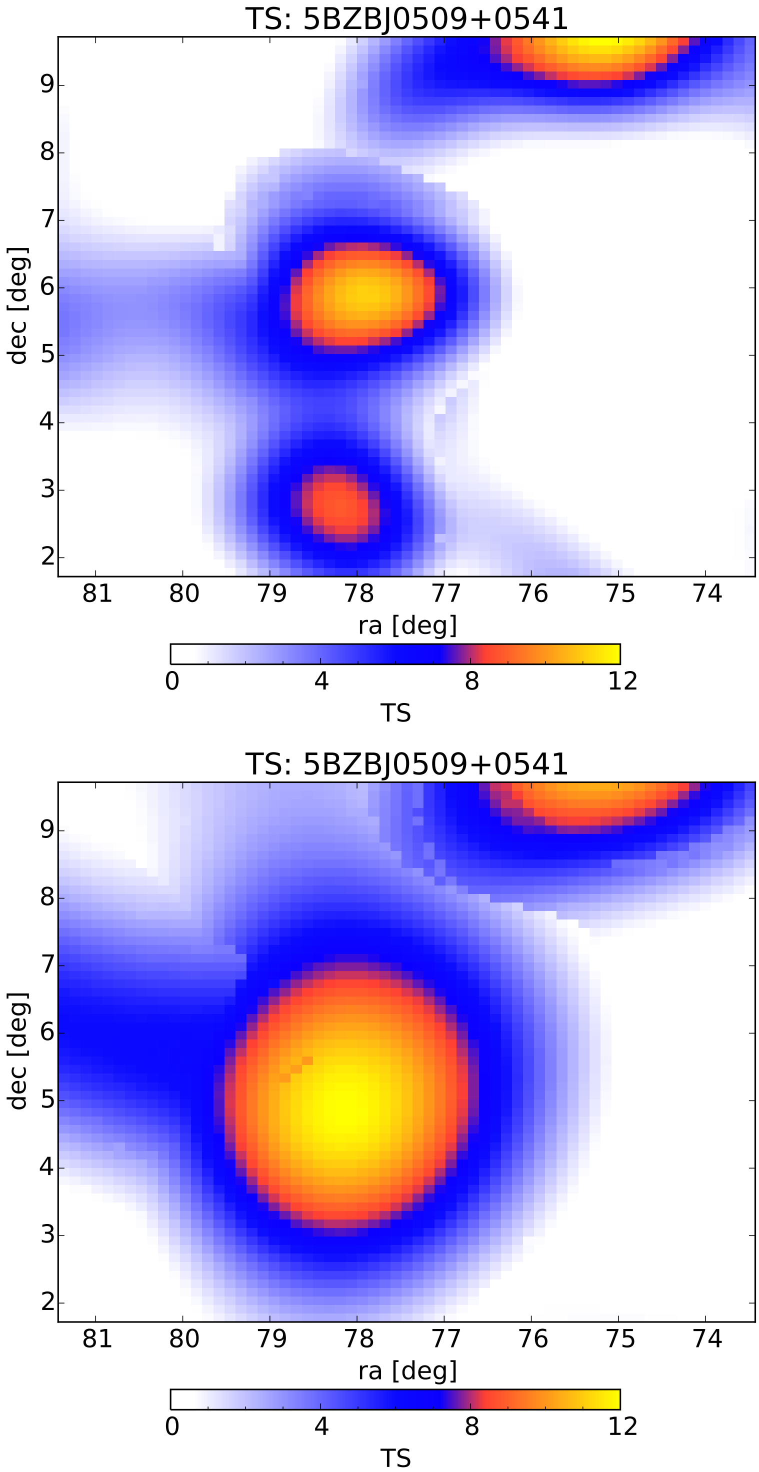

Figure A.2: *p-value maps for the TXS 0506+056 area LLH-fitted with the full sample. Each event's angular uncertainty has been changed to one degree in the upper plot, in the lower the new value is two degrees. In the upper skymap, there is little change apart from a few events in the upper right corner merging into a warm spot, and the hotspot at the TXS position getting smeared out.*

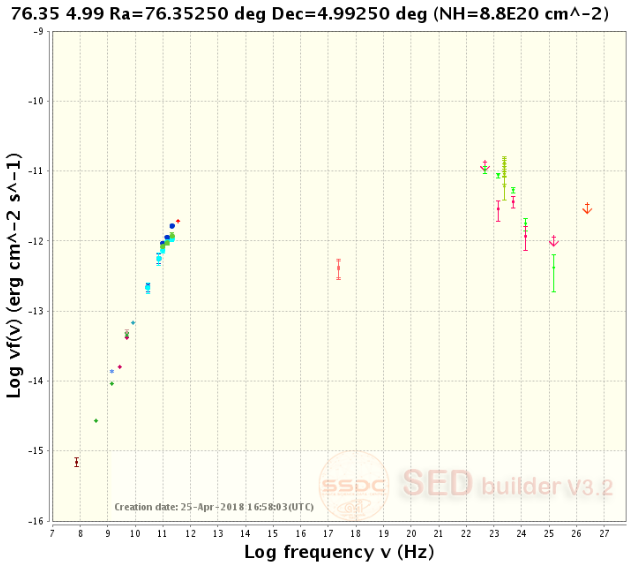

Figure A.3: *Spectral Energy Distribution of PKS 0502+049. It is a flat-spectrum radio quasar at redshift ∼1. Its synchrotron peak is had to determine from available data, but its IC second hump drops sharply, making it an unlikely source of astrophysical neutrinos.*

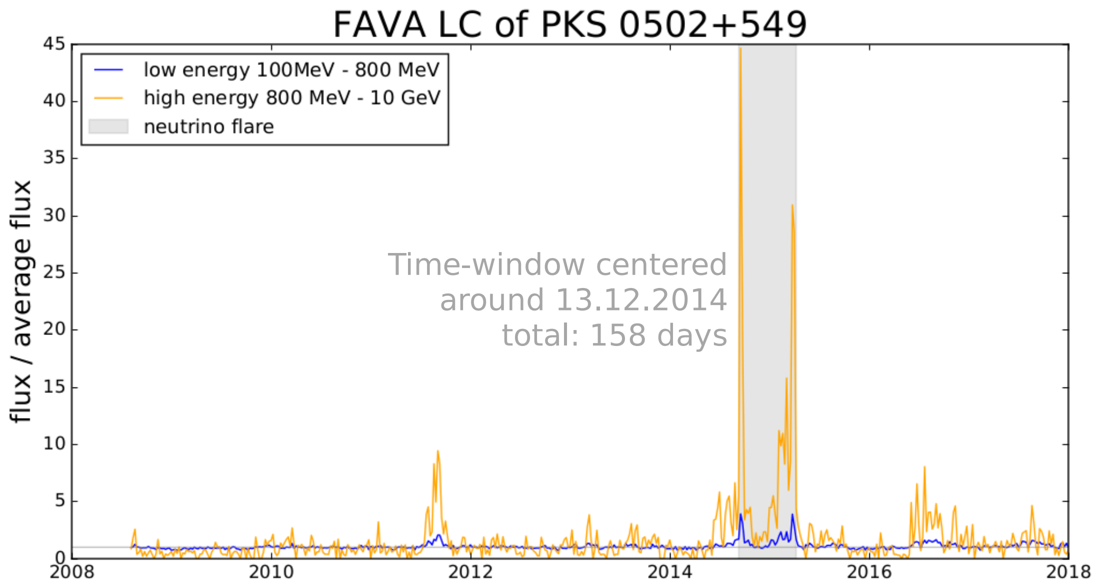

Figure A.4: *Lightcurve of the PKS 0502+049, the source near the TXS 0506+056, taken from FAVA [S. Abdollahi, 2017]. The PKS source is located at redshift*[2]*. Marked as a grey rectangle is a neutrino flare of the TXS, shown in Fig. 5.2. Possible reasons for this coincidence include: 1) The neutrino flare originates actually from the PKS (misreconstruction in IceCube). 2) The FAVA lightcurves in the area are contaminated - FAVA uses aperture photometry, so a confusion cannot be excluded. 3) This is pure coincidence. Point 2 has been treated exhaustively in this thesis and can be seen as unlikely.*

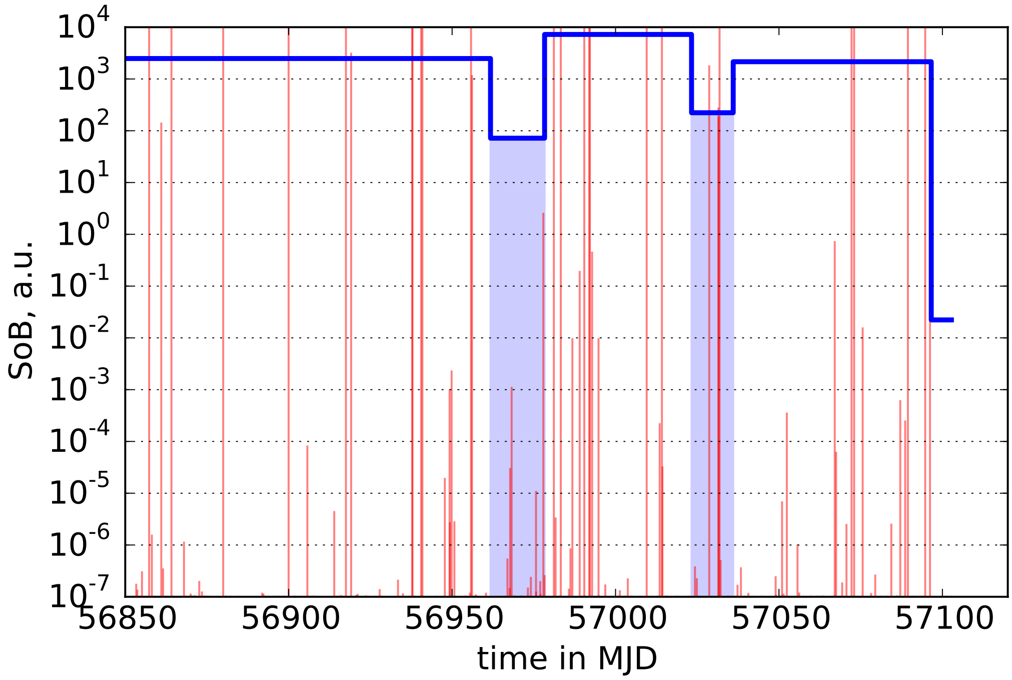

Figure A.5: *Neutrino arrival times during the 2014 flare. Each red vertical line marks an event. The height corresponds to the event signal weight. The blue histogram is the scaled sum of all signal weights in the time range, accounting for bin width. The bins chosen for the blue curve correspond to the flare intervals in [Padovani et al., 2018] (courtesy N.Sakhayan, B.Arsioli). The blue shaded regions are the time windows of gamma spectral hardening and flux increase.*

A.6 Tables

Table A.1: *Event list of the 25 events with the highest contribution to the fit result with a marker line at 14 events. 14 is chosen as the arithmetical ceiling of the number of fitted signal events, so this list compiles the most probable 'neutrino signal' one sees from the position of the source under investigation. This is entirely based on statistics and the methods described in this work. IceCube doesn't claim to know which events are astrophysical and which atmospheric on an event-by-event basis, and IceCube doesn't claim that there is a neutrino source that can be identified with the TXS 0506+056. For the sample column, the numbers correspond to 1:IC40, 2:IC59, 3:IC79, 4:IC86_I, 5:IC86_II-IV, 6:GFU. The logE energy proxy is a different measure of the true neutrino energy for every sample, and only comparisons within one sample are precisely comparable.*

ra [deg]	dec [deg]	sigma [deg]	logE proxy [logGeV]	time [MJD]	sample
77.39	5.64	0.154	4.73	58018.87	6.0
77.86	5.05	0.925	4.56	57391.44	6.0
77.55	5.40	0.191	3.98	56940.91	5.0
77.28	5.54	0.386	3.91	57009.53	5.0
78.11	6.91	1.512	5.50	54666.33	1.0
77.68	5.90	0.185	3.70	57089.44	5.0
76.45	5.44	1.095	4.18	57072.99	5.0
77.32	5.28	0.368	3.57	55808.33	4.0
78.82	6.26	1.775	4.31	56992.16	5.0
76.34	6.04	0.506	4.14	56981.13	5.0
77.56	6.31	0.402	3.60	57236.01	6.0
76.76	5.38	0.555	3.68	56067.08	5.0
78.08	5.25	0.524	4.42	55209.21	2.0
77.55	5.44	0.404	3.24	57753.32	6.0
77.55	5.72	0.364	3.10	56955.79	5.0
77.17	5.80	0.360	3.04	56398.47	5.0
77.77	5.95	0.366	3.27	56590.87	5.0
77.30	5.73	0.461	3.02	57735.37	6.0
77.49	5.79	1.654	3.79	57014.19	5.0
77.29	6.01	0.314	2.85	57794.10	6.0
76.99	5.41	0.451	3.48	55163.98	2.0
77.14	5.54	0.983	3.46	57112.65	5.0
76.77	6.06	0.799	3.43	56991.94	5.0
76.12	6.39	0.492	4.20	56321.78	5.0
77.75	5.95	0.357	3.00	55938.00	4.0
77.37	6.41	0.449	3.35	56343.58	5.0

Bibliography

[Aartsen et al., 2016] Aartsen, M. G., Abraham, K., Ackermann, M., Adams, J., Aguilar, J. A., Ahlers, M., Ahrens, M., Altmann, D., Andeen, K., Anderson, T., and et al. (2016). Observation and Characterization of a Cosmic Muon Neutrino Flux from the Northern Hemisphere Using Six Years of IceCube Data. *Astrophys. J.*, 833:3. [Cited on page 36.]

[Aartsen et al., 2013a] Aartsen, M. G. et al. (2013a). Evidence for High-Energy Extraterrestrial Neutrinos at the IceCube Detector. *Science*, 342:1242856. [Cited on pages 13 and 77.]

[Aartsen et al., 2013b] Aartsen, M. G. et al. (2013b). Measurement of South Pole ice transparency with the IceCube LED calibration system. *Nucl. Instrum. Meth.*, A711:73–89. [Cited on page 50.]

[Aartsen et al., 2014] Aartsen, M. G. et al. (2014). Observation of the cosmic-ray shadow of the Moon with IceCube. *Phys. Rev.*, D89(10):102004. [Cited on pages 30, 55, and 56.]

[Aartsen et al., 2016a] Aartsen, M. G. et al. (2016a). An All-Sky Search for Three Flavors of Neutrinos from Gamma-Ray Bursts with the IceCube Neutrino Observatory. *Astrophys. J.*, 824(2):115. [Cited on page 4.]

[Aartsen et al., 2016b] Aartsen, M. G. et al. (2016b). Characterization of the Atmospheric Muon Flux in IceCube. *Astropart. Phys.*, 78:1–27. [Cited on page 27.]

[Aartsen et al., 2017a] Aartsen, M. G. et al. (2017a). All-sky Search for Time-integrated Neutrino Emission from Astrophysical Sources with 7 yr of IceCube Data. *Astrophys. J.*, 835(2):151. [Cited on pages 8, 13, 16, 22, 27, 33, 35, 36, 43, 47, 49, 50, 51, and 67.]

[Aartsen et al., 2017b] Aartsen, M. G. et al. (2017b). The contribution of Fermi-2LAC blazars to the diffuse TeV-PeV neutrino flux. *Astrophys. J.*, 835(1):45. [Cited on pages 9 and 66.]

[Aartsen, 2013] Aartsen, M. G. e. a. (2013). First observation of pev-energy neutrinos with icecube. *Phys. Rev. Lett.*, 111:021103. [Cited on pages 1 and 16.]

[Abdo et al., 2010] Abdo, A., Ackermann, M., Agudo, I., Ajello, M., Aller, H., Aller, M., Angelakis, E., Arkharov, A., Axelsson, M., Bach, U., and et al. (2010). The Spectral Energy Distribution of Fermi Bright Blazars. *Astrophys. J.*, 716:30–70. [Cited on page 5.]

[Ackermann, 2011] Ackermann, M., e. a. (2011). The Second Catalog of Active Galactic Nuclei Detected by the Fermi Large Area Telescope. *Astrophysical Journal*, 743:171. [Cited on pages 5 and 9.]

[Ackermann et al., 2015] Ackermann, M. et al. (2015). The Third Catalog of Active Galactic Nuclei Detected by the Fermi Large Area Telescope. *Astrophys. J.*, 810(1):14. [Cited on pages 5 and 9.]

[Ackermann et al., 2016] Ackermann, M. et al. (2016). 2FHL: The Second Catalog of Hard Fermi-LAT Sources. *Astrophys. J. Suppl.*, 222(1):5. [Cited on pages 5 and 9.]

[Ahlers and Halzen, 2014] Ahlers, M. and Halzen, F. (2014). Pinpointing Extragalactic Neutrino Sources in Light of Recent IceCube Observations. *Phys. Rev.*, D90(4):043005. [Cited on page 10.]

[Ajello et al., 2017] Ajello, M. et al. (2017). 3FHL: The Third Catalog of Hard Fermi-LAT Sources. *Astrophys. J. Suppl.*, 232(2):18. [Cited on pages 5, 22, 23, 25, and 26.]

[Ajello et al., 2015] Ajello, M., Gasparrini, D., Sánchez-Conde, M., Zaharijas, G., Gustafsson, M., Cohen-Tanugi, J., Dermer, C. D., Inoue, Y., Hartmann, D., Ackermann, M., Bechtol, K., Franckowiak, A., Reimer, A., Romani, R. W., and Strong, A. W. (2015). The origin of the extragalactic gamma-ray background and implications for dark matter annihilation. *The Astrophysical Journal Letters*, 800(2):L27. [Cited on page 5.]

[Bahcall, 1964] Bahcall, J. N. (1964). Solar neutrinos. i. theoretical. *Phys. Rev. Lett.*, 12:300–302. [Cited on page 73.]

[Bechtol et al., 2017] Bechtol, K., Ahlers, M., Di Mauro, M., Ajello, M., and Vandenbroucke, J. (2017). Evidence against star-forming galaxies as the dominant source of IceCube neutrinos. *Astrophys. J.*, 836(1):47. [Cited on page 4.]

[Braun et al., 2008] Braun, J., Dumm, J., Palma, F. D., Finley, C., Karle, A., and Montaruli, T. (2008). Methods for point source analysis in high energy neutrino telescopes. *Astroparticle Physics*, 29(4):299 – 305. [Cited on page 34.]

[C. Haack, 2017] C. Haack, C. Wiebusch, o. b. o. t. I. C. (2017). A measurement of the diffuse astrophysical muon neutrino flux using eight years of icecube data. In *Volume 301 - 35th International Cosmic Ray Conference (ICRC2017)*. [Cited on page 14.]

[Chang, 2018] Chang, Y.-L. (2018). Vou-blazars. https://github.com/ecylchang/VOU_Blazars. Virtual Observatory for Blazars. [Cited on page 23.]

[Chang et al., 2017] Chang, Y. L., Arsioli, B., Giommi, P., and Padovani, P. (2017). 2WHSP: A multi-frequency selected catalogue of high energy and very high energy gamma-ray blazars and blazar candidates. *Astron. Astrophys.*, 598:A17. [Cited on pages 5 and 9.]

[Chirkin, 2014] Chirkin, D. (2014). Event reconstruction in icecube based on direct event re-simulation. In *Proceedings of the 33rd International Cosmic Rays Conference*. [Cited on page 62.]

[Coenders, 2016] Coenders, S. (2016). *High-energy cosmic ray accelerators: searches with IceCube neutrinos*. Dissertation, Technische Universität München, München. [Cited on pages 27, 28, 29, and 41.]

[Davis et al., 1968] Davis, R., Harmer, D. S., and Hoffman, K. C. (1968). Search for neutrinos from the sun. *Phys. Rev. Lett.*, 20:1205–1209. [Cited on page 73.]

[E. Andres, 2000] E. Andres, e. a. (2000). The amanda neutrino telescope: principle of operation and first results. *Astroparticle Physics*, 13(1):1 – 20. [Cited on pages 13, 16, 28, 29, 55, and 92.]

[Fermi, 1949] Fermi (1949). On the origin of cosmic rays. *Physical Review*, 75(8). [Cited on pages 1, 74, 75, and 92.]

[Gaisser et al., 2016] Gaisser, T. K., Engel, R., and Resconi, E. (2016). *Cosmic Rays and Particle Physics*. Cambridge University Press, 2 edition. [Cited on pages 1, 4, 6, 7, 43, 74, and 75.]

[Greisen, 1966] Greisen, K. (1966). End to the cosmic-ray spectrum? *Phys. Rev. Lett.*, 16:748–750. [Cited on pages 18 and 92.]

[Halzen and Kheirandish, 2016] Halzen, F. and Kheirandish, A. (2016). High Energy Neutrinos from Recent Blazar Flares. *Astrophys. J.*, 831(1):12. [Cited on page 10.]

[H.M. Niederhausen, 2017] H.M. Niederhausen, Y. Xu, o. b. o. t. I. C. (2017). High energy astrophysical neutrino flux measurement using neutrino-induced cascades observed in 4 years of icecube data. In *Volume 301 - 35th International Cosmic Ray Conference (ICRC2017)*. [Cited on page 14.]

[Huber, 2017] Huber, M. (2017). Icecube searches for neutrinos from blazars. https://pos.sissa.it/301/994/pdf. [Cited on pages 9 and 66.]

[IceCube et al., 2017] IceCube, T., FACT, and Collaborations, M. (2017). Icecube search for neutrinos from 1ES 1959+650: Completing the picture. In *Proceedings of the 35th International Cosmic Ray Conference*, volume ICRC2017, page 969. Proceedings of Science. [Cited on pages 10 and 65.]

[Mannheim, 1995] Mannheim, K. (1995). High-energy neutrinos from extragalactic jets. *Astroparticle Physics*, 3:295–302. [Cited on pages 7 and 10.]

[Mastichiadis and Kirk, 1995] Mastichiadis, A. and Kirk, J. G. (1995). Self-consistent particle acceleration in active galactic nuclei. *Astronomy and Astrophysics*, 295:613. [Cited on pages 11, 75, and 76.]

[Mastichiadis and Kirk, 1997] Mastichiadis, A. and Kirk, J. G. (1997). Variability in the synchrotron self-compton model of blazar emission. *Astronomy and Astrophysics*, 320:19–25. [Cited on pages 6, 7, and 76.]

[M.G. Aartsen, 2017a] M.G. Aartsen, e. a. (2017a). The icecube realtime alert system. *Astroparticle Physics*, 92(Supplement C):30 – 41. [Cited on pages 15 and 27.]

[M.G. Aartsen, 2017b] M.G. Aartsen, e. a. (2017b). The IceCube Neutrino Observatory: instrumentation and online systems. *JINST*, 12(3). [Cited on page 11.]

[Mirzoyan, 2017] Mirzoyan, R. (2017). First-time detection of VHE gamma rays by MAGIC from a direction consistent with the recent EHE neutrino event IceCube-170922A. *The Astronomer's Telegram*, 10817. [Cited on page 23.]

[Mortlock et al., 2011] Mortlock, D. J., Warren, S. J., Venemans, B. P., Patel, M., Hewett, P. C., McMahon, R. G., Simpson, C., Theuns, T., Gonzáles-Solares, E. A., Adamson, A., Dye, S., Hambly, N. C., Hirst, P., Irwin, M. J., Kuiper, E., Lawrence, A., and Röttgering, H. J. A. (2011). A luminous quasar at a redshift of z = 7.085. *Nature*, 474:616–. [Cited on page 2.]

[Ojha and Valverd, 2018] Ojha, R. and Valverd, J. (2018). Fermi-LAT detection of enhanced gamma-ray activity and hard spectrum of TXS 0506+056, located inside the IceCube-170922A error region. *The Astronomer's Telegram*, 11419. [Cited on page 63.]

[Padovani and Giommi, 1995] Padovani, P. and Giommi, P. (1995). The Connection between x-ray and radio-selected BL Lacertae objects. *Astrophys. J.*, 444:567. [Cited on page 5.]

[Padovani et al., 2018] Padovani, P., Giommi, P., Resconi, E., Glauch, T., Arsioli, B., Sahakyan, N., and Huber, M. (2018). Dissecting the region around IceCube-170922A: the blazar TXS 0506+056 as the first cosmic neutrino source. [Cited on pages 69 and 82.]

[Padovani et al., 2015] Padovani, P., Petropoulou, M., Giommi, P., and Resconi, E. (2015). A simplified view of blazars: the neutrino background. *Monthly Notices of the Royal Astronomical Society*, 452(2):1877–1887. [Cited on page 25.]

[Paiano et al., 2018] Paiano, S., Falomo, R., Treves, A., and Scarpa, R. (2018). The redshift of the BL Lac object TXS 0506+056. *Astrophys. J.*, 854(2):L32. [Cited on page 23.]

[Patrignani et al., 2016] Patrignani, C. et al. (2016). Review of Particle Physics. *Chin. Phys.*, C40(10):100001. [Cited on page 13.]

[Petropoulou et al., 2016] Petropoulou, M., Coenders, S., and Dimitrakoudis, S. (2016). Time-dependent neutrino emission from Mrk 421 during flares and predictions for IceCube. *Astropart. Phys.*, 80:115–130. [Cited on page 10.]

[Petropoulou and Mastichiadis, 2018] Petropoulou, M. and Mastichiadis, A. (2018). Patterns of variability in supercritical hadronic systems. [Cited on page 77.]

[Resconi et al., 2017] Resconi, E., Coenders, S., Padovani, P., Giommi, P., and Caccianiga, L. (2017). Connecting blazars with ultrahigh-energy cosmic rays and astrophysical neutrinos. *Mon. Not. Roy. Astron. Soc.*, 468(1):597–606. [Cited on pages 9, 23, and 67.]

[S. Abdollahi, 2017] S. Abdollahi, e. a. (2017). The second catalog of flaring gamma-ray sources from the fermi all-sky variability analysis. *The Astrophysical Journal*, 846(1):34. [Cited on pages 6, 23, 25, and 81.]

[Smith et al., 2013] Smith, M., Fox, D., Cowen, D., Mészáros, P., Tešić, G., Fixelle, J., Bartos, I., Sommers, P., Ashtekar, A., Babu, G. J., Barthelmy, S., Coutu, S., DeYoung, T., Falcone, A., Gao, S., Hashemi, B., Homeier, A., Márka, S., Owen, B., and Taboada, I. (2013). The astrophysical multimessenger observatory network (amon). *Astroparticle Physics*, 45:56 – 70. [Cited on pages 19 and 92.]

[Stecker et al., 1991] Stecker, F. W., Done, C., Salamon, M. H., and Sommers, P. (1991). High-energy neutrinos from active galactic nuclei. *Physical Review Letters*, 66:2697–2700. [Cited on page 10.]

[Tanaka et al., 2017] Tanaka, Y. T., Buson, S., and Kocevski, D. (2017). Fermi-LAT detection of increased gamma-ray activity of TXS 0506+056, located inside the IceCube-170922A error region. *The Astronomer's Telegram*, 10791. [Cited on page 22.]

[The IceCube Collaboration, 2016] The IceCube Collaboration (2016). Very high-energy gamma-ray follow-up program using neutrino triggers from icecube. *Journal of Instrumentation*, 11(11):P11009. [Cited on pages 15, 17, and 27.]

[The IceCube Collaboration, 2018] The IceCube Collaboration (2018). Neutrino emission from the direction of the blazar txs 0506+056 prior to the icecube-170922a alert. *Science*, 361(6398):147–151. [Cited on pages 41, 65, 66, and 67.]

[The IceCube Collaboration et al., 2018] The IceCube Collaboration, Fermi-LAT, MAGIC, AGILE, ASAS-SN, HAWC, H.E.S.S., INTEGRAL, Kanata, Kiso, Kapteyn, Liverpool Telescope, Subaru, Swift/NuSTAR, VERITAS, and VLA/17B-403 (2018). Multimessenger observations of a flaring blazar coincident with high-energy neutrino icecube-170922a. *Science*, 361(6398). [Cited on pages 19, 20, 21, 22, 23, 24, and 25.]

[Urry and Padovani, 1995] Urry, C. M. and Padovani, P. (1995). Unified schemes for radio-loud active galactic nuclei. *Publ. Astron. Soc. Pac.*, 107:803. [Cited on pages 2, 4, and 76.]

[Waxman and Bahcall, 1997] Waxman, E. and Bahcall, J. (1997). High energy neutrinos from cosmological gamma-ray burst fireballs. *Phys. Rev. Lett.*, 78:2292–2295. [Cited on pages 4 and 15.]

[Zatsepin and Kuz'min, 1966] Zatsepin, G. T. and Kuz'min, V. A. (1966). Upper Limit of the Spectrum of Cosmic Rays. *Soviet Journal of Experimental and Theoretical Physics Letters*, 4:78. [Cited on pages 18 and 92.]

Appendix B

Abbreviations

Table B.1: *Table of Abbreviations.*

GFU	gamma-ray follow-up	stream of muon tracks for IC realtime alerts
HESE	high energy starting events	highest purity IC neutrino sample
EHE	extremely high energy [events]	IC alert sample of tracks above a certain energy threshold
SMBH	supermassive black hole	
GRB	Gamma-Ray Burst	
ν peak	synchrotron peak	first-hump peak in a blazar SED
EBL	Extragalactic Background Light	non-CMB non-alactic diffuse photon bg
EGB	extragalactic gamma-ray background	gamma-rays from resolved and unresolved sources and true diffuse processes as measured at high gal. latitudes
FSRQ	flat-spectrum radio quasar	
SED	Spectral energy distribution	
LBL/IBL/HBL		low/intermediate/high synchrotron peaked BL Lac objects
UHECR	Ultra-high energy cosmic rays	
SPE	Single photo electron [fit]	IceCube reconstruction fit [E. Andres, 2000]
MPE	Multi-photo electron [fit]	IceCube reconstruction fit [E. Andres, 2000]
SMT8	single-multiplicity 8	IceCube trigger filter on 8 events [E. Andres, 2000]
pdf	probability density function	
CMB	Cosmic Microwave Background	
GZK	Greisen-Zatsepin-Kuzmin	[Greisen, 1966] [Zatsepin and Kuz'min, 1966]
ICXX	IceCube Season XX	Detector Season (one year) with XX strings
ICXX_YY	IceCube Season XX in year YY	Detector Season (one year) with XX strings in the year 20YY
DOM	Digital Optical Module	spherical photodetector + electronics unit in IceCube
ICL	IceCube Counting Lab	IceCube surface countinghouse
GCN	Gamma-ray coordinates network	https://gcn.gsfc.nasa.gov/
AMON	Astrophysical Multimessenger Online Network	[Smith et al., 2013] [Smith et al., 2013]
FAVA	Fermi All-sky Variability Analysis	[Fermi, 1949]
VHE	Very High Energy Observatory Network	Gamma-rays in the detection band of IACTs
BDT	Boosted Decision Tree	Multivariate selection
MC	Monte Carlo	Randomized Simulation Technique, here: Simulation data(set)
TS	Test Statistics	Likelihood ratio proxy
LLH	Likelihood	
livetime	read: 'exposure'	integrated runtime of the detector

List of Figures

List of Tables